MULTISCALE CONSTITUTIVE MODELING OF GRAPHENE-BASED AND MULTIFERROIC COMPOSITES

by

ROOHOLLAH HASHEMI

A dissertation submitted to the

Graduate School-New Brunswick

Rutgers, The State University of New Jersey

In partial fulfillment of the requirements

For the degree of

Doctor of Philosophy

Graduate Program in Mechanical and Aerospace Engineering

Written under the direction of

Dr. George J. Weng

And approved by

_____

_____

_____

_____

New Brunswick, New Jersey

JANUARY, 2017

ABSTRACT OF THE DISSERTATION

Multiscale constitutive modeling of graphene-based and multiferroic composites

by ROOHOLLAH HASHEMI

Dissertation Director:

Dr. George J. Weng

The main focus of this thesis is on the constitutive modeling of two important classes of advanced functional materials, that is graphene-based nanocomposites and piezoelectric-piezomagnetic multiferroic composites. Along the way, several related issues with complex physical nature are essentially examined from a continuum-based viewpoint. Our study begins with the development of a homogenization scheme with several desirable features for determination of overall magneto-electro-elastic response of multiferroic composites containing periodic distribution of multi-inhomogeneities. The accuracy and applicability of proposed theory is verified through consideration of several examples of three-phase multiferroic composites with complex microstructures. Besides, the strong dependence of overall behavior of composites on the microstructure parameters, such as the interface condition, thickness, eccentricity and material properties of core inhomogeneities and their coating layers is well demonstrated. Through the second part of this investigation, we offer a robust analytical methodology to determine the magneto-electro-elastic scattered fields of a shear wave induced by a two-phase multiferroic inhomogeneity within a transversely isotropic piezoelectric or piezomagnetic medium. To put its wide range of applicability in perspective, the developed theory is applied to several descriptive examples with various

degrees of complexities. The numerical results thoroughly illustrate the influence of material properties of constituent phases, the thickness and eccentricity of coating layer, and the frequency of propagating SH-wave on the scattered fields induced by the multiferroic fiber. In the third part of this thesis, we aim to uncover how the imperfect load transfer at the graphene–matrix interface can affect the time-dependent viscoelastic response of graphene/polymer nanocomposites. To this end, different interface models are formulated within the framework of Mori-Tanaka homogenization theory. Through consideration of different sets of experimental data we demonstrate that, by adopting the weakened interface models in our homogenization theory, the quantitative behavior of creep response of graphene/polymer nanocomposites can be well captured. In addition, both stress relaxation and stress–strain relations are also found to greatly depend on the interface condition. In the closing part of this investigation, the effective electrical conductivity and permittivity constants of graphene/polymer nanocomposites are examined via the effective-medium theory. To do so, the microcapacitor and electron tunneling activities are taken as two interfacial processes that depend on the volume concentration of graphene fillers, and can be well modeled in a phenomenological way. The proposed model is shown to be able to successfully recover the experimental data of nanocomposite samples in AC electrical settings.

Acknowledgment

First, I would like to offer my gratitude and appreciation to my PhD advisor, Dr. George J. Weng, for his valuable support throughout my PhD study. I also would like to express my sincere thanks to Dr. Mitsunori Denda, Dr. Jerry Shan and Dr. Jackie Li for being my dissertation committee members.

Dedication

To my beautiful wife, Dr. Zahra Erami. Honored to be your husband.

Table of contents

List of tables

List of figures

Chapter 1.

Introduction

1.1. Multiferroic composites

The first focus of this thesis is on the study of multiferroic composites. These advanced functional materials usually consist of a piezoelectric phase (i.e. $BaTiO_3$, PZT, etc) combined with a piezomagnetic material (i.e. $CoFe_2O_4$, Terfenol-D, etc). In the recent years, multiferroic composites have attracted tremendous attention from academic and industrial point of views due to the coupling effect among their elastic, electric and magnetic fields. As the most fascinating feature of these functional materials, they exhibit the magneto-electric coupling even though this effect is absent in their individual piezomagnetic and piezoelectric constituent phases. As schematically shown in Fig. 1.1, this magneto-electric coupling phenomenon results from the "product properties" of multiferroic composites (Van Suchtelen, 1972; Nan et al., 2008): an applied electric field generates a deformation in the piezoelectric phase, which in turn generates a deformation in the piezomagnetic phase, giving rise to the magnetization. Noteworthy to mention that the magneto-electric coupling effect of a multiferroic composite can be achieved even at room temperature, whereas similar coupling phenomena in single-phase magneto-electric materials is often observed only at very low temperature. Such a strong magneto-electric coupling behavior of multiferroic composites is a key factor for their broad potential applications in new multifunctional materials and devices, such as four-state memories, low-power systems, magnetically controlled opto-

electric devices, and smart sensors. Inspired by these applications, numerous studies in the literature are concerned with the determination of overall properties of multiferroic composites, in particular, their magneto-electric coupling moduli. It is further notable that, as a well-established phenomenon, the bond quality between inhomogeneities and surrounding matrix plays a significant role in microscopic fields and overall macroscopic response of multiferroic composites. In addition, thanks to recent advances in coating technology, a single or multiple active coating layers can be applied to inhomogeneites in order to achieve a better design flexibility and tailor the effective magneto-electro-elastic properties of these materials. In view of the physical contributions that can be made by the coating layers, the development of theoretical models with interphase effects then seems to be inevitable for the appropriate treatment of a real multiferroic composite. This is the first concern of this thesis.

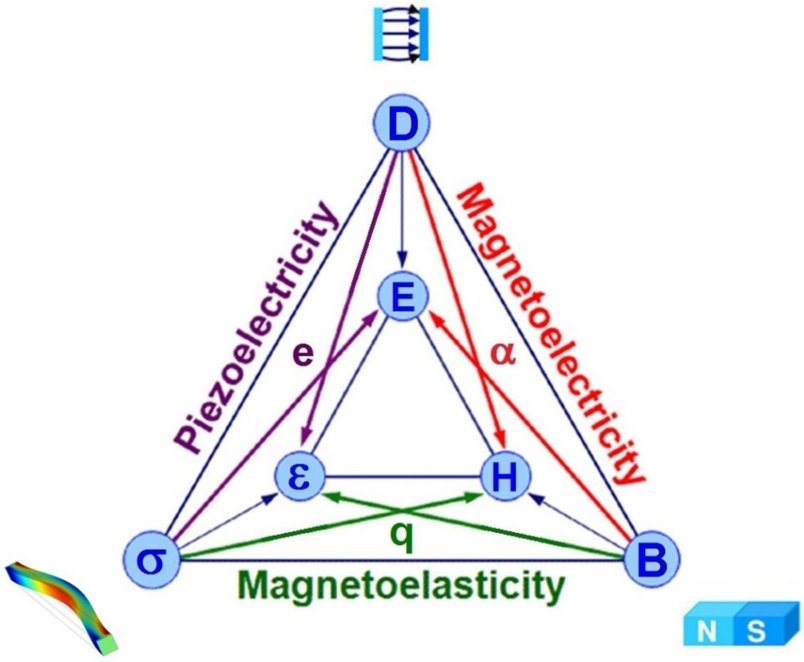

Fig. 1.1. Schematic illustration of magneto-electro-elastic coupling in multiferroic composites.

1.2. Graphene nanocomposites

Discovery of graphene and the subsequent development of graphene nanocomposite have led to a significant impact on the material science and technology (Novoselov et al. 2004; Stankovich et al., 2006). Graphene, a two-dimensional monolayer of sp^2-bonded carbon atoms, exhibits a range of remarkable properties, including: exceptional Young's modulus (~ 1 TPa), high tensile strength (~ 130 GPa), excellent thermal conductivity (~ 5000 w/mK), superb electrical conductivity (~ 10^4-10^5 S/m), and high surface area (~ 2600 m^2/g). These outstanding properties of graphene make it the basic building unit for an important family of nano-sized fillers, including: graphene nanosheet (GNS) which is a single or few-layered graphene sheet, and graphene nanoplatelet (GNP) which is a stack of multiple graphene layers. In fact, graphene can be considered as the most fascinating choice to enhance the thermal, electrical and mechanical properties of a broad range of materials, such as polymers, metals, and cement (see Fig. 1.2 for the morphology of a graphene-based material). In the context of electrical properties, the addition of highly conductive graphene fillers into polymer matrix has stimulated a surge of scientific interests from the research communities. It is noteworthy that there is a great demand in the electrical industry for flexible polymeric composites with excellent electrical performance and proper mechanical strength. The polymeric materials are insulator which can be made conductive by adding a large volume fraction of conventional conducting fillers in micrometer size, such as metal and graphite particles. However, the high loading of these fillers results in low mechanical strength, heavy weight and poor processability. In view of these shortcomings, highly conductive graphene fillers can be incorporated as alternative reinforcements to form the flexible functional

materials with desirable electro-mechanical properties. In this novel class of lightweight materials, the graphene fillers begin to contact to each other at a very low volume concentration, known as percolation threshold, owing to their extreme geometries. This process leads to the formation of percolating networks and micro-capacitor structures throughout the entire material, which eventually results in several orders of magnitude increase in the effective electrical properties of graphene nanocomposites. In the light of this unique characteristic, the graphene-based reinforcement of polymer materials has found a great potential application in sensors and stretchable electronics, electromagnetic shielding, super-capacitors, etc. As a result, a large number of conductive nanocomposites have been fabricated and characterized by incorporating graphene fillers in different polymeric matrixes, such as epoxy, polypropylene, poly(vinylidene fluoride), polystyrene, etc.

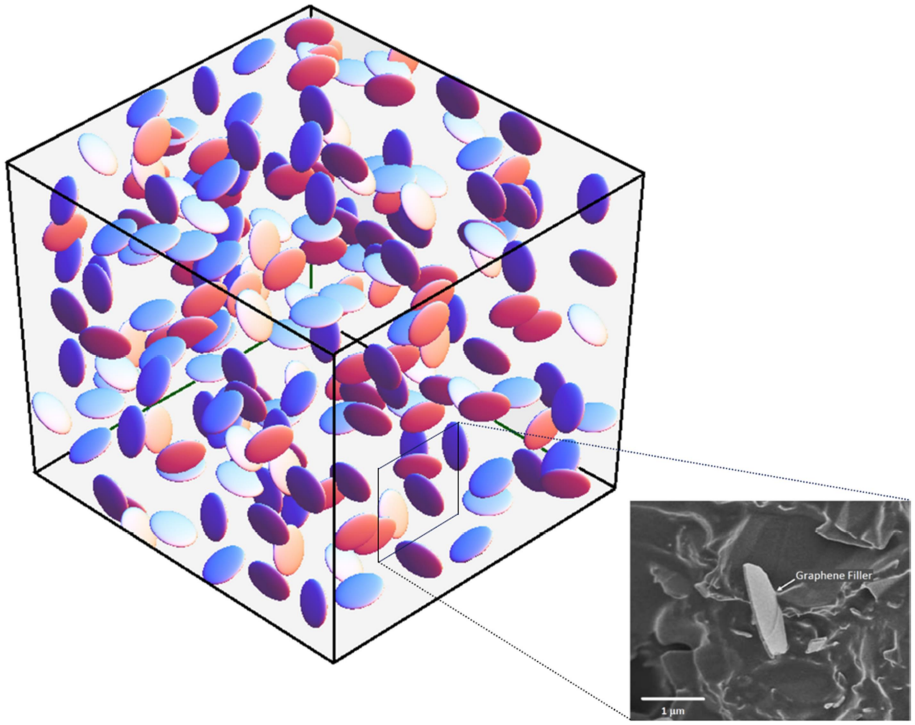

Fig. 1.2. Schematic illustration of a graphene-based nanocomposite, showing graphene fillers with idealized disk-like microgeometries (FESEM image of GNP is from King et al., 2015).

Inspired by the unique properties mentioned above, a quantitative prediction on the overall mechanical and electrical behavior of graphene nanocomposites is essential. However, an accurate modeling of these materials is challenging due to the complex nature of existing physical processes. Because of the multi-scale nature of this problem, the other difficulty lies in relating the microscopic characteristics of their internal microstructures to the macroscopic properties of interest. For instance, the numerical contrast of graphene electrical conductivity compared with most polymers is in the order of 10^{12}-10^{21}. Moreover, the aspect ratio and surface area of graphene is very large in comparison with conventional fillers. Therefore, from the continuum prospective we are dealing with a high contrast and high aspect ratio problem which is dramatically different from the classical cases. A thorough investigation of literature reveals that although considerable experimental efforts have been made in exploring the properties of graphene composites, the theoretical and computational studies on these materials are rarely reported. As the most common computational treatment for this class of problems, Monte Carlo (MC) and Molecular Dynamics (MD) methods have been employed to study nanocomposites. These methods can provide a valuable insight into the microscopic processes; however, the high computational expense undermines their capability for the simulation of systems where fillers have extreme range of geometry and material properties. Recognizing the potential gain that theoretical models can deliver, it will be greatly beneficial to adopt them for studying the physical characteristics of graphene-based nanocomposites. This is the second focus of this thesis. We then aim to utilize some continuum-based theories for examining the effective viscoelastic and electrical properties of graphene/polymer nanocomposites.

1.3. Thesis outline

This is the outline of succeeding chapters. Through Chapter 2, we first develop a robust homogenization scheme with several desirable features to determine the effective magneto-electro-elastic properties of periodic multiferroic composites with multi-phase inhomogeneities. The theory is then applied to a wide range of problems to examine the influence of a variety of microstructural parameters on the overall behavior of multiferroic composites. Chapter 3 is devoted to a study on the scattered fields of a time-harmonic shear wave by an eccentric two-phase multiferroic fiber embedded in a third phase piezoelectric or piezomagnetic medium. For the theoretical treatment of such a complex dynamics problem, we then offer a new micromechanics-based approach formulated within a rigorous mathematical framework. Chapter 4 is concerned with the influence of imperfect interface condition on the overall viscoelastic response of graphene/polymer nanocomposites. To this end, we develop a novel theory that embody the most essential features of nanocomposites, i.e. the time-dependent viscoelastic behavior of polymeric matrix, the anisotropy of elastic graphene fillers, and the imperfect load transfer at the filler-polymer interface. In Chapter 5, a continuum-based theory for determination of the effective electrical conductivity and permittivity constants of graphene-based nanocomposites is developed. Along the way, upon statistical modification of interfacial properties of graphene fillers, we plan to model the microcapacitor and electron tunneling activities in a phenomenological way. At the end, Chapter 6 gives a brief overview of the future research possibilities in the field of graphene-based and multiferroic composites.

Chapter 2.

Multiferroic composites with periodic multi-phase inhomogeneities

2.1. Overview

As mentioned earlier, one of the most intriguing features of multiferroic composite is the presence of magneto-electric coupling coefficient, even though none of constituent phases possesses such a property. The magnitude of this coupling constant depends on many microstructural parameters, such as material property, volume concentration and configuration of fibers/particles, and the bound quality at inhomogeneity-matrix interface. Inspired by the potential applications of multiferroic composites, numerous studies in the literature are concerned with the determination of overall properties of these functional materials, in particular, their magneto-electric coupling moduli. For instance, the mean field models have been employed by Li & Dunn (1998), Huang (1998), Li (2000) and Srinivas et al. (2006) to estimate the effective properties of multiferroic composites. Benveniste (1995) employed a formalism approach discovered by Milgrom & Shtrikman (1989) to obtain the exact relations for the effective moduli of a multiferroic with cylindrical fibers. Nan (1994) and Huang & Kuo (1997) adopted the Green's function approach to study the overall behavior of a fibrous multiferroic composite. In addition, a two-scale homogenization theory was employed by Aboudi (2001) to study the magneto-electro-elastic coupling and cross-property connections in a two-phase composite. Liu and Kuo (2012) developed the

micromechanical approach of E-inclusions to determine the effective properties of fibrous multiferroics. Moreover, the finite element method (FEM) was developed by Liu et al. (2004) and Lee et al. (2005) to address the periodic multiferroic composites with general microstructures.

All foregoing investigations are based on the simplifying assumption of the two-phase models with an abrupt inhomogeneity-matrix interface. However, it is greatly known that the bond quality between inhomogeneities and surrounding matrix plays a significant role in overall response of composite materials. The consideration of three-phase models with interphase effect then seems to be inevitable for the appropriate treatment of a real multiferroic composite. It is notable that, often, a transition zone with weakened material properties undesirably forms between reinforcements and the host matrix, as a result of the chemical interactions during the manufacture process of composite material. In other situations, the reinforcing fillers can be intentionally coated by interphase layers to improve the bonding strength. The interphase layers may have constant properties or spatially varying properties (Kuo, 2011; Hashemi et al., 2010 & 2015). Thanks to recent advances in coating technology, a single or multiple active coating layers also can be applied to inhomogeneites in order to achieve a better design flexibility and tailor the effective magneto-electro-elastic properties. In view of the physical contributions that can be made by the interphase layer, a number of theoretical investigations have paid special attention to this topic. For instance, Tong et al. (2008) adopted the generalized self-consistent method, while Camacho-Montes et al. (2009), Espinosa-Almeyda et al. (2011, 2014) and Guinovart-Díaz (2013) employed the asymptotic homogenization method to calculate the effective magneto-electro-elastic

properties of composites containing coated fibers. The classic Rayleigh's formulism was generalized by Kuo (2011) and Kuo and Pan (2011) to determine the overall behavior of composites with multicoated fibers under anti-plane shearing and in-plane electro-magnetic fields. Wang & Pan (2007) and Dinzart & Sabar (2011) applied the Mori-Tanaka model in conjunction with two different approaches, i.e. complex variable method and Green's function technique with interfacial operators, to determine the overall behavior of multiferroic composites with thinly coated inhomogeneities under anti-plane mechanical and in-plane electro-magnetic loadings. Yan et al. (2013) developed the eigenfunction expansion-variational method (originally formulated by Yan et al., 2011) to address the anti-plane coupling problem of a three-phase multiferroic composite containing coated circular fibers with periodic distributions. In addition, Kuo & Peng (2013) and Wang et al. (2015*c*) adopted a two-level recursive Mori-Tanaka model to assess the interphase effect on the magneto-electric coupling coefficients of multiferroic composites with random microstructures. All of these studies have demonstrated the significant impact of imperfect interface condition and/or the influence of active coating layer on the overall response of fibrous multiferroics.

This chapter intends to develop a homogenization scheme for determination of the effective magneto-electro-elastic properties of a periodic multiferroic composite with general multi-inhomogeneites. The proposed methodology is quite robust, so that it can be applied to a wide range of complex systems where the coating layers do not have to be thin, the shape and orientation of the core particle and coatings do not have to be identical, their centers do not have to coincide, their magneto-electro-elastic properties do not have to remain uniform, and the microstructure can be with the 2D elliptic or the 3D ellipsoidal inhomogeneity. Present

theory with such a desirable features is achieved based on the theoretical framework of Shodja & Roumi (2005) in conjunction with the superposition procedure of Kargarnovin et al. (2011) extended here for the treatment of magneto-electro-elastic multi-coated inhomogeneities. The development starts from the local equivalent inclusion principle through the introduction of the position-dependent equivalent eigenstrain-electric-magnetic fields. Then with a Fourier series expansion and a superposition procedure, the volume-averaged equivalent eigenfields for each domain of multi-inclusion systems are obtained. This approach is very efficient regardless of the number of phases of the reinforcing particles, and yields accurate values of the eigenfields at any desired domain. The results for local fields over the constituent phases in turn are used in the energy equivalency criterion to determine the effective magneto-electro-elastic properties of composite material. To demonstrate wide range of applicability of this scheme, it will be applied to examine the properties of several multiferroic composites with different microstructures. The calculated results reflect the complex nature of interplay between the properties of core, matrix, and coating, as well as whether the coating is uniform, functionally graded, or eccentric.

In what follows, an inhomogeneity is a subdomain of a medium whose magneto-electro-elastic properties differ from its surrounding matrix; in contrast, an inclusion is a subdomain having the same material properties of as those of matrix, but possessing the eigenstrain-electric-magnetic fields.

2.2. The theory

Consider a multiferroic composite material which contains periodically distributed piezoelectric (or piezomagnetic) multi-inhomogeneitis of common geometry and dimensions within a piezomagnetic (or piezoelectric) matrix. The possible microstructure of inner particle (denoted by $\psi_1 \equiv \Gamma_1$), and its surrounding coating layers (denoted by $\Gamma_\alpha, \alpha = 2,3,...,N$) are depicted in Fig. 2.1(a). In view of such a multi-layer morphology for the inhomogeneity system, the sequence $\psi_1, \psi_2, \ldots, \psi_N = \bigcup_{\alpha=1}^{N} \Gamma_\alpha$ forms a set of nested ellipsoidal domains. The core and its coating have arbitrary material properties, positions and aspect ratios. It is notable that the individual piezoelectric and piezomagnetic phases of composite material has the usual electro-elastic and magneto-elastic coupling, respectively, but neither has the magneto-electric coupling. The multiferroic composite, however, has it. As a result, it is more convenient to write the set of constitutive equations for the constituent phases in its general form that also include this magneto-electric coupling term. In this light, we adopt the following coupled relations

$$\begin{aligned} \sigma_{ij} &= C_{ijkl}\,\varepsilon_{kl} - e_{kij} E_k - q_{kij} H_k, \\ D_i &= e_{ikl}\,\varepsilon_{kl} + \kappa_{ik}\, E_k + \alpha_{ik}\, H_k, \\ B_i &= q_{ikl}\,\varepsilon_{kl} + \alpha_{ik}\, E_k + \mu_{ik}\, H_k, \end{aligned} \tag{2.1}$$

for the piezoelectric, piezomagnetic, and multiferroic responses. The constitutive equations involve 6 physical field quantities, i.e., mechanical strain ε_{ij} and stress σ_{ij}, electric field E_i and displacement field D_i, and magnetic field H_i and flux density B_i. The moduli C_{ijkl}, κ_{ij} and μ_{ij} are, respectively, the elastic stiffness tensor, electric permittivity and magnetic permeability tensors. α_{ij} is the magneto-electric coefficient tensor, and e_{ijk} and q_{ijk} are

piezoelectric and piezomagnetic constant tensors, respectively. In the following analysis, it is convenient to write all magneto-electro-elastic moduli in a unified fashion. To this end, we call upon the notations introduced initially by Barnett and Lothe (1975) for the treatment of piezoelectric materials, and generalized later by Alshits et al. (1992) to involve the magneto-electric coupling. This notation is identical to the conventional notation with the exception that lowercase subscripts take the range from 1 to 3, while the uppercase subscripts range from 1 to 5, with the subscripts 4 and 5 referring to the electric and magnetic quantities, respectively. The repeated upper case subscripts then are summed over 1 to 5. According to this notation, the field variables of material take the following shorthand from:

$$\Sigma_{iJ}=\begin{cases}\sigma_{ij}, & J=1,2,3,\\ D_i, & J=4,\\ B_i, & J=5,\end{cases}\qquad U_J=\begin{cases}u_J, & J=1,2,3,\\ \phi, & J=4,\\ \varphi, & J=5,\end{cases}\qquad Z_{Mn}=\begin{cases}\varepsilon_{Mn}, & M=1,2,3,\\ -E_n, & M=4,\\ -H_n, & M=5,\end{cases} \tag{2.2}$$

As a result, the general form of the linear constitutive relations can be written as:

$$\Sigma_{iJ}=L_{iJMn}Z_{Mn}, \tag{2.3}$$

in which

$$L_{iJMn}=\begin{cases}C_{ijmn}, & J,M=1,2,3,\\ e_{nij}, & J=1,2,3,M=4,\\ q_{nij}, & J=1,2,3,M=5,\\ e_{imn}, & J=4,M=1,2,3,\\ q_{imn}, & J=5,M=1,2,3,\\ -\alpha_{in}, & J=4,M=5,\\ -\alpha_{in}, & J=5,M=4,\\ -K_{in}, & J=4,M=4,\\ -\mu_{in}, & J=5,M=5.\end{cases} \tag{2.4}$$

stands for the generalized moduli tensor of corresponding phase. In the light of this contracted notation, the magneto-electro-elastic moduli tensor of matrix is denoted by L^m_{iJMn},

and the properties of the αth phase of multi-coated inhomogeneity is differentiated with the corresponding superscript, as $L_{iJMn}^{\Gamma_\alpha}$ stands for the moduli tensor of Γ_α, $\alpha = 1,2,\ldots,N$.

The far-field mechanical displacement, electric and magnetic potentials prescribed on the boundary of multiferroic composite are given by $u_i^o = \varepsilon_{ij}^o x_j$, $\phi^o = -E_i^o x_i$ and $\varphi^o = -H_i^o x_i$, respectively, which give rise to an overall strain-electric-magnetic field, denoted by Z_{Mn}^o, over entire composite material. This far-field loading will be disturbed due the presence of multi-coated inhomogeneity in the matrix. We now adopt the Eshelby's equivalent inclusion principle (Eshelby, 1957), but written for a heterogeneous medium with the coupled magneto-electro-elastic behavior, in order to determine the disturbed fields over each phase of multi-inhomogeneity system.

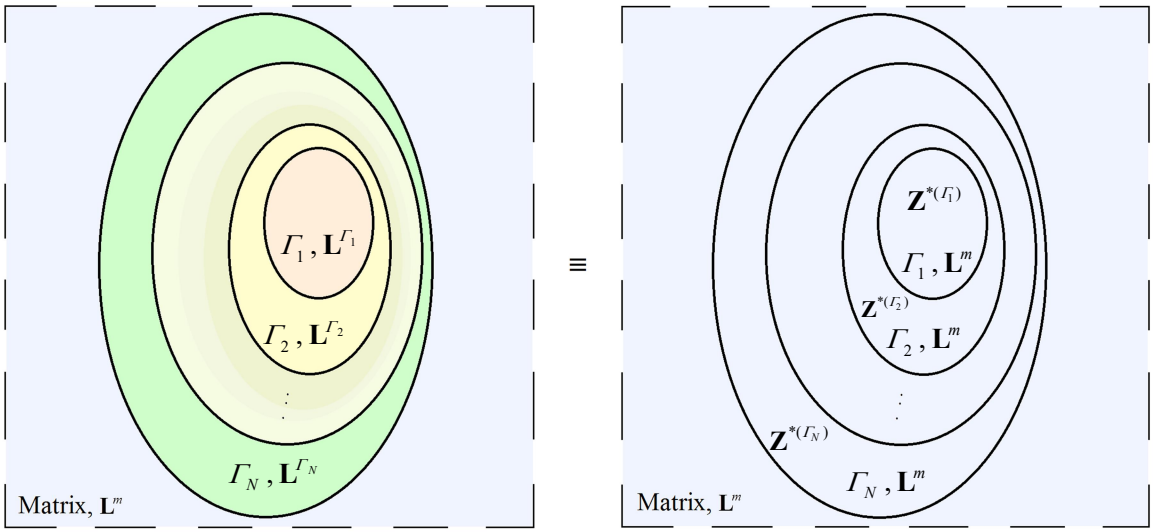

(a) (b)

Fig. 2.1. Schematic diagram of (a) an ellipsoidal multiphase inhomogeneity replaced by (b) an equivalent multi-inclusion system with proper eigenfields $\mathbf{Z}^{*(\Gamma_\alpha)}$ over regions $\Gamma_\alpha, \alpha = 1,2,...,N.$

According to this methodology, we replace the multi-inhomogeneity that carry different moduli with the equivalent multi-inclusions with the properties of the matrix but carrying certain equivalent eigenstrain-electric-magnetic field, denoted by stared the quantities,

$Z_{Mn}^{*(\Gamma_\alpha)}(\boldsymbol{x})$. The configuration of such a multi-inclusion is schematically shown in Fig. 2.1(b). It is evident that, due to inter-particle interactions and the complex nature of the microgeometry, the eigenfield is position-dependent. The magnitude of this quantity can be determined on the basis that the fields in the original heterogeneous system and in the equivalent homogeneous system, but carrying this specified eigenfield, would be identical. This equivalency then holds for a proper choice of $Z_{Mn}^{*(\Gamma_\alpha)}(\boldsymbol{x})$ defined over region $\Gamma_\alpha, \alpha = 1,2,...,N.$ Since the multi-inhomogeneities have a periodic distribution, the associated equivalent eigenstrain-electric-magnetic fields can be expressed in terms of the Fourier series expansion, as

$$Z_{Mn}^{*(\Gamma_\alpha)}(\boldsymbol{x}) = \sum_{\boldsymbol{\xi}} \tilde{Z}_{Mn}^{*(\Gamma_\alpha)}(\boldsymbol{\xi}).\, e^{\mathrm{i}\boldsymbol{\xi}.\boldsymbol{x}}, \tag{2.5}$$

where

$$\tilde{Z}_{Mn}^{*(\Gamma_\alpha)}(\boldsymbol{\xi}) = \frac{1}{V} \int_{RVE} Z_{Mn}^{*(\Gamma_\alpha)}(\boldsymbol{x})\; e^{-\mathrm{i}\boldsymbol{\xi}.\boldsymbol{x}} d\boldsymbol{x}, \tag{2.6}$$

and $\mathrm{i} = \sqrt{-1}$ and $\sum_{\boldsymbol{\xi}}$ is, in general, a triple summation corresponding to ξ_i $(i = 1,2,3)$ which are in turn associated with the periodicity of the eigenstrain-electric-magnetic field in the directions x_i. Moreover, *RVE* stands for the representative volume element of composite material distributed periodically throughout the entire domain. The volume of this fundamental element is denoted by $V = \Lambda_1\Lambda_2\Lambda_3$, in which Λ_i is the dimension of the parallelepiped unit cell along the respective x_i-coordinate $(i = 1,2,3).$ We now decompose the multi-inclusion into a series of single inclusion problems by means of a superposition scheme in which the eigenstrain-electric-magnetic of each phase is first introduced into itself, and

then that of the *k*th phase is introduced into the (*k*-1)th region for subtraction (Shodja & Roumi, 2005; Kargarnovin et al., 2011). As we count the phase outward so that the inner inclusion is phase 1, this introduction of the eigenfield actually starts from the outermost phase. The schematic representation of such a decomposition of multi-inclusion system is illustrated in Fig. 2.2, where the top figures indicate the introduction of their own eigenfield and the bottom ones with a minus sign reflect the subtraction of eigenfield from its immediate outer layer.

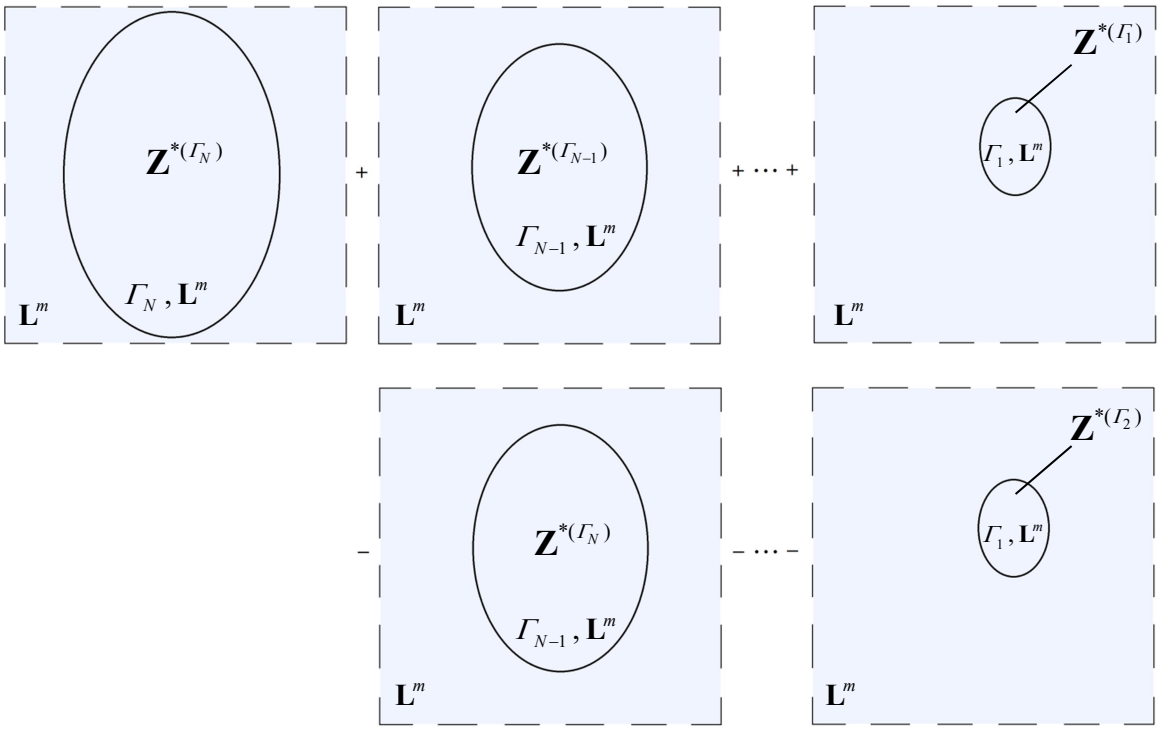

Fig. 2.2. Superposition scheme for the determination of disturbed strain-electric-magnetic field. The multi-inclusion system has been decomposed to single-inclusions with proper eigenfields.

In view of an individual single-inclusion problem shown in subfigures of Fig. 2.2, the eigenfield $Z_{Mn}^{*(\gamma)}$, $\gamma \equiv \Gamma_i$ $(i = 1,2,\ldots,N)$ distributed over the ellipsoidal region $\beta \equiv \psi_j$ $(j = 1,2,\ldots,N)$ in turn produces a disturbed magneto-electro-elastic field, to be denoted by

$Z^{d}_{Mn}(\boldsymbol{x};\boldsymbol{Z}^{*(\gamma,\beta)})$, in the entire body which carries the properties of the matrix, L^{m}_{iJMn}. In this light, the magneto-electro-elastic field for such a single-inclusion system can be written as

$$\Sigma_{iJ}(\boldsymbol{x}) = L^{m}_{iJMn}[Z^{o}_{Mn} + Z^{d}_{Mn}(\boldsymbol{x};\boldsymbol{Z}^{*(\gamma,\beta)}) - Z^{*(\gamma)}_{Mn}(\boldsymbol{x})], \quad \boldsymbol{x} \in \beta. \tag{2.7}$$

which must satisfy the equilibrium equation,

$$\Sigma_{iJ,i} = 0. \tag{2.8}$$

Upon substitution of expression of eigenfield from Eqs. (2.6) and (2.7) into the equilibrium equation, and by invoking the definition of strain, electric and magnetic fields through the relevant calculation process, one can arrive at the following unified expression for the disturbed field induced by a the corresponding single-inclusion system with periodic distribution,

$$Z^{d}_{Mn}(\boldsymbol{x};\boldsymbol{Z}^{*(\gamma,\beta)}) = \frac{1}{V}\sum_{\boldsymbol{\xi}^{\beta}} Q_{MnKl}(\boldsymbol{\xi}^{\beta}) \int_{\beta} Z^{*(\gamma)}_{Kl}(\boldsymbol{x}') e^{i\boldsymbol{\xi}^{\beta}.(\boldsymbol{x}-\boldsymbol{x}')} d\boldsymbol{x}' \,, \tag{2.9}$$

where

$$Q_{MnKl}(\boldsymbol{\xi}) = \begin{cases} L^{m}_{iJMn}\, D^{-1} \xi_i \, (\xi_n N_{MJ} + \xi_M N_{nJ})/2, & M = 1,2,3, \\ L^{m}_{iJMn}\, D^{-1} \xi_i \, \xi_n N_{MJ}, & M = 4,5. \end{cases} \tag{2.10}$$

In this formula, $D(\boldsymbol{\xi})$ and $N_{MJ}(\boldsymbol{\xi})$ are the determinant and cofactor of $K_{MJ} = L^{m}_{iJMn}\xi_n\xi_i$, respectively. Now, using Eq. (2.9) and with the aid of the superposition scheme shown in Fig. 2.2, the overall disturbed strain-electric-magnetic field at every point in the matrix and the equivalent multi-inclusion can be written as

$$
\begin{aligned}
Z^d_{Mn}(\boldsymbol{x}) &= \sum_{\alpha=1}^{N} Z^d_{Mn}(\boldsymbol{x};\boldsymbol{Z}^{*(\Gamma_\alpha,\psi_\alpha)}) - \sum_{\alpha=1}^{N-1} Z^d_{Mn}(\boldsymbol{x};\boldsymbol{Z}^{*(\Gamma_{\alpha+1},\psi_\alpha)}) \\
&= \sum_{\alpha=1}^{N-1}\Big[Z^d_{Mn}(\boldsymbol{x};\boldsymbol{Z}^{*(\Gamma_\alpha,\psi_\alpha)}) - Z^d_{Mn}(\boldsymbol{x};\boldsymbol{Z}^{*(\Gamma_{\alpha+1},\psi_\alpha)})\Big] + Z^d_{Mn}(\boldsymbol{x};\boldsymbol{Z}^{*(\Gamma_N,\psi_N)}) \\
&= \frac{1}{V}\sum_{\alpha=1}^{N-1}\sum_{\boldsymbol{\xi}^{\psi_\alpha}} Q_{MnKl}(\boldsymbol{\xi}^{\psi_\alpha}) \int_{\psi_\alpha} [Z^{*(\Gamma_\alpha)}_{Kl}(\boldsymbol{x}') - Z^{*(\Gamma_{\alpha+1})}_{Kl}(\boldsymbol{x}')] e^{\mathrm{i}\boldsymbol{\xi}^{\psi_\alpha}\cdot(\boldsymbol{x}-\boldsymbol{x}')}\, d\boldsymbol{x}' \\
&\quad + \frac{1}{V}\sum_{\boldsymbol{\xi}^{\psi_N}} Q_{MnKl}(\boldsymbol{\xi}^{\psi_N}) \int_{\psi_N} Z^{*(\Gamma_N)}_{Kl}(\boldsymbol{x}') e^{\mathrm{i}\boldsymbol{\xi}^{\psi_N}\cdot(\boldsymbol{x}-\boldsymbol{x}')} d\boldsymbol{x}'.
\end{aligned}
\tag{2.11}
$$

To obtain the equivalent eigenstrain-electric-magnetic field pertinent to the αth phase, we now recall Eshelby's equivalent inclusion principle in the local form

$$
\begin{aligned}
\Sigma^o_{iJ} + \Sigma^d_{iJ}(\boldsymbol{x}) &= L^{\Gamma_\alpha}_{iJMn}\left(Z^o_{Mn} + Z^d_{Mn}(\boldsymbol{x})\right) \\
&= L^m_{iJMn}\left(Z^o_{Mn} + Z^d_{Mn}(\boldsymbol{x}) - Z^{*(\Gamma_\alpha)}_{Mn}(\boldsymbol{x})\right), \quad \boldsymbol{x}\in\Gamma_\alpha, \quad \alpha = 1,2,\ldots,N.
\end{aligned}
\tag{2.12}
$$

Since only the average field is needed for the calculation of effective moduli, this local form can be integrated over each subdomain to yield the averaged quantities

$$
\begin{aligned}
\left\langle \Sigma^o_{iJ}\right\rangle_{\Gamma_\alpha} + \left\langle \Sigma^d_{iJ}(\boldsymbol{x})\right\rangle_{\Gamma_\alpha} &= L^{\Gamma_\alpha}_{iJMn}\left(Z^o_{Mn} + \left\langle Z^d_{Mn}(\boldsymbol{x})\right\rangle_{\Gamma_\alpha}\right) \\
&= L^m_{iJMn}\left(Z^o_{Mn} + \left\langle Z^d_{Mn}(\boldsymbol{x})\right\rangle_{\Gamma_\alpha} - \left\langle Z^{*(\Gamma_\alpha)}_{Mn}(\boldsymbol{x})\right\rangle_{\Gamma_\alpha}\right), \quad \alpha = 1,2,\ldots,N.
\end{aligned}
\tag{2.13}
$$

where the bracket $\langle\bullet\rangle_{\Gamma_\alpha}$ denotes the volume average of the said quantity over region Γ_α, $\alpha = 1,2,\ldots,N.$ The volume average of $Z^d_{Mn}(\boldsymbol{x})$ over the αth phase in turn can be evaluated from Eq. (2.13), as

$$
\begin{aligned}
\left\langle Z^d_{Mn}(\boldsymbol{x})\right\rangle_{\Gamma_\alpha} &= \frac{1}{VV^{\Gamma_\alpha}}\sum_{\omega=1}^{N-1}\sum_{\boldsymbol{\xi}^{\psi_\omega}} Q_{MnKl}(\boldsymbol{\xi})\, G_{\Gamma_\alpha}(\boldsymbol{\xi}) \int_{\psi_\omega}\left[Z^{*(\Gamma_\omega)}_{Kl}(\boldsymbol{x}') - Z^{*(\Gamma_{\omega+1})}_{Kl}(\boldsymbol{x}')\right] e^{-\mathrm{i}\boldsymbol{\xi}^{\psi_\omega}\cdot\boldsymbol{x}'} d\boldsymbol{x}' \\
&\quad + \frac{1}{VV^{\Gamma_\alpha}}\sum_{\boldsymbol{\xi}^{\psi_N}} Q_{MnKl}(\boldsymbol{\xi})\, G_{\Gamma_\alpha}(\boldsymbol{\xi}) \int_{\psi_N} Z^{*(\Gamma_N)}_{Kl}(\boldsymbol{x}') e^{-\mathrm{i}\boldsymbol{\xi}^{\psi_N}\cdot\boldsymbol{x}'} d\boldsymbol{x}',
\end{aligned}
\tag{2.14}
$$

in which $G_{\Gamma_\alpha}(\boldsymbol{\xi}) = \int_{\Gamma_\alpha} e^{\mathrm{i}\boldsymbol{\xi}\cdot\boldsymbol{x}} d\boldsymbol{x}$ is readily available with the aid of

$$\int_{\psi_\alpha} e^{i\boldsymbol{\xi}.\boldsymbol{x}} d\boldsymbol{x} = \frac{3(\sin\eta - \eta\cos\eta)}{\eta^3} V^{\psi_\alpha}, \quad \eta = \sqrt{(a_1\xi_1)^2 + (a_2\xi_2)^2 + (a_3\xi_3)^2}, \tag{2.15}$$

where a_i (i=1,2,3) are the principle half-axes of the ellipsoidal domain. Finally, substituting Eq. (2.14) into the second equality of Eq. (2.13), and after some rearrangement, we obtain

$$\begin{aligned} Z^o_{Mn} = & \left[L^m_{iJMn} - L^{\Gamma_\alpha}_{iJMn} \right]^{-1} L^m_{iJKl} \left\langle Z^{*(\Gamma_\alpha)}_{Kl} \right\rangle_{\Gamma_\alpha} \\ & - \frac{1}{VV^{\Gamma_\alpha}} \sum_{\omega=1}^{N-1} \sum_{\boldsymbol{\xi}^{\psi_\omega}} Q_{MnKl}(\boldsymbol{\xi})\, G_{\Gamma_\alpha}(\boldsymbol{\xi}) \int_{\psi_\omega} \left[Z^{*(\Gamma_\omega)}_{Kl}(\boldsymbol{x}') - Z^{*(\Gamma_{\omega+1})}_{Kl}(\boldsymbol{x}') \right] e^{-i\boldsymbol{\xi}^{\psi_\omega}.\boldsymbol{x}'} d\boldsymbol{x}' \\ & - \frac{1}{VV^{\Gamma_\alpha}} \sum_{\boldsymbol{\xi}^{\psi_N}} Q_{MnKl}(\boldsymbol{\xi})\, G_{\Gamma_\alpha}(\boldsymbol{\xi}) \int_{\psi_N} Z^{*(\Gamma_N)}_{Kl}(\boldsymbol{x}') e^{-i\boldsymbol{\xi}^{\psi_N}.\boldsymbol{x}'} d\boldsymbol{x}', \quad \boldsymbol{x} \in \Gamma_\alpha \ (\alpha = 1,2,\ldots,N), \end{aligned} \tag{2.16}$$

when this relation is written for all N subdomains, it provides N simultaneous equations for $\left\langle Z^{*(\Gamma_\alpha)}_{Kl} \right\rangle_{\Gamma_\alpha}$, which then can be solved in terms of the averaged strain-electric-magnetic field in the matrix. The complex structure of Eq. (2.16) suggests a method for estimating $\left\langle Z^{*(\Gamma_\alpha)}_{Kl} \right\rangle_{\Gamma_\alpha}$ in terms of Z^m_{Mn}, in which the eigenfield in each phase will be replaced by its average value, leading to

$$\begin{aligned} Z^o_{Mn} = & \left[L^m_{iJMn} - L^{\Gamma_\alpha}_{iJMn} \right]^{-1} L^m_{iJKl} \left\langle Z^{*(\Gamma_\alpha)}_{Kl} \right\rangle_{\Gamma_\alpha} \\ & - \frac{1}{VV^{\Gamma_\alpha}} \sum_{\omega=1}^{N-1} \sum_{\boldsymbol{\xi}^{\psi_\omega}} Q_{MnKl}(\boldsymbol{\xi}) G_{\Gamma_\alpha}(\boldsymbol{\xi})\, G_{\psi_\omega}(-\boldsymbol{\xi}) \left[\left\langle Z^{*(\Gamma_\omega)}_{Kl} \right\rangle_{\Gamma_\omega} - \left\langle Z^{*(\Gamma_{\omega+1})}_{Kl} \right\rangle_{\Gamma_{\omega+1}} \right] \\ & - \frac{1}{VV^{\Gamma_\alpha}} \sum_{\boldsymbol{\xi}^{\psi_N}} Q_{MnKl}(\boldsymbol{\xi}) G_{\Gamma_\alpha}(\boldsymbol{\xi})\, G_{\psi_N}(-\boldsymbol{\xi}) \left\langle Z^{*(\Gamma_N)}_{Kl} \right\rangle_{\Gamma_N}, \quad \boldsymbol{x} \in \Gamma_\alpha \quad (\alpha = 1,2,\ldots,N), \end{aligned} \tag{2.17}$$

where $G_{\psi_\omega}(-\boldsymbol{\xi}) = \int_{\psi_\omega} e^{-i\boldsymbol{\xi}.\boldsymbol{x}'} d\boldsymbol{x}'$. We thus have N equations for the N unknowns eigenfields, $\left\langle Z^{*(\Gamma_\alpha)}_{Kl} \right\rangle_{\Gamma_\alpha}$. The result can be expressed in the general form of

$$\left\langle Z^{*(\Gamma_\alpha)}_{Mn} \right\rangle_{\Gamma_\alpha} = T^{\Gamma_\alpha}_{MnKl} Z^o_{Kl} \tag{2.18}$$

where $T_{MnKl}^{\Gamma_\alpha}$ is eigenfield concentration tensor of the said domain. Denoting the effective moduli tensor of composite system by $\bar{L}_{iJMn}$, the general form of constitutive relation between the macroscopic field quantities can be written as

$$\Sigma_{iJ}^{o} = \bar{L}_{iJMn} Z_{Mn}^{o}. \tag{2.19}$$

As well, under a uniform far-field loading, Z_{Mn}^{o} the total energy of the effective medium can be written as:

$$W = \frac{V}{2} \bar{L}_{iJMn} Z_{Ji}^{o} Z_{Mn}^{o}. \tag{2.20}$$

On the other hand, the total energy of a homogenous domain, *D* with distribution of multi-inclusions may be written as:

$$W = \frac{1}{2} \int_D L_{iJMn}^{m} \left(Z_{Mn}^{o} + Z_{Mn}^{d} - Z_{Mn}^{*} \right) \left(Z_{Mn}^{o} + Z_{Mn}^{d} \right) d\boldsymbol{x}, \tag{2.21}$$

Since applied strain-electric-magnetic fields, Z_{Mn}^{o} is uniform, Eq. (2.21) becomes:

$$W = \frac{V}{2} L_{iJMn}^{m} Z_{Ji}^{o} Z_{Mn}^{o} - \frac{V}{2} L_{iJMn}^{m} Z_{Ji}^{o} \int_D Z_{Mn}^{*} \, d\boldsymbol{x}, \tag{2.22}$$

In arriving at (2.22), it has been assumed that the average of disturbed fields over the entire domain is zero, $\left\langle Z_{Mn}^{d}(\boldsymbol{x}) \right\rangle_D = 0$. Upon consideration of the multi-inclusion systems with average equivalent eigen fields, Eq. (2.22) yields:

$$W = \frac{V}{2} L_{iJMn}^{m} Z_{Ji}^{o} Z_{Mn}^{o} - \frac{1}{2} L_{iJMn}^{m} Z_{Mn}^{o} \sum_{\alpha=1}^{N} V^{\Gamma_\alpha} \left\langle Z_{Ji}^{*(\Gamma_\alpha)}(\boldsymbol{x}) \right\rangle_{\Gamma_\alpha}, \tag{2.23}$$

where the volume of each constituent phase, V^{Γ_α}, provides the weighted mean for the corresponding average eigen field in the summation. Upon recalling Eq. (2.18), the equivalent energy criterion yields:

$$\bar{L}_{iJMn} Z^{o}_{Ji} Z^{o}_{Mn} = L^{m}_{iJMn} Z^{o}_{Ji} Z^{o}_{Mn} - L^{m}_{iJMn} Z^{o}_{Mn} \sum_{\alpha=1}^{N} f^{\Gamma_\alpha} \left\langle Z^{*(\Gamma_\alpha)}_{Ji}(\boldsymbol{x}) \right\rangle_{\Gamma_\alpha}, \tag{2.24}$$

where f^{Γ_α} stands for the volume fraction of matrix and the αth phase of particle ensemble. Having determined the average value of the eigen fields from Eq. (2.18), the effective magneto-electro-elastic properties of multiferroic composite with periodic microstructure can be obtained from Eq. (2.24).

Before we proceed to the numerical examples, some remarks on the applicability and robustness of the present methodology, which led to Eq. (2.24), can be highlighted in passing. In particular, several desirable features have been built into Eqs. (2.14) and (2.17) which enable us to determine the effective properties of multiferroic composites with the complex microstructures. For instance, the quantity $G(\boldsymbol{\xi})$ can reflect the ellipsoidal geometry of the particle core and its coatings, and the infinite series can account for the particle–particle interactions. Accordingly, in multiferroic composites with multiphase inhomogeneities, as long as the core particles and their surrounding interphase layers are ellipsoidal or possess geometries which are limiting case of an ellipsoid, the developed formulation would be applicable. Moreover, since the proposed theory is based on a multi-inhomogneneity system wherein the core and its coating layers can have distinct periodicity, the present theory is quite versatile, and it can be applied to a wide range of coating problems, i.e. thin or thick, single-layer or multi-layer, functionally graded (FG) and even eccentric coatings. In addition, we have observed that the summation over the infinite series in Eq. (2.17) always converge. This can be seen from the fact that function $Q_{MnKl}(\boldsymbol{\xi})$ remains finite as ξ_i $(i = 1,2,3)$ takes on large values, and that the integral terms $G_{\Gamma_\alpha}(\boldsymbol{\xi})$ and $G_{\psi_\omega}(-\boldsymbol{\xi})$

in the series go to zero like $1/\xi_i^2$ as ξ_i approaches to infinity. Accordingly, the infinite series in Eq. (2.17) are of order $1/\xi_i^4$ for large value of ξ_i, and this leads to a rapid convergence.

Table 2.1. Magneto-electro-elastic properties of $BaTiO_3$, $CoFe_2O_4$, Terfenol-D and Epoxy: C_{ijkl} (GPa), κ_{ij} (nC^2/Nm^2), μ_{ij} ($\mu N/s^2C^2$), e_{ijk} (C/m^2) and q_{ijk} (N/Am).

Properties	$BaTiO_3$ (BTO)	$CoFe_2O_4$ (CFO)	Terfenol-D (TD)	Epoxy
C_{1111}	150.37	286	8.54	8
C_{1122}	65.63	173	0.65	4.4
C_{1133}	65.94	170.3	3.91	4.4
C_{3333}	145.52	269.5	28.3	8
C_{1313}	43.86	45.3	5.55	1.8
κ_{11}	9.87	0.08	0.05	0.037
κ_{33}	11.08	0.093	0.05	0.037
μ_{11}	5	590	8.64	2.51
μ_{33}	10	157	2.26	2.51
e_{311}	-4.32	0	0	0
e_{333}	17.36	0	0	0
e_{113}	11.4	0	0	0
q_{311}	0	580.3	5.4	0
q_{333}	0	699.7	270.1	0
q_{113}	0	550	155.56	0

2.3. Numerical results and discussion

In this section, for a comprehensive demonstration on the generality and efficacy of present theory, we apply it to several problems of multiferroic composites with various complexities. In this process, the influence of microstructure parameters, such as the thickness, eccentricity, shape and magneto-electro-elastic properties of core inhomogeneities and their coatings on the overall response of composites also is illustrated. In what follows, all piezoelectric and piezomagnetic phases are transversely isotropic, with the respective poling and magnetization directions pointing along x_3-direction. The material properties used in the numerical calculations are listed in Table. 2.1.

2.3.1. Comparison with Kuo and Peng (2013) for BTO/CFO/TD composite

We first consider a multiferroic composite consisting of $BaTiO_3$ fibers coated by $CoFe_2O_4$ layers, embedded within a Terfenol-D matrix. For the sake of convenience, we denote the composite as BTO/CFO/TD. Kuo and Peng (2013) recently employed the finite element method (FEM) to obtain the effective properties of similar composite material. To make the necessary contact with their FEM results, three particular radius ratios, $R^{\text{fiber}}/R^{\text{coating}}$ =0.4, 0.6 and 0.8 have been considered for the BTO/CFO inhomogeneity system. Thus, this study will serve to make contact with the existing literature. We now adopt the present theory to determine the effective magneto-electric voltage coefficients of this BTO/CFO/TD composite, $\overline{\alpha}_{E11}$ and $\overline{\alpha}_{E33}$, for the specified radius ratios. $\overline{\alpha}_{Eij} = \overline{\alpha}_{ij} / \overline{\kappa}_{ij}$ (no summation) is an important set of parameters with practical importance for the measurement of magneto-

electric coupling in multiferroic materials. In comparison with the FEM results of Kuo and Peng (2013), our theoretical results for $\overline{\alpha}_{E11}$ and $\overline{\alpha}_{E33}$ are respectively illustrated in Fig. 2.3(a) and (b), as a function of the volume concentration of BTO/CFO inhomogeneity system, $f^{\text{fiber}} + f^{\text{coating}}$. It is evident from both figures that theoretical results reasonably match with the corresponding FEM results. The quantitative agreement between two sets of results can be observed over the entire range of volume concentrations of coated fibers.

2.3.2. Comparison with Kuo (2011) for BTO/TD/CFO composite

In present analysis, we consider a multiferroic composite consisting of BTO fibers with thick TD coatings, distributed periodically within a CFO matrix. Such a problem has been examined previously by Kuo (2011), who combined the methods of complex potentials with a re-expansion formulae and the generalized Rayleigh's formulation (1892) to obtain a complete solution of the multi-inclusion problem. We have employed the present theory to determine the overall behavior of composite material at three different volume concentrations of inhomogeneity system, $f^{\text{fiber}} + f^{\text{coating}} = 0.2$, 0.4 and 0.6. In present analysis, the radius ratio of BTO fiber to its TD coating is kept fixed at $R^{\text{fiber}}/R^{\text{coating}} = 0.8$. Table 2.2 displays our calculated results together with those of Kuo (2011) for the effective properties of BTO/TD/CFO composite, including $\overline{C}_{2323}$ (elastic modulus), $\overline{e}_{113}$ (piezoelectric constant), $\overline{\kappa}_{11}$ (dielectric permittivity), $\overline{\mu}_{11}$ (magnetic permeability), $\overline{q}_{113}$ (piezomagnetic constant) and $\overline{\alpha}_{11}$ (magneto-electric coefficient). It is readily observed that, for all specified volume fractions of BTO/TD inhomogeneity system, the results of proposed methodology is in a very

good agreement with those reported by Kuo (2011). This quantitative harmony between two sets of results points to the accuracy of our proposed approach for the theoretical treatment of multiferroic composites with coated fibers.

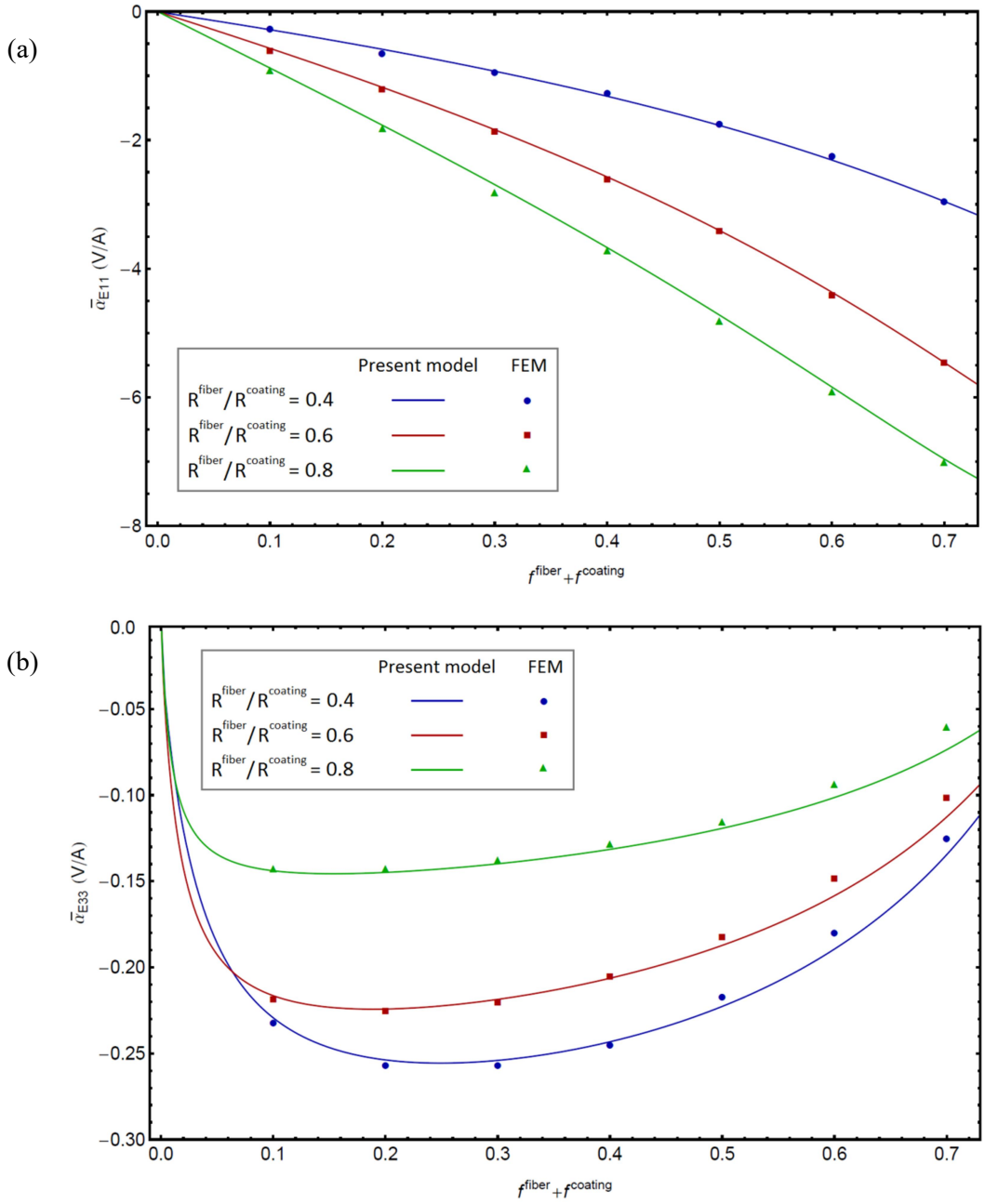

Fig. 2.3. Effective magneto-electric voltage coefficient of a fibrous BTO/CFO/TD composite, (a) $\bar{\alpha}_{E11}$ and (b) $\bar{\alpha}_{E33}$, in comparison with the FEM results of Kuo and Peng (2013).

Table 2.2. Effective moduli of a fibrous BTO/TD/CFO composite for different volume fraction of BTO/TD fibers ($R^{\text{fiber}} / R^{\text{coating}} = 0.8$).

$f^{\text{fiber}} + f^{\text{coating}}$		$\overline{C}_{2323}$ (GPa)	$\overline{e}_{113}$ (C/m^2)	$\overline{\kappa}_{11}$ (nF/m)	$\overline{q}_{113}$ (N/Am)	$\overline{\mu}_{11}$ (μN/s^{2}C^2)	$\overline{\alpha}_{11}$ (Ns/VC)
0.2	Present model	42.0	0.020	0.049	390.6	390.1	15.7×10^{-12}
	Kuo (2011)	42.5	0.020	0.049	390.0	390.0	16.0×10^{-12}
0.4	Present model	38.93	0.040	0.097	276.4	255.3	36.8×10^{-12}
	Kuo (2011)	39.25	0.040	0.098	275.0	255.0	37.5×10^{-12}
0.6	Present model	36.26	0.058	0.144	177.5	140.9	62.1×10^{-12}
	Kuo (2011)	37.00	0.060	0.147	175.0	140.0	63.0×10^{-12}

2.3.3. Comparison with Yan et al. (2013) for TD/BTO/CFO composite

We now determine the effective moduli of a fibrous TD/BTO/CFO composite by utilizing the newly developed theory. A similar problem recently was studies by Yan et al. (2013), by utilizing the so-called eigenfunction expansion-variational (EEV) method. For the sake of comparison with their theoretical results, we now adopt the present theory to calculate the effective magneto-electric coefficient of composite, $\overline{\alpha}_{11}$, for two particular volume concentrations of TD/BTO inhomogeneity system, $f^{\text{fiber}} + f^{\text{coating}} = 0.3$ and 0.6. Our calculated results together with those of EEV model are illustrated in Fig. 2.4, as a function of the square of radius ratio, $(R^{\text{fiber}}/R^{\text{coating}})^2$. Here, R^{fiber} and R^{coating} stand for the radius of TD core and its BTO coating, respectively, such that $(R^{\text{fiber}}/R^{\text{coating}})^2 = f^{\text{fiber}} / (f^{\text{fiber}} + f^{\text{coating}})$. Needless to mention that limiting value of $R^{\text{fiber}}/R^{\text{coating}} \approx 0$ (or 1) indicates the TD fibers are coated by very thick (or very thin) BTO layers. From Fig. 2.4 one can examine the influence of coating thickness on the accuracy of our theoretical results.

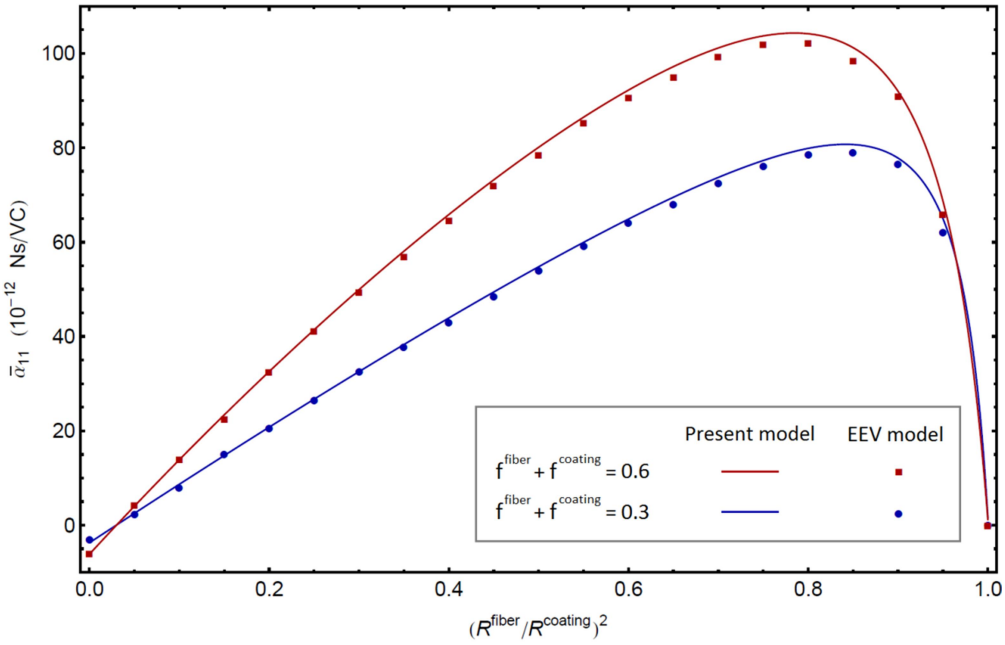

Fig. 2.4. Effective magnetoelectric constant of a fibrous TD/BTO/CFO composite, $\bar{\alpha}_{11}$, in comparison with the results given by Yan et al. (2013) for the similar composite.

2.3.4. CFO/BTO/Epoxy composite with FG interphase layer

Consider an epoxy material containing periodically distributed CFO fibers with BTO coating layers. We assume that an elastic interphase layer exists between the BTO coatings and the surrounding epoxy matrix. The stiffness, dielectric and permeability moduli of such a thin interphase is assumed to vary linearly from those of coating to the matrix, as

$$\begin{aligned} C_{ijkl}^{\text{interphase}} &= C_{ijkl}^{coating} + (C_{ijkl}^{matrix} - C_{ijkl}^{coating})(r - R^{\text{coating}})/t, \\ \kappa_{ij}^{\text{interphase}} &= \kappa_{ij}^{coating} + (\kappa_{ij}^{matrix} - \kappa_{ij}^{coating})(r - R^{\text{coating}})/t, \\ \mu_{ij}^{\text{interphase}} &= \mu_{ij}^{coating} + (\mu_{ij}^{matrix} - \mu_{ij}^{coating})(r - R^{\text{coating}})/t, \end{aligned} \tag{2.25}$$

where t is the thickness of interphase layer, r is the radial distance from the center of fiber, and R^{coating} is the radius of the outer boundary of BTO coating layer. We also consider various volume fractions for the interphase layer, $f^{\text{interphase}} / (f^{\text{fiber}} + f^{\text{coating}}) = 0$ (no interphase) and

0.05 and 0.1, so that one can examine the influence of thickness of the interphase layer on the overall response of multiferroic composite. It is notable in passing that in some real situations an undesirable phase undesirably forms between the inhomogeneities and the matrix, as a result of the chemical interactions during the manufacturing process of composite materials. The property of this transition zone can be functionally graded (FG), i.e. its composition varies continuously from the reinforcing fiber (or particle) to the surrounding matrix. In other situation, the FG interphase layers is deliberately applied to reinforcing fillers in order to reduce the large residual stress between constituent phases, prevent the matrix cracking during the manufacturing process, increase the fatigue and fracture strengths of composite materials, or improve their thermomechanical behavior for a reliable performance in high-temperature environments. Recognizing the potential gain that the FG coating could deliver, in present analysis we assumed the presence of such a thin layer with linearly varying properties between the CFO/BTO fibers and surrounding epoxy matrix.

The present formulation has been employed here to determine the effective properties of CFO/BTO/Epoxy composite material with various microstructures mentioned above. Our numerical results for the effective moduli $\overline{e}_{311}$, $\overline{q}_{311}$, $\overline{\alpha}_{\mathrm{E}11}$ and $\overline{\alpha}_{\mathrm{E}33}$ are illustrated in Fig. 2.5 (a)-(d), as a function of total volume fraction CFO fiber and its BTO coating, $f^{\mathrm{fiber}} + f^{\mathrm{coating}}$. For the sake of conciseness in the corresponding legends, the relative volume fraction of coating layer, $f^{\mathrm{coating}} / (f^{\mathrm{fiber}} + f^{\mathrm{coating}})$, and that of FG interphase, $f^{\mathrm{interphase}} / (f^{\mathrm{fiber}} + f^{\mathrm{coating}})$ have been represented by $\lambda^{\mathrm{coating}}$ and λ^{int}, respectively. A close look at Fig. 2.5 reveals some interesting characteristics of CFO/BTO/Epoxy composite material.

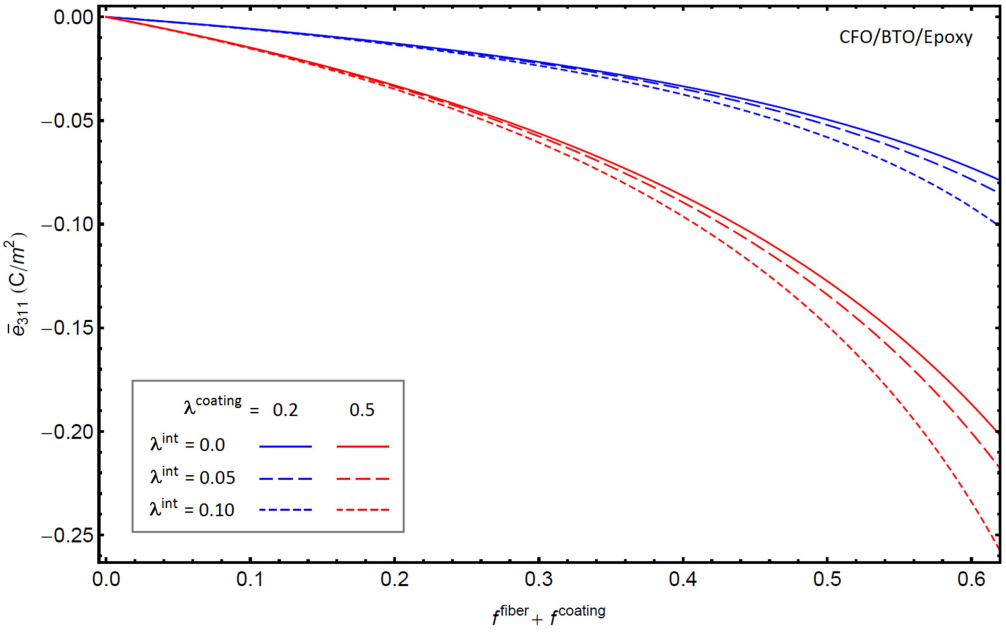
CFO/BTO/Epoxy
$\bar{e}_{311}$ (C/m^2)
$f^{fiber} + f^{coating}$
$\lambda^{coating}$ = 0.2 0.5
λ^{int} = 0.0
λ^{int} = 0.05
λ^{int} = 0.10

(a)

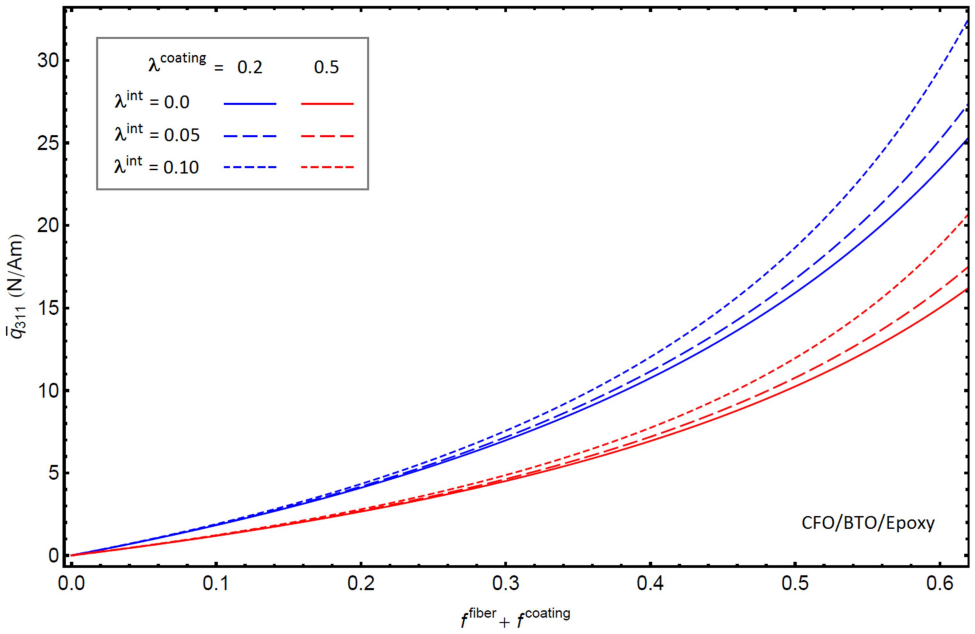
CFO/BTO/Epoxy
$\bar{q}_{311}$ (N/Am)
$f^{fiber} + f^{coating}$
$\lambda^{coating}$ = 0.2 0.5
λ^{int} = 0.0
λ^{int} = 0.05
λ^{int} = 0.10

(b)

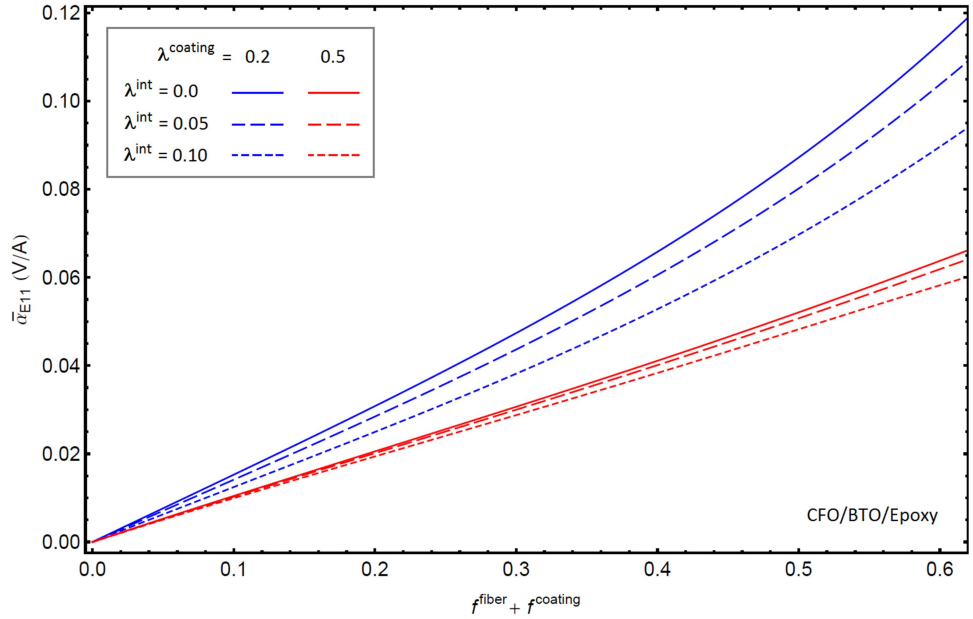

(c)

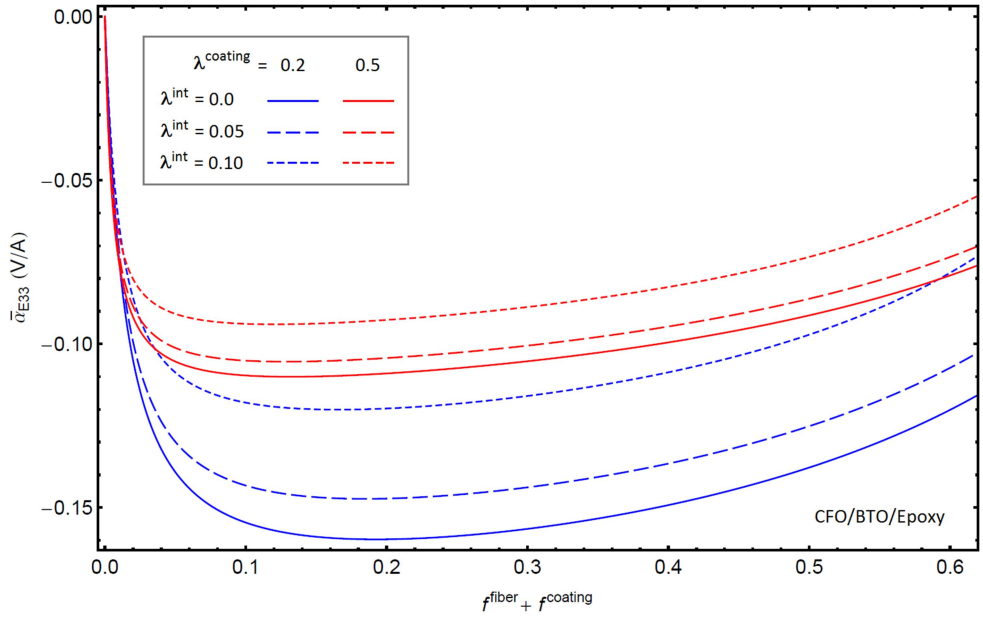

(d)

Fig. 2.5. Piezoelectric constant, $\bar{e}_{311}$, piezomagnetic constant, $\bar{q}_{311}$, and magneto-electric voltage coefficients, $\bar{\alpha}_{E11}$ and $\bar{\alpha}_{E33}$ of CFO/BTO/Epoxy composite with FG interphase layer between fibers and matrix. Note that $\lambda^{coating} = f^{coating} / (f^{fiber} + f^{coating})$ and $\lambda^{int} = f^{interphase} / (f^{fiber} + f^{coating})$.

For instance, it is evident from Fig. 2.5 (a) and (b) that at a given value for total volume fraction of CFO/BTO fibers, the overall piezoelectric (piezomagnetic) coefficient of composite material increases (decreases) with increasing the thickness of BTO coating, λ^{coating}. However, when we introduce the FG interphase layer around the CFO/BTO fillers, $\overline{e}_{311}$ and $\overline{q}_{311}$ both tend to increase. In fact, an increase in λ^{int} enhances both piezoelectric and piezomagnetic constants, although there is no electro-elastic and magneto-elastic coupling effects in the FG interphase layer. Besides, it is seen in Fig. 2.5(c) and (d) that the effective magneto-electric voltage coefficients of composite, $\overline{\alpha}_{\text{E11}}$ and $\overline{\alpha}_{\text{E33}}$ decrease with increasing the thickness of BTO coating, λ^{coating}. Moreover, for a given concentration of CFO fiber and its BTO coating, the introduction of such a FG interphase around the CFO/BTO fibers brings down the magneto-electric voltage coefficients of composite material; both $\overline{\alpha}_{\text{E11}}$ and $\overline{\alpha}_{\text{E33}}$ decrease when we increase the relative concentration of FG interphase layer, λ^{int}. Moreover, Fig. 2.5 in general illustrates that the influence of FG interphase on the overall response of multiferroic composite becomes more pronounced with increasing the volume fractions of CFO/BTO fibers, $f^{\text{fiber}} + f^{\text{coating}}$; as it can be expected.

2.3.5. Particulate BTO/CFO/Epoxy composite with weak interface

We now consider a multiferroic composite consisting of BTO spherical particles with CFO coatings, distributed periodically within an epoxy matrix. For now, the composite material is supposed to have a perfect interface condition; namely, the BTO/CFO particles are perfectly bonded to the epoxy matrix. However, we know that in reality the interface condition is not

perfect. The load transfer from matrix to reinforcing fillers can be significantly hindered due to the weak fillers/matrix surface condition; as a result, the imperfect interface has a profound influence on the overall behavior of composite materials. For a demonstration on the inevitable contribution that can be made by a weak interface condition, let us further assume that the interface between the BTO/CFO particles and the surrounding epoxy matrix is not perfect. To model this imperfect interface in the context of our proposed theory, we consider a very thin spherical layer of transition zone around the double-phase BTO/CFO particles. This diminishing layer (say interface) is then assumed to be significantly weaker than other constituent phases of composite material, as it is the case in the real situation. It is notable in passing that similar approach has been successfully adopted by Wang et al. (2015c) to address the issue of imperfect interface in random multiferroic composites.

We now employ present methodology to calculate the effective properties of abovementioned multiferroic composite, under distinct assumptions of perfect and weak interface conditions. In present analysis, three particular volume fractions have been considered for the BTO/CFO particle ensembles, $f^{\text{particle}} + f^{\text{coating}} = 0.2,\ 0.35$ and 0.5. On the other hand, the interface volume concentration is taken to to be 1% of the BTO/CFO particles, $f^{\text{interface}} = 0.01\ (f^{\text{particle}} + f^{\text{coating}})$. Besides, to illustrate the effect of weakened interface condition, following isotropic material properties have been assumed for the interface (Wang et al, 2015*c*),

$$\begin{aligned}
&C_{1111}^{\text{interface}} = 3\ \text{GPa}, \quad C_{1313}^{\text{interface}} = 1\ \text{GPa},\\
&\kappa_{11}^{\text{interface}} = 2\varepsilon_o, \quad \kappa_{33}^{\text{interface}} = 2\varepsilon_o \quad (\varepsilon_o = 8.85\times 10^{-12} \quad F/m),\\
&\mu_{11}^{\text{interface}} = 2\mu_o, \quad \mu_{33}^{\text{interface}} = 2\mu_o \quad (\mu_o = 1.257\times 10^{-6} \quad H/m).
\end{aligned} \tag{2.26}$$

Fig. 2.6(a)-(d) display our theoretical results for effective properties of composite materials, $\overline{e}_{311}$, $\overline{q}_{311}$, $\overline{\alpha}_{\text{E11}}$ and $\overline{\alpha}_{\text{E33}}$, as a function of the cube of radius ratio, $(R^{\text{particle}}/R^{\text{coating}})^3$. Here,

R^{particle} and R^{coating} stand for the radius of the BTO particle and its CFO coating, respectively. Needless to mention that $(R^{\text{particle}}/R^{\text{coating}})^3 = f^{\text{particle}}/(f^{\text{particle}}+f^{\text{coating}})$. At a fixed volume concentration of inhomogeneity system (i.e. $f^{\text{particle}}+f^{\text{coating}}$=*constant*), the limiting ratio of $R^{\text{particle}}/R^{\text{coating}} \approx 0$ (or 1) indicates that the BTO particles have been coated by very thick (or very thin) CFO layers. Fig. 2.6 reveals the complex nature of interplay between the various constituent phases of composite material. For instance, it is evident from Fig. 2.6(a) that, at a given volume concentration of BTO/CFO fillers, the overall piezoelectric constant increase with increasing the radius ratio, $R^{\text{particle}}/R^{\text{coating}}$. Fig. 2.6(b) shows an inverse trend for the effective piezomagnetic constant, such that $\overline{q}_{311}$ decreases when $R^{\text{particle}}/R^{\text{coating}}$ increases. However, Fig. 2.6(c) and 2.(d) show that there is a critical value for $R^{\text{particle}}/R^{\text{coating}}$ in which constants $\overline{\alpha}_{\text{E11}}$ and $\overline{\alpha}_{\text{E33}}$ reach to their maximum values. After their picks, both magneto-electric voltage coefficients decrease down to zero when $R^{\text{particle}}/R^{\text{coating}}$ approaches to limiting values of zero or one; as it can be expected. It is evident that the critical value of radius ratio is a function of the total volume fraction of BTO/CFO fillers. For instance, for the volume concentrations of $f^{\text{particle}}+f^{\text{coating}} = 0.2$ and 0.5, the maximum value of $\overline{\alpha}_{\text{E33}}$ have been achieved at different ratios of $(R^{\text{particle}}/R^{\text{coating}})^3 \approx 0.7$ and 0.6, respectively. Figs. 2.6(c) and (d) further demonstrate that the presence of a weak interface between BTO/CFO particles and surrounding epoxy brings up the effective magneto-electric voltage coefficients of composite material.

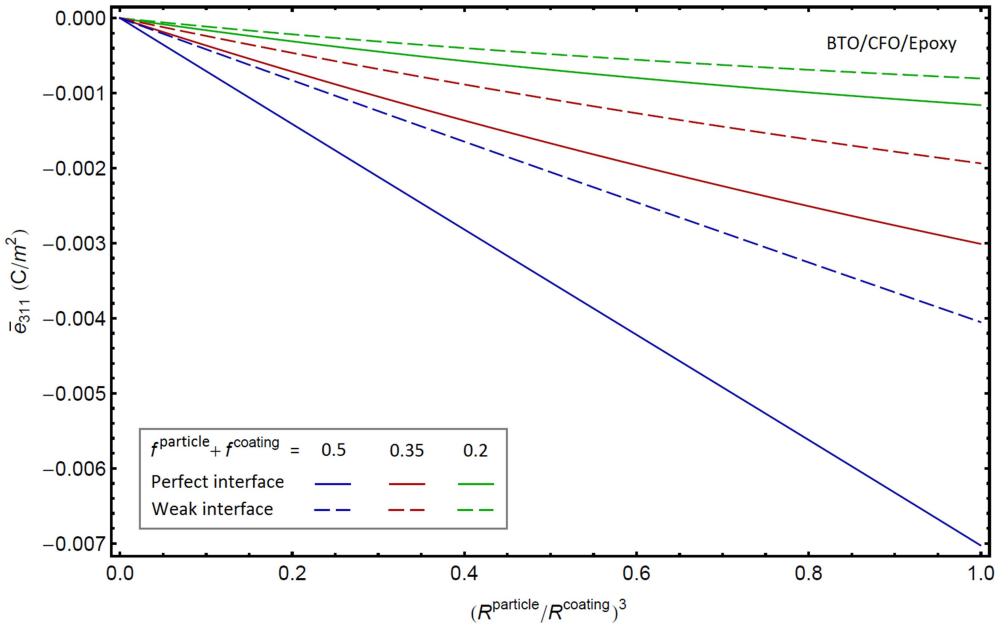
BTO/CFO/Epoxy
$f^{particle} + f^{coating}$ = 0.5 0.35 0.2
Perfect interface
Weak interface
$\bar{e}_{311}$ (C/m^2)
$(R^{particle}/R^{coating})^3$
0.000
−0.001
−0.002
−0.003
−0.004
−0.005
−0.006
−0.007
0.0
0.2
0.4
0.6
0.8
1.0

(a)

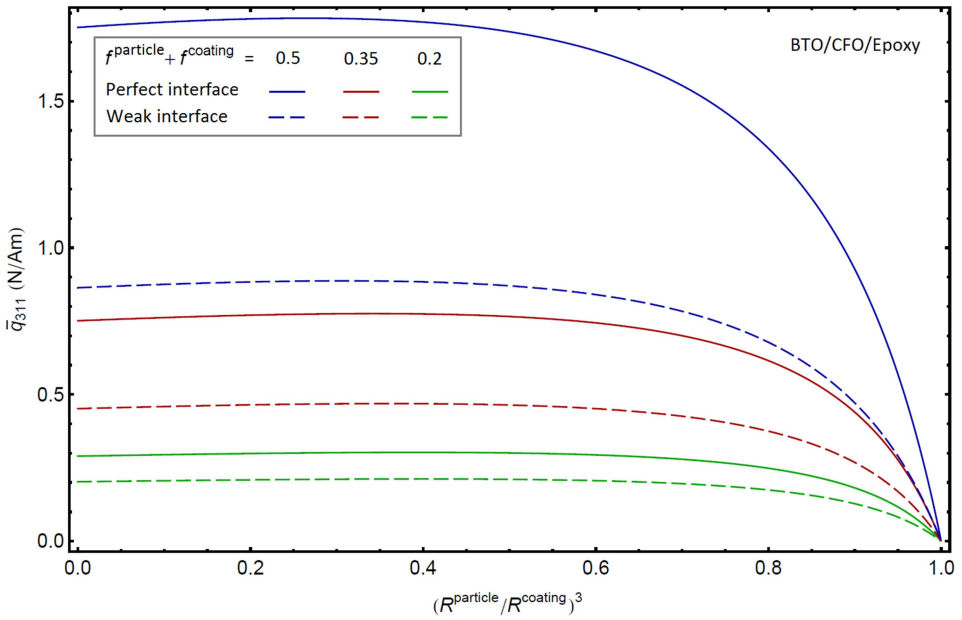
BTO/CFO/Epoxy
$f^{particle} + f^{coating}$ = 0.5 0.35 0.2
Perfect interface
Weak interface
$\bar{q}_{311}$ (N/Am)
$(R^{particle}/R^{coating})^3$
1.5
1.0
0.5
0.0
0.0
0.2
0.4
0.6
0.8
1.0

(b)

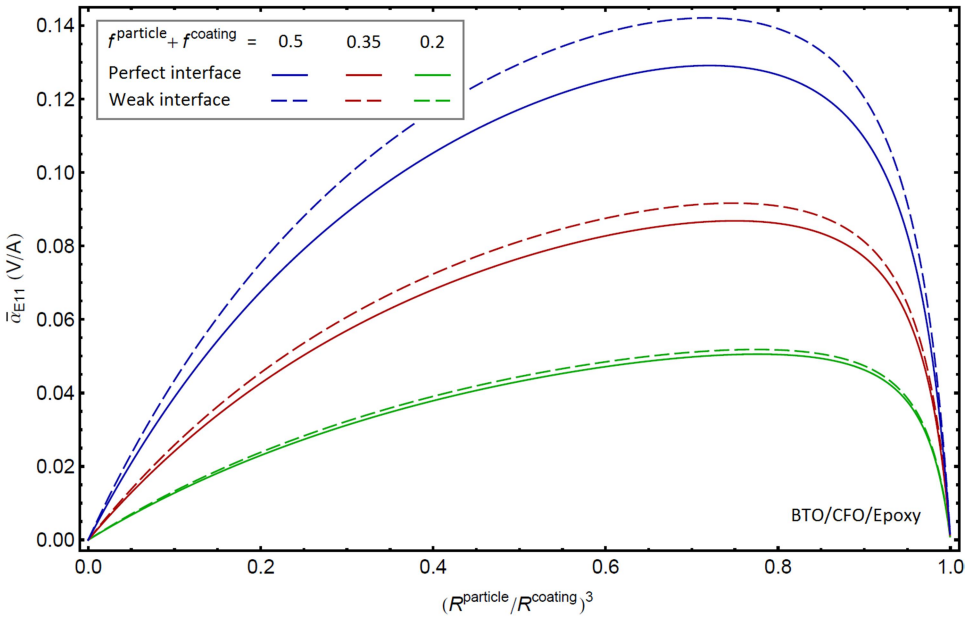

(c)

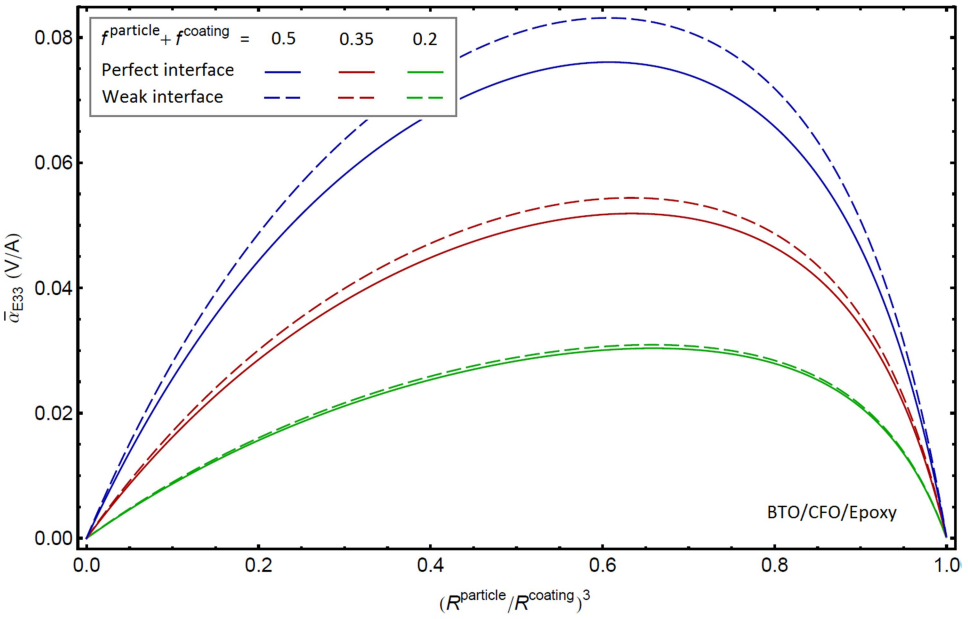

(d)

Fig. 2.6. Effective piezoelectric constant, $\bar{e}_{311}$, piezomagnetic modulus, $\bar{q}_{311}$, and magneto-electric voltage coefficients, $\bar{\alpha}_{E11}$ and $\bar{\alpha}_{E33}$ of a particulate BTO/CFO/Epoxy composite with perfect and weak interface condition between coated particles and matrix.

On the contrary, it is evident from Figs. 2.6(a) and (b) that the imperfect interface condition reduces the overall piezoelectric and piezomagnetic moduli of particulate BTO/CFO/Epoxy material. It is also observed that, in general, the interface condition has a more substantial influence on the piezoelectric and piezomagnetic constants, compared to its effects on the corresponding magneto-electric voltage coefficients.

2.3.6. Particulate BTO/CFO and CFO/BTO composites with eccentric void cores: coating layer with non-uniform thickness

Let us consider a multiferroic composite material consisting of BTO (or CFO) spherical particles distributed periodically within a CFO (or BTO) matrix. We further assume that an eccentric spherical void core has been located inside each BTO (or CFO) particle. Such a configuration for the double-phase inhomogeneity system with eccentricity vector $\boldsymbol{\delta}$ is schematically shown in Fig. 2.7. In present analysis, the void core is assumed to take various volume concentrations, denoted by the ratio $f^{void}/f^{particle}=0$ (no void core), 0.1 and 0.2. Besides, three different cases of eccentricity are considered for the void, as

- Case 1: $\delta_1/R^{\text{particle}}=0,\ \delta_2/R^{\text{particle}}=0,\ \delta_3/R^{\text{particle}}=0$ (Concentric void core)
- Case 2: $\delta_1/R^{\text{particle}}=0,\ \delta_2/R^{\text{particle}}=0,\ \delta_3/R^{\text{particle}}=0.3$
- Case 3: $\delta_1/R^{\text{particle}}=0.3,\ \delta_2/R^{\text{particle}}=0,\ \delta_3/R^{\text{particle}}=0$

in which R^{particle} is the radius of spherical piezoelectric (or piezomagnetic) particle.

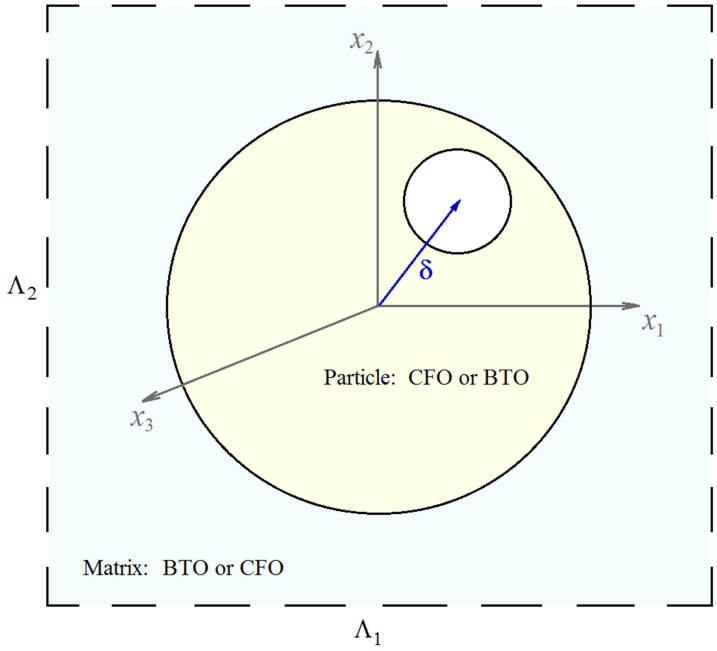

Fig. 2.7. A spherical particle with eccentric void core contained in the RVE. This typical configuration pertains to the particulate BTO/CFO and CFO/BTO composites.

Employing the developed theory, the foregoing set of problems has been solved for the particle volume fraction of f^{particle} =0.4. For the sake of demonstration, our calculated results for the effective stiffness, piezoelectric and piezomagnetic moduli of BTO/CFO and CFO/BTO composites with abovementioned microstructures are listed in Tables 2.3 and 2.4, respectively. It is seen that the multiferroic composite exhibits an overall tetragonal symmetry for case of 1 and 2 of eccentricity, but for the case 3 it is orthogonal. The calculated results demonstrate that, in general, the effective properties of multiferroic composites strongly depend on the microstructure of their constituent phases.

Table 2.3. (a) Effective elastic properties of BTO/CFO multiferroic composite consisting of spherical particles with eccentric void core, calculated at volume fraction of f^{particle} =0.4.

$\frac{\delta}{R^{particle}}$	$\frac{f^{void}}{f^{particle}}$	$\bar{C}_{1111}$	$\bar{C}_{1212}$	$\bar{C}_{1122}$	$\bar{C}_{3333}$	$\bar{C}_{1313}$	$\bar{C}_{1133}$	$\bar{C}_{2222}$	$\bar{C}_{2323}$	$\bar{C}_{2233}$
—	0	226.5	52.2	122.0	227.6	48.9	120.1	226.5	48.9	120.1
$\delta_1/R=0$	0.1	204.4	48.5	107.4	205.5	45.0	106.3	204.4	45.3	106.3
$\delta_2/R=0$	0.2	185.3	45.1	95.1	185.9	41.4	94.5	185.3	41.5	94.5
$\delta_3/R=0$										
$\delta_1/R=0$	0.1	199.3	47.6	104.0	209.8	45.3	105.1	199.3	45.3	105.1
$\delta_2/R=0$	0.2	177.5	43.7	90.3	193.6	41.8	92.8	177.5	41.8	92.8
$\delta_3/R=0.3$										
$\delta_1/R=0.3$	0.1	209.1	48.7	107.1	201.2	45.1	105.8	199.8	44.0	104.4
$\delta_2/R=0$	0.2	193.3	45.4	94.8	179.3	41.5	93.9	178.3	39.9	91.7
$\delta_3/R=0$										

Table 2.3. (b) Effective piezoelectric and piezomagnetic properties of BTO/CFO composite consisting of spherical particles with eccentric void core, at volume fraction of f^{particle} =0.4.

$\frac{\delta}{R^{particle}}$	$\frac{f^{void}}{f^{particle}}$	$\bar{e}_{333}$	$\bar{e}_{311}$	$\bar{e}_{113}$	$\bar{e}_{322}$	$\bar{e}_{223}$	$\bar{q}_{333}$	$\bar{q}_{311}$	$\bar{q}_{113}$	$\bar{q}_{322}$	$\bar{q}_{223}$
—	0	0.255	-0.049	0.158	-0.049	0.158	337.7	265.4	264.0	265.4	264.0
$\delta_1/R=0$	0.1	0.270	-0.029	0.155	-0.029	0.155	318.7	247.5	258.6	247.5	258.6
$\delta_2/R=0$	0.2	0.283	-0.012	0.151	-0.012	0.151	302.3	232.2	253.3	232.2	253.3
$\delta_3/R=0$											
$\delta_1/R=0$	0.1	0.273	-0.032	0.162	-0.032	0.162	319.9	244.3	259.0	244.3	259.0
$\delta_2/R=0$	0.2	0.288	-0.019	0.165	-0.019	0.165	304.8	227.6	253.9	227.6	253.9
$\delta_3/R=0.3$											
$\delta_1/R=0.3$	0.1	0.270	-0.032	0.151	-0.016	0.148	315.9	248.6	258.7	245.0	257.2
$\delta_2/R=0$	0.2	0.28	-0.018	0.145	-0.10	0.140	298.1	234.3	253.4	228.7	251.0
$\delta_3/R=0$											

Table 2.4. (a) Effective elastic properties of a CFO/BTO multiferroic composite consisting of spherical particles with eccentric void core, calculated at volume fraction of f^{particle} =0.4.

$\frac{\delta}{R^{particle}}$	$\frac{f^{void}}{f^{particle}}$	$\bar{C}_{1111}$	$\bar{C}_{1212}$	$\bar{C}_{1122}$	$\bar{C}_{3333}$	$\bar{C}_{1313}$	$\bar{C}_{1133}$	$\bar{C}_{2222}$	$\bar{C}_{2323}$	$\bar{C}_{2233}$
—	0	202.7	48.9	104.7	200.9	45.1	105.3	202.7	48.9	104.7
$\delta_1/R=0$	0.1	181.2	45.3	90.5	177.8	41.9	90.2	181.2	41.9	90.2
$\delta_2/R=0$	0.2	162.4	41.9	78.4	157.9	38.9	77.7	162.4	38.9	77.7
$\delta_3/R=0$										
$\delta_1/R=0$	0.1	177.3	44.6	87.9	182.7	41.9	90.0	177.3	44.6	87.9
$\delta_2/R=0$	0.2	156.4	40.7	74.8	166.4	38.8	77.6	156.4	40.7	74.8
$\delta_3/R=0.3$										
$\delta_1/R=0.3$	0.1	185.4	45.5	89.2	172.9	41.9	89.3	174.9	41.3	86.5
$\delta_2/R=0$	0.2	170.0	42.1	77.0	150.7	38.9	76.8	152.8	38.0	72.5
$\delta_3/R=0$										

Table 2.4. (b) Effective piezoelectric and piezomagnetic properties of a CFO/BTO composite consisting of spherical particles with eccentric void core, at volume fraction of f^{particle} =0.4.

$\frac{\delta}{R^{particle}}$	$\frac{f^{void}}{f^{particle}}$	$\bar{e}_{333}$	$\bar{e}_{311}$	$\bar{e}_{113}$	$\bar{e}_{322}$	$\bar{e}_{223}$	$\bar{q}_{333}$	$\bar{q}_{311}$	$\bar{q}_{113}$	$\bar{q}_{322}$	$\bar{q}_{223}$
—	0	8.82	-2.7	5.97	-2.76	5.97	46.8	34.6	10.5	34.6	10.6
$\delta_1/R=0$	0.1	8.91	-2.41	5.83	-2.41	5.83	44.1	32.2	10.5	32.2	10.5
$\delta_2/R=0$	0.2	8.98	-2.10	5.70	-2.10	5.7	41.6	30.0	10.4	30.0	10.4
$\delta_3/R=0$											
$\delta_1/R=0$	0.1	9.02	-2.30	5.83	-2.30	5.83	44.3	30.9	10.8	30.9	10.8
$\delta_2/R=0$	0.2	9.15	-1.93	5.70	-1.93	5.70	42.1	27.8	11.1	27.8	11.1
$\delta_3/R=0.3$											
$\delta_1/R=0.3$	0.1	8.90	-2.48	5.84	-2.35	5.81	43.2	32.6	10.32	31.4	10.30
$\delta_2/R=0$	0.2	8.95	-2.23	5.70	-2.01	5.6	40.1	30.8	10.1	28.6	10.0
$\delta_3/R=0$											

2.4. Concluding remarks

In this chapter, a micromechanical homogenization scheme has been developed to determine the effective moduli of a multiferroic composite containing periodic distribution of multiphase inhomogeneities. To treat the multi-coated inhomogeneity, we have divided it into different regions, and then each replaced by an inclusion system with certain amount of equivalent eigenstrain-electric-magnetic fields. Due to the periodic structure, the eigenfields are expanded in terms of the Fourier series. In conjunction with a superposition scheme, the local form of equivalent inclusion principle is then called upon, and integrated to give expressions for the average eigenfields. Finally, upon consideration of energy equivalency criterion the overall effective moduli of composite are obtained in terms of the derived average eigenstrain-electric-magnetic fields. This newly developed scheme is quite robust. It can be applied to a wide range of complex systems where the coating does not have to be thin, the shape and orientation of the core and coatings do not have to be the same, the layout of the coated layers can be eccentric, the properties of each layer can be functionally-graded, and the periodically distributed particles can be of the 2-D elliptic or the 3-D ellipsoidal shape. In this scheme the short-range inter-phase interactions, the particle-matrix interactions, and the long-range interactions between the periodically distributed inhomogeneities have all been fully accounted for, so the theory is applicable to high volume concentration and high property contrast problems. In view of the generality and efficacy of proposed methodology, we applied it to examine the properties of several multiferroic composites with different microstructures. The calculated results revealed the complex nature of interplay between the properties of core, matrix, and coating, as well as whether the coating is uniform, functionally

graded, or eccentric. In addition, the influence of imperfect interface condition on the overall magneto-electro-elastic behavior of three-phase composites has been well demonstrated. It is hopeful that the proposed theory can serve as a simple and yet widely useful tool for further development of high performance multiferroic composites with the optimized microstructures.

Chapter 3.

Magneto-electro-elastic scattered fields of a SH-wave induced by a two-phase multiferroic fiber in a piezoelectric or piezomagnetic medium

3.1. Overview

In many practical applications the devices incorporating piezoelectric-piezomagnetic multiferroic materials may be subjected to dynamics loadings. Accordingly, the study of wave propagation in multifrroic composites, and pertinent scattering phenomenon by the multi-phase inhomogeneities made of distinct piezoelectric and piezomagnetic materials is of great theoretical and practical interest. To date, the subject of wave propagation in the elastic heterogeneous media has been extensively studied during past decades; see, for example the fundamental works of Eringen and Suhubi (1975), Mikata and Nemat-Nasser (1991), Liu and Kriz (1996), Shindo et al. (1997) Selsil et al. (2001), Sato and Shindo (2001), and Michelitsch et al. (2003). However, only a few investigations addressing the wave propagation phenomenon in a piezoelectric-piezomagnetic media have been reported in the literature. Chen and Shen (2007) extended the work of Levin et al. (2002), who studied the elastic wave propagation in composites with piezoelectric fibers, to multiferroic composites. They first solved the problem associated with a single cylindrical fiber, and then considered the problem associated with multiple fibers by employing the effective field approach. Soh and Liu (2006) studied the propagation of an interfacial SH-wave in two bonded semi-infinite

piezoelectric-piezomagnetic materials. Chen et al. (2007) presented an analytical treatment for the propagation of harmonic waves in magneto-electro-elastic multilayered plates. Liu et al (2007) and Wang et al. (2007) demonstrated the propagation of a SH-wave in a semi-infinite medium with magneto-elastic coupling effect and hexagonal symmetry. Pang et al. (2008) and Liu et al. (2008) investigated the propagation of Rayleigh-type surface waves and Love waves in a piezoelectric-piezomagnetic layered half-space. Effects of the imperfect interface on SH-waves in two-phase multiferroic composites were also studied by Du et al. (2004), Huang et al. (2009), Sun et al. (2011) and Kuo and Yu (2014). Overall, to the best of author's knowledge none of these treatments addresses the dynamics problem with greater generality associated with the wave scattering phenomenon in a three-phase multiferroic medium, in which the constituent phases (i.e. fiber, coating and matrix) may consist of different piezoelectric and piezomagnetic materials. The present chapter aims to formulate a robust analytical methodology, named as magneto-electro-mechanical dynamics equivalent inclusion method (DEIM), which is suitable for studying the scattering of SH-waves by a multiferroic fiber-coating system embedded in piezoelectric or piezomagnetic matrix. For further generalization of problem, we consider an eccentric configuration for the coating-fiber ensemble.

3.2. The theory

3.2.1. Problem statement and basic constitutive equations

As shown in Fig. 3.1, consider a two-phase cylindrical fiber with circular cross-section, in which the core, Ω_1 and its coating layer, Ω_2 are made of different piezoelectric and piezomagnetic materials. The fiber ensemble, $\Omega_1 \cup \Omega_2$ is embedded in another piezoelectric or piezomagnetic medium, D. The regions Ω_1 and $\Omega_1 \cup \Omega_2$ with radii, respectively, R_1 and R_2 are assumed to be generally eccentric; thus, the thickness of interphase layer is non-uniform. The origin of Cartesian coordinate system (x_1, x_2, x_3), and corresponding polar coordinates (r,θ) in x_1x_2-plane are set at the center of core fiber. To keep the symmetry with respect to x_1-axis, we further assume that the center of region $\Omega_1 \cup \Omega_2$ is located at ($-\delta$,0,0), where δ stand for the eccentricity between Ω_1 and $\Omega_1 \cup \Omega_2$ (Fig. 3.1). As mentioned above, regions Ω_1, Ω_2 and D consist of distinct transversely isotropic piezoelectric and piezomagnetic materials. The x_3-axis is then assumed to be the axis of rotational symmetry which coincides with the poling and magnetization directions of available piezoelectric and piezomagnetic materials, respectively. It is known that the magneto-elastic (or electro-elastic) coupling is absent in an individual piezoelectric (or piezomagnetic) constituent phase. However, to present the succeeding mathematical formulation in a concise fashion, we write the linear constitutive equations of either piezoelectric or piezoelectric phases in the following unified format:

$$\begin{aligned} \sigma_{ij} &= C_{ijkl}\,\varepsilon_{kl} - e_{kij}E_k - q_{kij}H_k, \\ D_i &= e_{ikl}\,\varepsilon_{kl} + \kappa_{ik}\,E_k, \\ B_i &= q_{ikl}\,\varepsilon_{kl} + \mu_{ik}\,H_k, \end{aligned} \tag{3.1}$$

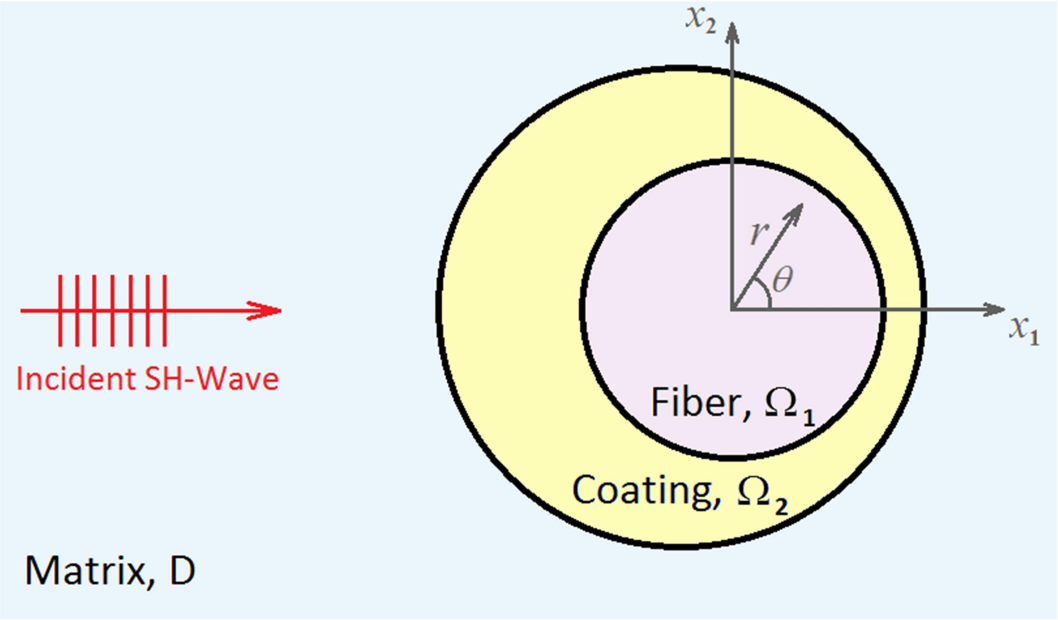

Fig. 3.1. Two-phase multiferroic fiber subjected to a SH-wave propagating in x_1-direction.

which simultaneously includes both electro-elastic and magneto-elastic coupling terms. The strain, electric field and magnetic field all can be derived from the gradients of displacement, u_i, and electric and magnetic potentials, ϕ and φ, respectively, as:

$$\begin{aligned} &\varepsilon_{ij} = \left(u_{i,j} + u_{j,i}\right)/2, \\ &E_i = -\phi_{,i}, \\ &H_i = -\varphi_{,i}. \end{aligned} \tag{3.2}$$

In addition, the balance of linear momentum in the absence of body forces, the Gauss's law, and the condition of no magnetic poles requires that the stress, electric displacement, and magnetic flux satisfy the following equilibrium equations:

$$\begin{aligned} &\sigma_{ij,j} = \rho \ddot{u}_i, \\ &D_{i,i} = 0, \\ &B_{i,i} = 0, \end{aligned} \tag{3.3}$$

where ρ is the mass density and symbol "." over a quantity indicates its time derivative.

Suppose that ascribed double-inhomogeneity system is subjected to an incident anti-plane SH-wave, $u_3^i(\boldsymbol{x},t)$ which is polarized along x_3-direction and is propagating in the positive x_1-direction, as schematically shown in Fig. 3.1. The incident wave in the matrix then may be described as following time harmonic functions:

$$
\begin{aligned}
&u_3^i(\boldsymbol{x},t) = u_0\, e^{i(\lambda r\cos\theta-\omega t)},\\
&\phi^i(\boldsymbol{x},t) = \frac{e}{\kappa}u_0\, e^{i(\lambda r\cos\theta-\omega t)},\\
&\varphi^i(\boldsymbol{x},t) = \frac{q}{\mu}u_0\, e^{i(\lambda r\cos\theta-\omega t)},
\end{aligned}
\tag{3.4}
$$

where $\phi^i(\boldsymbol{x},t)$ and $\varphi^i(\boldsymbol{x},t)$ are the incident electric and magnetic potentials, respectively, due to the electro-elastic and magneto-elastic coupling effects in the matrix. In above expressions, u_o denotes the amplitude of the incident SH-wave, ω is the circular frequency of the elastic wave, λ is the corresponding wave number. Note that when the matrix consists of a piezoelectric material, $\lambda=\omega\sqrt{\rho\kappa/(c\kappa+e^2)}$; otherwise, when the matrix is made of a piezomagnetic material, $\lambda=\omega\sqrt{\rho\mu/(c\mu+q^2)}$. Moreover, in Eq. (3.4) $c=C_{1313}$, $e=e_{113}$, $\kappa=\kappa_{11}$, $q=q_{113}$ and $\mu=\mu_{11}$ for the sake of brevity. At any field point the total displacement, $u_3(\boldsymbol{x},t)$, total electric field, $\phi(\boldsymbol{x},t)$, and total magnetic flux, $\varphi(\boldsymbol{x},t)$ can be written as:

$$
\begin{aligned}
&u_3(\boldsymbol{x},t) = u_3^i(\boldsymbol{x},t)+u_3^s(\boldsymbol{x},t),\\
&\phi(\boldsymbol{x},t) = \phi^i(\boldsymbol{x},t)+\phi^s(\boldsymbol{x},t),\\
&\varphi(\boldsymbol{x},t) = \varphi^i(\boldsymbol{x},t)+\varphi^s(\boldsymbol{x},t).
\end{aligned}
\tag{3.5}
$$

in which $u_3^s(\boldsymbol{x},t)$, $\phi^s(\boldsymbol{x},t)$ and $\varphi^s(\boldsymbol{x},t)$ are the scattered fields induced by the multiferroic double-inhomogeneity system. The scattered field has to be evaluated in such a way that the total fields satisfy the following governing equations:

$$\begin{aligned}
&(c+\Delta c)\nabla^2 u_3+(e+\Delta e)\nabla^2\phi+(q+\Delta q)\nabla^2\varphi=(\rho+\Delta\rho)\ddot{u}_3,\\
&(e+\Delta e)\nabla^2 u_3-(\kappa+\Delta\kappa)\nabla^2\phi=0,\\
&(q+\Delta q)\nabla^2 u_3-(\mu+\Delta\mu)\nabla^2\varphi=0.
\end{aligned} \tag{3.6}$$

This system of coupled differential equations has been obtained by utilizing Eqs. (3.1-3), in which ∇^2 stands for the two-dimensional Laplacian operator in the cylindrical coordinates. In addition, it was supposed that the material property $\mathcal{M}_i \equiv c_i, e_i, \kappa_i, \beta_i, q_i$, or μ_i belongs to the core fiber, Ω_1 for i =1, the coating layer, Ω_2 for i =2, and the matrix, D if no index is attached. Accordingly, $\Delta\mathcal{M}$ in Eq. (3.6) is defined as:

$$\Delta\mathcal{M}=\begin{cases}\mathcal{M}_1-\mathcal{M} & in \quad \Omega_1,\\ \mathcal{M}_2-\mathcal{M} & in \quad \Omega_2,\\ 0 & in \quad D.\end{cases} \tag{3.7}$$

3.2.2. Magneto-electro-mechanical dynamics equivalent inclusion method (DEIM)

We now propose an analytical micromechanics-based methodology, so-called Magneto-electro-mechanical DEIM, to calculate the scattered fields for the above-mentioned problem. It is noteworthy to mention that the DEIM was originally proposed by Fu and Mura (1983) for the determination of the elastic scattered fields of an ellipsoidal inhomogeneity subjected to time harmonic waves. The formulation of DEIM given by Fu and Mura (1983) has some shortcomings in employment of the notion of the homogenizing eigenstrain field. Sarvestani

el al. (2008), Shodja and Delfani (2009) and Shodja et al. (2014) remedied the shortcomings through introduction of the concept of eigenbody-force field and the pertinent consistency conditions. Moreover, they extended the theory to consider the elastic multi-inhomogeneity system with eccentricity. Extending their fundamental methodology to a multiferroic medium with constituent piezoelectric and piezomagnetic phases, we now replace the double-inhomogeneity ensemble with an equivalent double-inclusion system. As shown in Fig. 3.2, both regions of double-inclusion system are made of the same piezoelectric or piezomagnetic material as the matrix, but they are carrying appropriate distributions of time harmonic eigen fields, including eigen body-force, $Q_3^*(\boldsymbol{x},t)$, eigen stress, $\sigma_{3j}^*(\boldsymbol{x},t)$, eigen electric displacement, $D_j^*(\boldsymbol{x},t)$, eigen magnetic flux, $B_j^*(\boldsymbol{x},t)$ (j = 1 and 2). The magnitude of eigen fields can be determined on the basis that the stress fields, electric displacement, magnetic flux as well as their gradients must be identically equal in two equivalent double-inhomogeneity and double-inclusion systems. This scheme is called the magneto-electro-mechanical DEIM. For the double-inclusion problem, the governing differential equations in the presence of eigen fields become:

$$\begin{aligned} &c\,\nabla^2 u_3 + e\,\nabla^2\phi + q\,\nabla^2\varphi = \rho\,\ddot{u}_3 + Q_3^* + \sigma_{31,1}^* + \sigma_{32,2}^*, \\ &e\,\nabla^2 u_3 - \kappa\,\nabla^2\phi = D_{1,1}^* + D_{2,2}^*, \\ &q\,\nabla^2 u_3 - \mu\,\nabla^2\varphi = B_{1,1}^* + B_{2,2}^*. \end{aligned} \tag{3.8}$$

In view of Eq. (3.8), we may assume the time harmonic solutions for the total fields, as $u_3(\boldsymbol{x},t) = u(\boldsymbol{x})\,e^{-i\omega t}$, $\phi(\boldsymbol{x},t) = \phi(\boldsymbol{x})\,e^{-i\omega t}$ and $\varphi(\boldsymbol{x},t) = \varphi(\boldsymbol{x})\,e^{-i\omega t}$. Upon substitution of these functions with unknown amplitudes $u(\boldsymbol{x})$, $\phi(\boldsymbol{x})$ and $\varphi(\boldsymbol{x})$ into the governing Eq. (3.8), one can arrive at

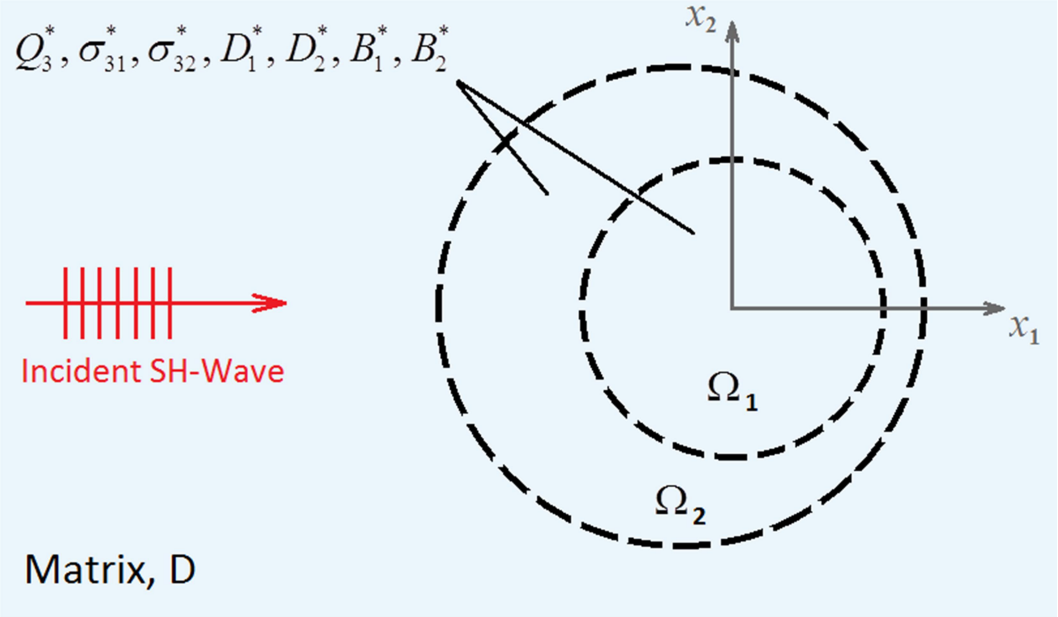

Fig. 3.2. Equivalent double-inclusion system carrying appropriate distribution of eigen fields.

$$
\begin{aligned}
&c\,\nabla^2 u_3(\boldsymbol{x}) + e\,\nabla^2\phi(\boldsymbol{x}) + q\,\nabla^2\varphi(\boldsymbol{x}) + \rho\omega^2 u_3(\boldsymbol{x}) = Q_3^*(\boldsymbol{x}) + \sigma_{31,1}^*(\boldsymbol{x}) + \sigma_{32,2}^*(\boldsymbol{x}),\\
&e\,\nabla^2 u_3(\boldsymbol{x}) - \kappa\,\nabla^2\phi(\boldsymbol{x}) = D_{1,1}^*(\boldsymbol{x}) + D_{2,2}^*(\boldsymbol{x}),\\
&q\,\nabla^2 u_3(\boldsymbol{x}) - \mu\,\nabla^2\varphi(\boldsymbol{x}) = B_{1,1}^*(\boldsymbol{x}) + B_{2,2}^*(\boldsymbol{x}).
\end{aligned}
\tag{3.9}
$$

Upon utilizing the Green's function technique, the amplitude of total fields then can be calculated by the simultaneous solution of Eqs. (3.9), as:

$$
\begin{aligned}
u_3(\boldsymbol{x}) = u_3^i(\boldsymbol{x}) &- \int_{\Omega_1\cup\Omega_2} G_{33}(\boldsymbol{x}-\boldsymbol{x}')\left[\sigma_{31,1}^*(\boldsymbol{x}') + \sigma_{32,2}^*(\boldsymbol{x}') + Q_3^*(\boldsymbol{x}')\right]d\boldsymbol{x}'\\
&- \int_{\Omega_1\cup\Omega_2} G_{34}(\boldsymbol{x}-\boldsymbol{x}')\left[D_{1,1}^*(\boldsymbol{x}') + D_{2,2}^*(\boldsymbol{x}')\right]d\boldsymbol{x}'\\
&- \int_{\Omega_1\cup\Omega_2} G_{35}(\boldsymbol{x}-\boldsymbol{x}')\left[B_{1,1}^*(\boldsymbol{x}') + B_{2,2}^*(\boldsymbol{x}')\right]d\boldsymbol{x}',\\
\phi(\boldsymbol{x}) = \phi^i(\boldsymbol{x}) &- \int_{\Omega_1\cup\Omega_2} G_{43}(\boldsymbol{x}-\boldsymbol{x}')\left[\sigma_{31,1}^*(\boldsymbol{x}') + \sigma_{32,2}^*(\boldsymbol{x}') + Q_3^*(\boldsymbol{x}')\right]d\boldsymbol{x}'\\
&- \int_{\Omega_1\cup\Omega_2} G_{44}(\boldsymbol{x}-\boldsymbol{x}')\left[D_{1,1}^*(\boldsymbol{x}') + D_{2,2}^*(\boldsymbol{x}')\right]d\boldsymbol{x}',
\end{aligned}
$$

$$\varphi(\boldsymbol{x}) = \varphi^{i}(\boldsymbol{x}) - \int_{\Omega_1 \cup \Omega_2} G_{53}(\boldsymbol{x}-\boldsymbol{x}') \left[\sigma^{*}_{31,1}(\boldsymbol{x}') + \sigma^{*}_{32,2}(\boldsymbol{x}') + Q^{*}_{3}(\boldsymbol{x}') \right] d\boldsymbol{x}' - \int_{\Omega_1 \cup \Omega_2} G_{55}(\boldsymbol{x}-\boldsymbol{x}') \left[B^{*}_{1,1}(\boldsymbol{x}') + B^{*}_{2,2}(\boldsymbol{x}') \right] d\boldsymbol{x}'. \tag{3.10}$$

Here $G_{ij}(\boldsymbol{x}-\boldsymbol{x}')$ (i, j = 3, 4 and 5) are the corresponding two-dimensional steady state Green's functions, associated with the propagation of the SH-wave in a transversely isotropic piezoelectric (or piezomagnetic) medium with electro-elastic (or magneto-elastic) coupling. For the piezoelectric matrix, the non-zero components of Green's function have been given by Levin et al. (2002), as:

$$\begin{aligned}
G_{33}(\boldsymbol{x}-\boldsymbol{x}') &= \frac{i\kappa}{4(c\kappa+e^2)} H_0^{(1)}\left(\lambda\left|\boldsymbol{x}-\boldsymbol{x}'\right|\right), \\
G_{34}(\boldsymbol{x}-\boldsymbol{x}') &= \frac{ie}{4(c\kappa+e^2)} H_0^{(1)}\left(\lambda\left|\boldsymbol{x}-\boldsymbol{x}'\right|\right), \quad G_{43}(\boldsymbol{x}-\boldsymbol{x}') = G_{34}(\boldsymbol{x}-\boldsymbol{x}'), \\
G_{44}(\boldsymbol{x}-\boldsymbol{x}') &= \frac{ie^2}{4(c\kappa^2+\kappa e^2)} H_0^{(1)}\left(\lambda\left|\boldsymbol{x}-\boldsymbol{x}'\right|\right) + \frac{1}{2\pi\kappa} ln\left|\boldsymbol{x}-\boldsymbol{x}'\right|, \\
G_{55}(\boldsymbol{x}-\boldsymbol{x}') &= \frac{1}{2\pi\mu} ln\left|\boldsymbol{x}-\boldsymbol{x}'\right|.
\end{aligned} \tag{3.11}$$

Likewise, when the matrix consists of a piezomagnetic material the non-zero components of corresponding Green's function become:

$$\begin{aligned}
G_{33}(\boldsymbol{x}-\boldsymbol{x}') &= \frac{i\mu}{4(c\mu+q^2)} H_0^{(1)}\left(\lambda\left|\boldsymbol{x}-\boldsymbol{x}'\right|\right), \\
G_{35}(\boldsymbol{x}-\boldsymbol{x}') &= \frac{iq}{4(c\mu+q^2)} H_0^{(1)}\left(\lambda\left|\boldsymbol{x}-\boldsymbol{x}'\right|\right), \quad G_{53}(\boldsymbol{x}-\boldsymbol{x}') = G_{35}(\boldsymbol{x}-\boldsymbol{x}'), \\
G_{44}(\boldsymbol{x}-\boldsymbol{x}') &= \frac{1}{2\pi\kappa} ln\left|\boldsymbol{x}-\boldsymbol{x}'\right|, \\
G_{55}(\boldsymbol{x}-\boldsymbol{x}') &= \frac{iq^2}{4(c\mu^2+\mu q^2)} H_0^{(1)}\left(\lambda\left|\boldsymbol{x}-\boldsymbol{x}'\right|\right) + \frac{1}{2\pi\mu} ln\left|\boldsymbol{x}-\boldsymbol{x}'\right|,
\end{aligned} \tag{3.12}$$

In Eqs. (3.11-12), $H_0^{(1)}$ is the Hankel function of the first kind of zero order.

According to the magneto-electro-mechanical DEIM, we now can enforce the consistency conditions between the double-inhomogeneity system and its equivalent double-inclusion

system. Subsequently, the equivalency of the stress, electric displacement and magnetic flux in Eq. (3.6) with the counterpart field variables in Eq. (3.8) leads to following coupled consistency conditions:

$$\begin{aligned}
&\Delta c\, u_{3,j}(\boldsymbol{x}) - \Delta e\, E_j(\boldsymbol{x}) - \Delta q\, H_j(\boldsymbol{x}) + \sigma^*_{3j}(\boldsymbol{x}) = 0, \quad j = 1, 2, \\
&\Delta\rho\,\omega^2\, u_3(\boldsymbol{x}) + Q^*_3(\boldsymbol{x}) = 0, \\
&\Delta e\, u_{3,j}(\boldsymbol{x}) + \Delta\kappa\, E_j(\boldsymbol{x}) + D^*_j(\boldsymbol{x}) = 0, \quad j = 1, 2, \\
&\Delta q\, u_{3,j}(\boldsymbol{x}) + \Delta\mu\, H_j(\boldsymbol{x}) + B^*_j(\boldsymbol{x}) = 0, \quad j = 1, 2.
\end{aligned} \tag{3.13}$$

Note that total displacement, electric potential and magnetic potential are already known in terms of the incident fields and unknown eigen fields, thanks to the Green's function solution given by Eqs. (3.10-12) for the equivalent double-inclusion problem. In this light, upon substitution of $u_3(\boldsymbol{x})$, $E_j(\boldsymbol{x})$ and $H_j(\boldsymbol{x})$ (j= 1, 2) from Eq. (3.10) into consistency equations (3.13), the exact solution to the unknown eigen fields can be conveniently obtained, as it will be explained in the next section.

3.2.3. Analytical solution procedure for determining eigen fields and scattered fields from consistency equations

Realizing the physical nature of this problem a priori, it will be proved useful to express all field quantities in the form of following series expansions. In so doing, the incident wave in the matrix may be expanded in terms of Fourier-Bessel series (Shodja et al., 2014), as:

$$\begin{aligned}
u^i_3(\boldsymbol{x}) &= u_0 \sum_{n=0}^{\infty} a_n i^n J_n(\lambda r)\cos(n\theta), \\
\phi^i(\boldsymbol{x}) &= \frac{e}{\kappa} u_0 \sum_{n=0}^{\infty} a_n i^n J_n(\lambda r)\cos(n\theta), \\
\varphi^i(\boldsymbol{x}) &= \frac{q}{\mu} u_0 \sum_{n=0}^{\infty} a_n i^n J_n(\lambda r)\cos(n\theta),
\end{aligned} \tag{3.14}$$

where J_n is the Bessel function of the first kind of order *n*. Moreover, the eigen fields over the double-inclusion system can be expressed in the following series form:

$$\left\{\sigma_{31}^{*}(\boldsymbol{x});Q_{3}^{*}(\boldsymbol{x});D_{1}^{*}(\boldsymbol{x});B_{1}^{*}(\boldsymbol{x})\right\}=\begin{cases}\sum_{n=0}^{\infty}\{f_n^{(1)}(r);f_n^{(3)}(r);f_n^{(4)}(r);f_n^{(6)}(r)\}\cos(n\theta), & \boldsymbol{x}\in\Omega_1,\\ \sum_{n=0}^{\infty}\{g_n^{(1)}(r);g_n^{(3)}(r);g_n^{(4)}(r);g_n^{(6)}(r)\}\cos(n\theta), & \boldsymbol{x}\in\Omega_2,\end{cases}$$

$$\left\{\sigma_{32}^{*}(\boldsymbol{x});D_{2}^{*}(\boldsymbol{x});B_{2}^{*}(\boldsymbol{x})\right\}=\begin{cases}\sum_{n=0}^{\infty}\{f_n^{(2)}(r);f_n^{(5)}(r);f_n^{(7)}(r)\}\sin(n\theta), & \boldsymbol{x}\in\Omega_1,\\ \sum_{n=0}^{\infty}\{g_n^{(2)}(r);g_n^{(5)}(r);g_n^{(7)}(r)\}\sin(n\theta), & \boldsymbol{x}\in\Omega_2,\end{cases} \tag{3.15}$$

where

$$\begin{aligned} f_n^{(j)}(r)&=\sum_{m=0}^{\infty}\left(A_{nm}^{(j)}J_m(\lambda r)+B_{nm}^{(j)}r^m\right), \qquad 0<r\le R_1,\\ g_n^{(j)}(r)&=\sum_{m=0}^{\infty}\left(C_{nm}^{(j)}J_m(\lambda r)+D_{nm}^{(j)}H_m^{(1)}(\lambda r)+K_{nm}^{(j)}r^m+L_{nm}^{(j)}r^{-m}\right), \qquad R_1<r<R_2, \end{aligned} \tag{3.16}$$

in which $H_m^{(1)}$ is the Hankel functions of the first kind of order *m*, and $A_{nm}^{(j)}$, $B_{nm}^{(j)}$, $C_{nm}^{(j)}$, $D_{nm}^{(j)}$, $K_{nm}^{(j)}$ and $L_{nm}^{(j)}$ (*j* = 1, 2, 3, 4, 5, 6 and 7) are the unknown coefficients to be determined. In addition, the Bessel and Hankel functions appeared in the Green's functions (11) and (12) can have the following representations in the cylindrical coordinate system (Shodja et al., 2014):

$$H_0^{(1)}\left(\lambda\left|\boldsymbol{x}-\boldsymbol{x}'\right|\right)=\begin{cases}\sum_{n=0}^{\infty}a_nJ_n(\lambda r)H_n^{(1)}(\lambda r')\cos[n(\theta-\theta')], & r<r',\\ \sum_{n=0}^{\infty}a_nJ_n(\lambda r')H_n^{(1)}(\lambda r)\cos[n(\theta-\theta')], & r>r',\end{cases}$$

$$\ln\left|\boldsymbol{x}-\boldsymbol{x}'\right|=\begin{cases}-\ln(r')+\sum_{n=1}^{\infty}\frac{1}{n}(\frac{r}{r'})^n\cos[n(\theta-\theta')], & r<r',\\ -\ln(r)+\sum_{n=1}^{\infty}\frac{1}{n}(\frac{r'}{r})^n\cos[n(\theta-\theta')], & r>r',\end{cases} \tag{3.17}$$

where $a_0 = 1$ and $a_n = 2$ for n = 1, 2, 3, … . In this expressions, (r, θ) and (r', θ') are associated with the Cartesian coordinates of the field and source points indicated by $\boldsymbol{x}$ and $\boldsymbol{x}'$, respectively.

Upon substitution of series expansions (3.14), (3.15) and (3.17) into the corresponding terms appearing in Eqs. (3.10-12), the analytical expressions for the total displacement, electric potential and magnetic potential can be obtained. To this end, a careful treatment of the involved integrals is required. The corresponding precise and rigorous remedy is given in Appendix. When the matrix is piezoelectric (i.e. q = 0), the scattred field quantities will have the following forms at a field point at $\boldsymbol{x} \in \Omega_1 \bigcup \Psi^* \bigcup \Psi^{**}$:

$$
\begin{aligned}
u_3^s(\boldsymbol{x}) = \sum_{n=0}^{\infty} \Bigg\{ & 2U_n^{(3)}(r) + \left[\frac{n+1}{r} + \frac{d}{dr}\right]\left[U_{n+1}^{(1)}(r) + U_{n+1}^{(2)}(r) + eU_{n+1}^{(4)}(r) + \mathrm{e}U_{n+1}^{(5)}(r)\right] \\
& - \left[\frac{n-1}{r} - \frac{d}{dr}\right]\left[U_{n-1}^{(1)}(r) - U_{n-1}^{(2)}(r) + eU_{n-1}^{(4)}(r) - eU_{n-1}^{(5)}(r)\right]\Bigg\}\cos(n\theta) \\
& + \frac{d}{dr}\left[U_0^{(1)}(r) + eU_0^{(4)}(r)\right]\cos\theta,
\end{aligned}
$$

$$
\begin{aligned}
\phi^s(\boldsymbol{x}) = \frac{e}{\kappa}u_3^s(\boldsymbol{x}) & - \sum_{n=1}^{\infty}\left[\frac{n}{r} + \frac{d}{dr}\right]\left[V_n^{(4)}(r) + V_n^{(5)}(r)\right]\cos\left[(n-1)\theta\right] \\
& + \sum_{n=1}^{\infty}\left[\frac{n}{r} - \frac{d}{dr}\right]\left[V_n^{(4)}(r) - V_n^{(5)}(r)\right]\cos\left[(n+1)\theta\right] + Z^{(4)}(r)\cos\theta,
\end{aligned}
$$

$$
\begin{aligned}
\varphi^s(\boldsymbol{x}) = & -\sum_{n=1}^{\infty}\left[\frac{n}{r} + \frac{d}{dr}\right]\left[V_n^{(6)}(r) + V_n^{(7)}(r)\right]\cos\left[(n-1)\theta\right] \\
& + \sum_{n=1}^{\infty}\left[\frac{n}{r} - \frac{d}{dr}\right]\left[V_n^{(6)}(r) - V_n^{(7)}(r)\right]\cos\left[(n+1)\theta\right] + Z^{(6)}(r)\cos\theta,
\end{aligned}
\tag{3.18}
$$

where regions Ψ^* and Ψ^{**} are defined in Appendix. Otherwise, when domain D is made of a piezomagnetic material (i.e. e = 0) the following expressions hold for the scattered fields at $\boldsymbol{x} \in \Omega_1 \bigcup \Psi^* \bigcup \Psi^{**}$:

$$
\begin{aligned}
u_3^s(\boldsymbol{x}) = \sum_{n=0}^{\infty} \Bigg\{ & 2W_n^{(3)}(r) + \left[\frac{n+1}{r} + \frac{d}{dr}\right]\left[W_{n+1}^{(1)}(r) + W_{n+1}^{(2)}(r) + qW_{n+1}^{(6)}(r) + qW_{n+1}^{(7)}(r)\right] \\
& - \left[\frac{n-1}{r} - \frac{d}{dr}\right]\left[W_{n-1}^{(1)}(r) - W_{n-1}^{(2)}(r) + qW_{n-1}^{(6)}(r) - qW_{n-1}^{(7)}(r)\right]\Bigg\}\cos(n\theta) \\
& + \frac{d}{dr}\left[W_0^{(1)}(r) + qW_0^{(4)}(r)\right]\cos\theta, \\
\phi^s(\boldsymbol{x}) = & -\sum_{n=1}^{\infty}\left[\frac{n}{r} + \frac{d}{dr}\right]\left[V_n^{(4)}(r) + V_n^{(5)}(r)\right]\cos\left[(n-1)\theta\right] \\
& + \sum_{n=1}^{\infty}\left[\frac{n}{r} - \frac{d}{dr}\right]\left[V_n^{(4)}(r) - V_n^{(5)}(r)\right]\cos\left[(n+1)\theta\right] + Z^{(4)}(r)\cos\theta, \\
\varphi^s(\boldsymbol{x}) = & \frac{q}{\mu}u_3^s(\boldsymbol{x}) - \sum_{n=1}^{\infty}\left[\frac{n}{r} + \frac{d}{dr}\right]\left[V_n^{(6)}(r) + V_n^{(7)}(r)\right]\cos\left[(n-1)\theta\right] \\
& + \sum_{n=1}^{\infty}\left[\frac{n}{r} - \frac{d}{dr}\right]\left[V_n^{(6)}(r) - V_n^{(7)}(r)\right]\cos\left[(n+1)\theta\right] + Z^{(6)}(r)\cos\theta.
\end{aligned}
\tag{3.19}
$$

Functions $U_n^{(j)}$, $W_n^{(j)}$, $V_n^{(j)}$ and $Z^{(j)}$ appearing in expressions (3.18) and (3.19) are given through Appendix. In view of Eqs. (3.18-19), we now have the analytical expressions for the total fields in terms of unknown coefficients appearing in Eq. (3.16) for the Fourier-Bessel series expansion of eigen fields. Subsequently, with the aid of consistency Eqs. (3.13) the coefficients $A_{nm}^{(j)}$, $B_{nm}^{(j)}$, $C_{nm}^{(j)}$, $D_{nm}^{(j)}$, $K_{nm}^{(j)}$ and $L_{nm}^{(j)}$ (j = 1, 2, 3, 4, 5, 6 and 7) can be determined. To this end, suppose that for N terms of the series in expressions (3.15) together with M terms of the series in Eq. (3.16) the eigen fields are represented with satisfactory accuracies. This assumption gives rise to 14 N x M unknowns, $A_{nm}^{(j)}$ and $B_{nm}^{(j)}$ pertinent to the region Ω_1 and 28 N x M unknowns, $C_{nm}^{(j)}$, $D_{nm}^{(j)}$, $K_{nm}^{(j)}$ and $L_{nm}^{(j)}$ associated with the coating Ω_2. Thus, for the complete determination of the unknown coefficients, the consistency Eq. (3.13) should be written at 2 N x M points inside Ω_1 and at 4 N x M points inside Ω_2 to obtain 42 N x M equations needed to solve for 42 N x M unknowns.

Once the eigen fields are obtained by abovementioned procedure, it is desirable to compute the scattered fields within the matrix. For the piezoelectric matrix, the scattered displacement, electric and magnetic potentials at $\boldsymbol{x} \in D - \left\{\Omega_1 \cup \Psi^* \cup \Psi^{**}\right\}$ are of the following form:

$$
\begin{aligned}
u_3^s(\boldsymbol{x}) &= \sum_{n=0}^{\infty} S_n^E H_n^{(1)}(\lambda r)\cos(n\theta), \\
\phi^s(\boldsymbol{x}) &= \frac{e}{\kappa} u_3^s(\boldsymbol{x}) + \sum_{n=1}^{\infty} \frac{\cos\left[(n+1)\theta\right]}{r^{n+1}}\left(\Gamma_n^{(4)} - \Gamma_n^{(5)}\right) + T^{(4)}(r)\cos\theta, \\
\varphi^s(\boldsymbol{x}) &= \sum_{n=1}^{\infty} \frac{\cos\left[(n+1)\theta\right]}{r^{n+1}}\left(\Gamma_n^{(6)} - \Gamma_n^{(7)}\right) + T^{(6)}(r)\cos\theta,
\end{aligned}
\tag{3.20}
$$

in which

$$
\begin{aligned}
S_0^E &= 2\xi_0^{(3)} + \lambda\left[\xi_0^{(1)} + \xi_0^{(2)} + \xi_0^{(4)} + \xi_0^{(5)}\right], \\
S_1^E &= 2\xi_1^{(3)} + \lambda\left[\xi_2^{(1)} + \xi_2^{(2)} + e\xi_2^{(4)} + e\xi_2^{(5)}\right] - 2\lambda\left[\xi_0^{(1)} + e\xi_0^{(4)}\right], \\
S_n^E &= 2\xi_n^{(3)} + \lambda\left[\xi_{n+1}^{(1)} + \xi_{n+1}^{(2)} + e\xi_{n+1}^{(4)} + e\xi_{n+1}^{(5)}\right] - \lambda\left[\xi_{n-1}^{(1)} - \xi_{n-1}^{(2)} + e\xi_{n-1}^{(4)} - e\xi_{n-1}^{(5)}\right], \quad n = 2,3,...
\end{aligned}
\tag{3.21}
$$

The expression for functions $T^{(j)}(r)$, $\Gamma_n^{(j)}$, and $\xi_n^{(j)}(r)$ (n = 0, 1, 2, …) appearing in (3.20-21) are given in Appendix. On the other hand, when matrix consists of a piezomagnetic material the scattered fields at $\boldsymbol{x} \in D - \left\{\Omega_1 \cup \Psi^* \cup \Psi^{**}\right\}$ can be calculated by following series:

$$
\begin{aligned}
u_3^s(\boldsymbol{x}) &= \sum_{n=0}^{\infty} S_n^M H_n^{(1)}(\lambda r)\cos(n\theta), \\
\phi^s(\boldsymbol{x}) &= \sum_{n=1}^{\infty} \frac{\cos\left[(n+1)\theta\right]}{r^{n+1}}\left(\Gamma_n^{(4)} - \Gamma_n^{(5)}\right) + T^{(4)}(r)\cos\theta, \\
\varphi^s(\boldsymbol{x}) &= \frac{q}{\mu} u_3^s(\boldsymbol{x}) + \sum_{n=1}^{\infty} \frac{\cos\left[(n+1)\theta\right]}{r^{n+1}}\left(\Gamma_n^{(6)} - \Gamma_n^{(7)}\right) + T^{(6)}(r)\cos\theta,
\end{aligned}
\tag{3.22}
$$

in which

$$
\begin{aligned}
S_0^M &= 2\eta_0^{(3)} + \lambda\left[\eta_0^{(1)} + \eta_0^{(2)} + \eta_0^{(6)} + \eta_0^{(7)}\right], \\
S_1^M &= 2\eta_1^{(3)} + \lambda\left[\eta_2^{(1)} + \eta_2^{(2)} + q\eta_2^{(6)} + q\eta_2^{(7)}\right] - 2\lambda\left[\eta_0^{(1)} + q\eta_0^{(6)}\right], \\
S_n^M &= 2\eta_n^{(3)} + \lambda\left[\eta_{n+1}^{(1)} + \eta_{n+1}^{(2)} + q\eta_{n+1}^{(6)} + q\eta_{n+1}^{(7)}\right] - \lambda\left[\eta_{n-1}^{(1)} - \eta_{n-1}^{(2)} + q\eta_{n-1}^{(6)} - q\eta_{n-1}^{(7)}\right], \quad n = 2,3,...
\end{aligned}
\tag{3.23}
$$

where the coefficients $\eta_n^{(j)}(r)$ (n = 0, 1, 2, …) are given in Appendix, as well.

This completes our micromechanics formulation for determining the scattered fields of an incident SH-wave over each of fiber, coating and matrix phases made of different piezoelectric and piezomagnetic materials.

3.3. Numerical results and discussion

In this section, through consideration of various examples the effects of several parameters, such as material properties and eccentricity of fiber and its coating, as well as the wave number of incident SH-wave on the scattering phenomenon in a multiferroic fiber are thoroughly examined. Along the way, the robustness and applicability of proposed theory also is well demonstrated. The material properties of constituent phases, used in the numerical calculations of this section, are listed in Table. 3.1.

Before we proceed, let us introduce the total scattering cross-section, Σ_{SH} which is an importance parameter with great practical interest in the non-destructive evaluations. This parameter is defined as the ratio of the mean scattered energy in all directions to the mean energy of the incident wave per unit area normal to the direction of propagation. Using expansions for Eqs. (3.20) and (3.22) at infinity and after some mathematical manipulations, the expression for the total scattering cross-section can be obtained, as:

$$\Sigma_{SH} = \frac{4}{\lambda}\sum_{n=0}^{\infty}\frac{1}{a_n}\left|\frac{S_n^E}{u_0}\right|^2 \tag{3.24}$$

and

$$\Sigma_{SH} = \frac{4}{\lambda}\sum_{n=0}^{\infty}\frac{1}{a_n}\left|\frac{S_n^M}{u_0}\right|^2 \tag{3.25}$$

Table 3.1. Magneto-electro-elastic properties of $BaTiO_3$ (BTO), $CoFe_2O_4$ (CFO), Terfenol-D (TD), Al, SiC and Epoxy.

Properties	BTO	CFO	TD	SiC	Al	Epoxy
c (GPa)	43.86	45.3	5.55	188.1	26.5	1.8
κ (nC^2/Nm^2)	11.2	0.08	0.05	0.088	0.016	0.037
μ ($\mu N/s^2C^2$)	5	590	8.64	1.4	1.26	2.51
e (C/m^2)	11.4	0	0	0	0	0
q (N/Am)	0	550	155.5	0	0	0
ρ (Kg/m^3)	6000	5200	9210	3181	2706	1202

for the piezoelectric or piezomagnetic matrixes, respectively. Needless to mention that the coefficients S_n^E and S_n^M in Eqs. (3.24) and (3.25) includes the effects of magneto-electro-elastic couplings in the corresponding constituent phases. In following numerical examples we evaluate the total scattering cross-section in different cases to examine the effect of various material parameters on the pertinent scattered fields.

3.3.1. Scattered fields by a SiC fiber with elastic coating layer in an Al matrix: Comparison with Shindo and Niwa (1996)

To verify the accuracy of present analytical solution, we first consider the problem of a cylindrical SiC fiber with concentric elastic interphase layer inside an infinite Al matrix. The material properties of the coating are assumed to be the mean value of those of the SiC fiber and Al matrix. This simple bench mark problem has been previously examined by Shindo and Niwa (1998), who utilized the wave-function expansion methodology to address the effect of interphase layer on the scattering of SH-wave in fibrous composites. So, this example will serve to make contact with the existing literature. To do so, we apply present

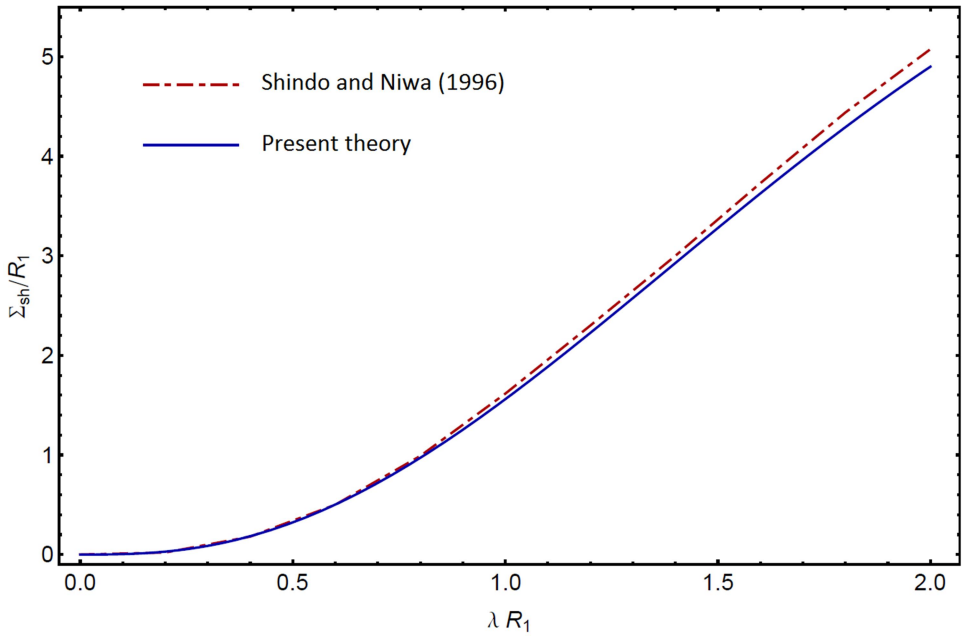

Fig. 3.3. Variation of dimensionless total scattering cross-section with normalized wave number, for a SiC fiber with elastic coating in Al matrix.

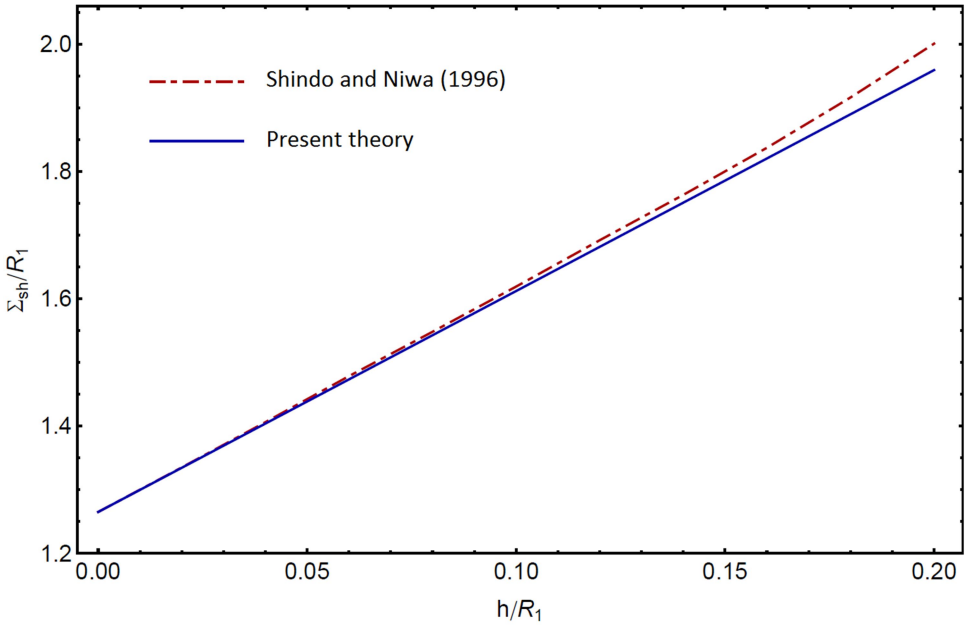

Fig. 3.4. Variation of dimensionless total scattering cross-section as a function of normalized thickness of coating layer, for a SiC fiber with elastic coating in Al matrix.

micromechanical theory to this problem, by considering just the first 6 terms of the expansions (3.15) and (3.16). For the coating thickness of $h = 0.1R_1$, the variation of dimensionless total scattering cross-section, $\sum_{SH}/R_1$ is computed, and displaced in Fig. 3.3 as a function of the normalized wave number, λR_1. Moreover, the effect of thickness of coating layer, h on the variation of $\sum_{SH}/R_1$ for a SH-wave with dimensionless wave number is depicted in Fig. 3.4. From Figs. 3.3 and 3.4 it can be readily observed that, for the entire range of wave numbers and coating thickness, our results are in good agreement with the previous solution reported by Shindo and Niwa (1996).

3.3.2. Scattered fields by a BTO fiber in a CFO matrix: Comparison with Kuo and Yu (2014)

For further validation of current analytical solution, the problem of a cylindrical BTO fiber embedded in an infinite CFO matrix subjected to a SH-wave is examined via present theory. Fig. 3.5 shows the dimensionless total scattering cross-section, $\sum_{SH}/R_1$ calculated in terms of the normalized wave number, λR_1. Our results in this figure are shown along with those of Kuo and Yu (2014); they utilized the wave-function expansion technique in their analysis. It is readily seen that two sets of results are in good quantitative agreement, even for high frequency ranges.

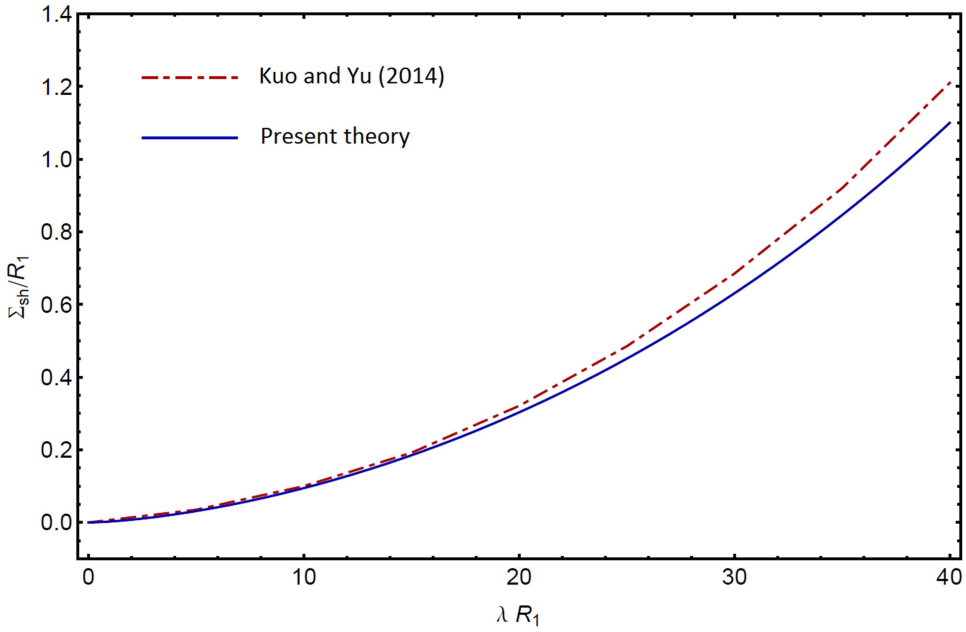

Fig. 3.5. Variation of dimensionless total scattering cross-section as a function of normalized wave number, for a BTO fiber in CFO matrix.

3.3.3. Scattered fields by a CFO fiber with concentric BTO coating embedded in a TD matrix

Consider a piezomagnetic fiber made of CFO material having a piezoelectric coating of uniform thickness which is made of BTO material. This two-phase multiferroic fiber is embedded in an infinite piezomagnetic medium made of TD material. An incident anti-plane SH-wave propagating in the TD matrix can be scattered by the CFO-BTO inhomogeneity system. By employing the present formulation at different dimensionless wave numbers ($\lambda R_1 = 0.5,\ 1,\ 2$ and 3), the total scattering cross-section, $\sum_{SH}/R_1$ is computed and displaced in Fig. 3.6 as a function of normalized coating thickness, h/R_1. It is evident that the effects of BTO interphase layer on the scattered fields is quite substantial; it causes a nearly linear increase in the dimensionless total scattering cross-section as h/R_1 varies from 0 to 0.25.

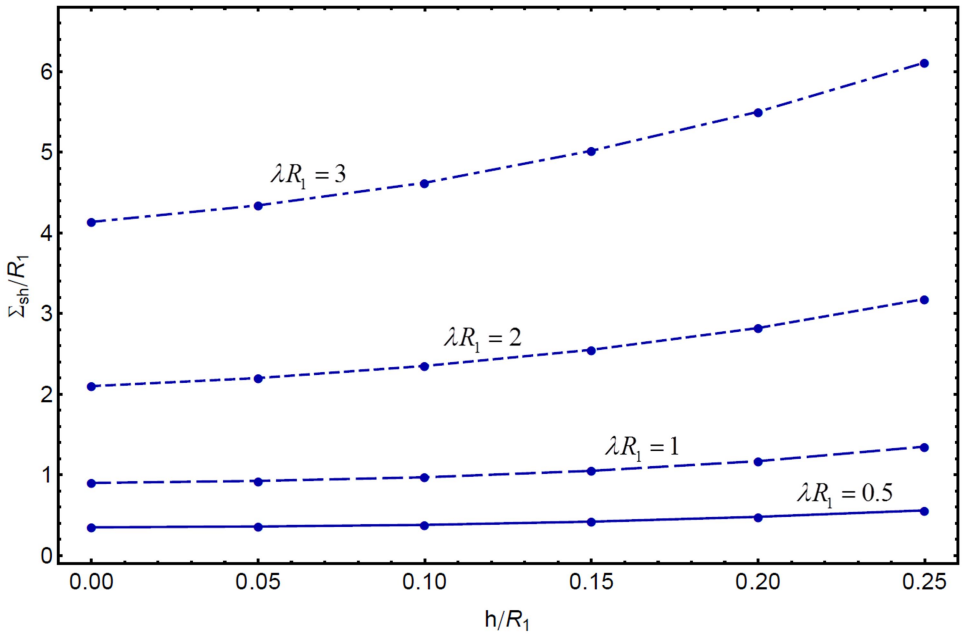

Fig. 3.6. Variation of dimensionless total scattering cross-section with normalized thickness of coating layer, for different wave numbers, λR_1. Results pertain to a CFO fiber with concentric BTO coating in a TD matrix.

Fig. 3.6 also shows that the effect of BTO coating on the scattered field is more pronounced at larger values of the wave number. For a demonstration of the convergence behavior of our solution, the trend of the convergence of Σ_{SH}/R_1 with the considered number of terms in the series expansion (3.15) are depicted in Fig. 3.7. The lower and upper curves pertains to different wave numbers of $\lambda R_1 = 1$ and 3, respectively, which have been obtained for the coating thickness of $h/R_1 = 0.1$. Fig. 3.7 shows that the discrepancy between the value of Σ_{SH}/R_1 corresponding to n = 6 and 7 is only about 1.7% for $\lambda R_1 = 1$ and 1.3% for $\lambda R_1 = 3$; this reveals the high convergence rate of the present solution.

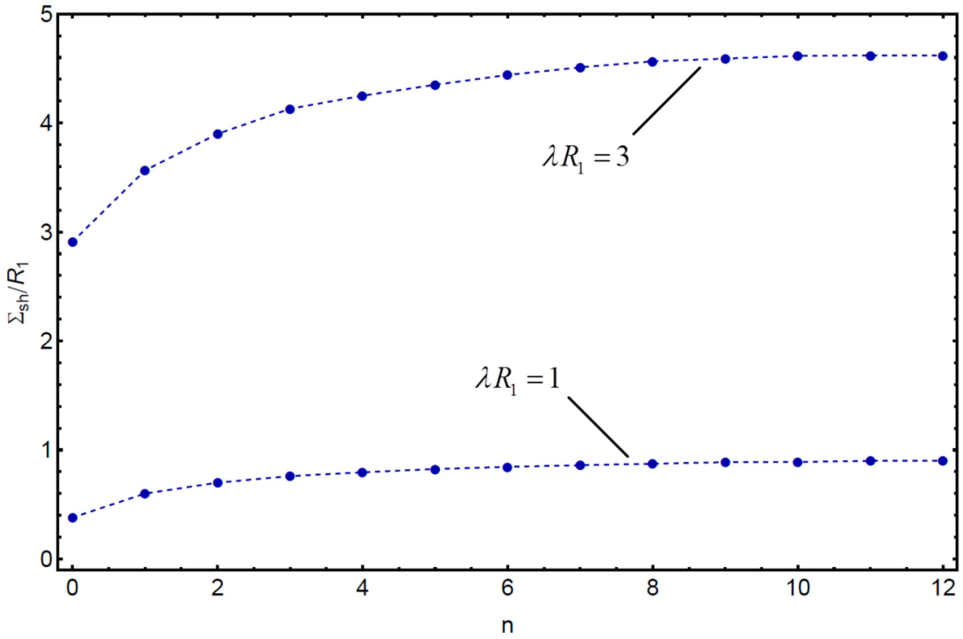

Fig. 3.7. Convergence of normalized total scattering cross-section with the number of terms, *n* considered in the corresponding series solution. Results pertain to a CFO fiber with concentric BTO coating in a TD matrix.

3.3.4. Scattered fields by a BTO fiber with eccentric CFO coating embedded in a TD matrix

This example is devoted to an eccentric double-inhomogeneity system, in which a BTO piezoelectric fiber is coated by a CFO piezomagnetic interphase with non-uniform thickness. The surrounding matrix is made of a TD piezomagnetic material. Throughout this example, the radius of the coating layer to that of fiber is $R_2/R_1 = 1.5$; however, three different coating eccentricity of $\delta/R_1 = 0$ (concentric), 0.2 and 0.4 are considered in our numerical calculations. The dimensionless wave number of incident SH-wave, λR_1 is allowed to vary from 0 to 4. The variations of the normalized total scattering cross-section, $\sum_{SH}/R_1$ in terms of the dimensionless wave number for abovementioned scenarios of eccentricity are illustrated in

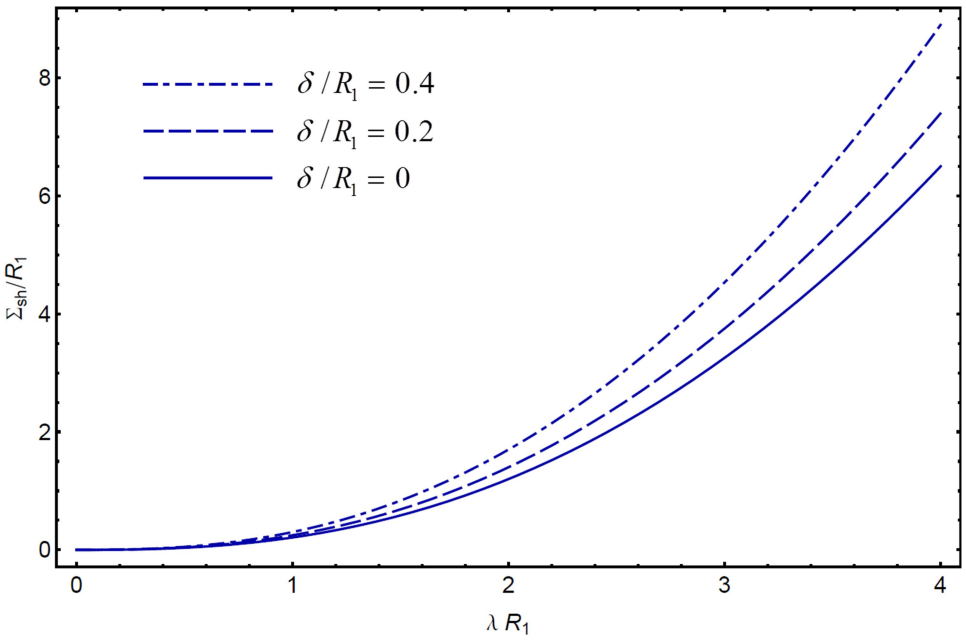

Fig. 3.8. The variations of the total scattering cross-section with the normalized wave number, for different coating eccentricities, δ / R_1. Results pertain to a BTO fiber with eccentric TD coating in a CFO matrix.

Fig. 3.8. It can be inferred from the figure that total scattering cross-sections tend to increase with increasing the wave number. Moreover, a comparison between different curves at a given wave number reveals that the value of Σ_{SH} increases with increasing the coating eccentricity, δ. This influence of coating eccentricity becomes more pronounced at larger value of the wave number. As a result, nearly beyond $\lambda R_1 = 1$ the difference between curves of Σ_{SH} / R_1 begins to show and become increasingly notifiable as λR_1 increases.

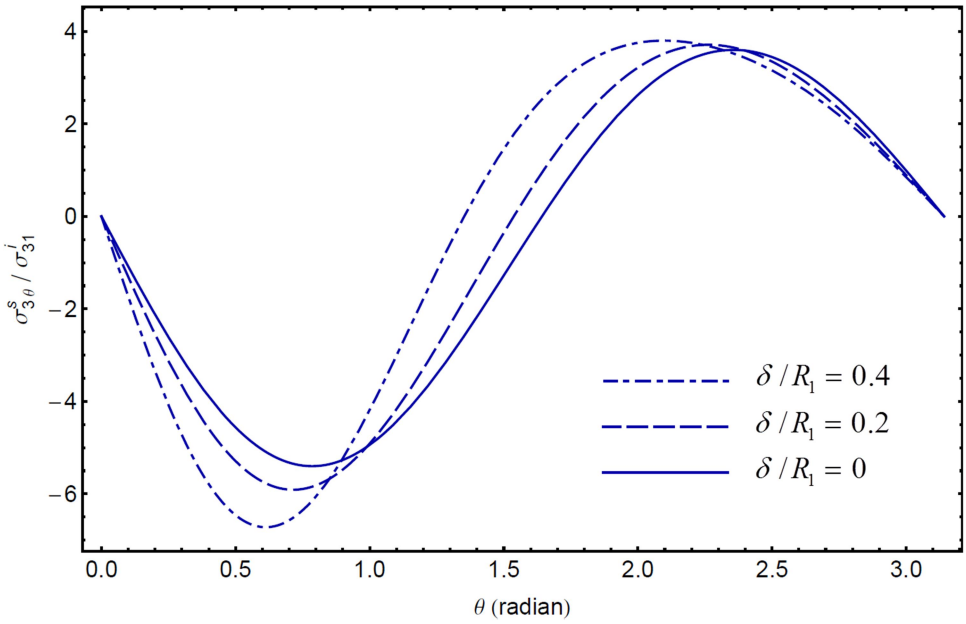

(a)

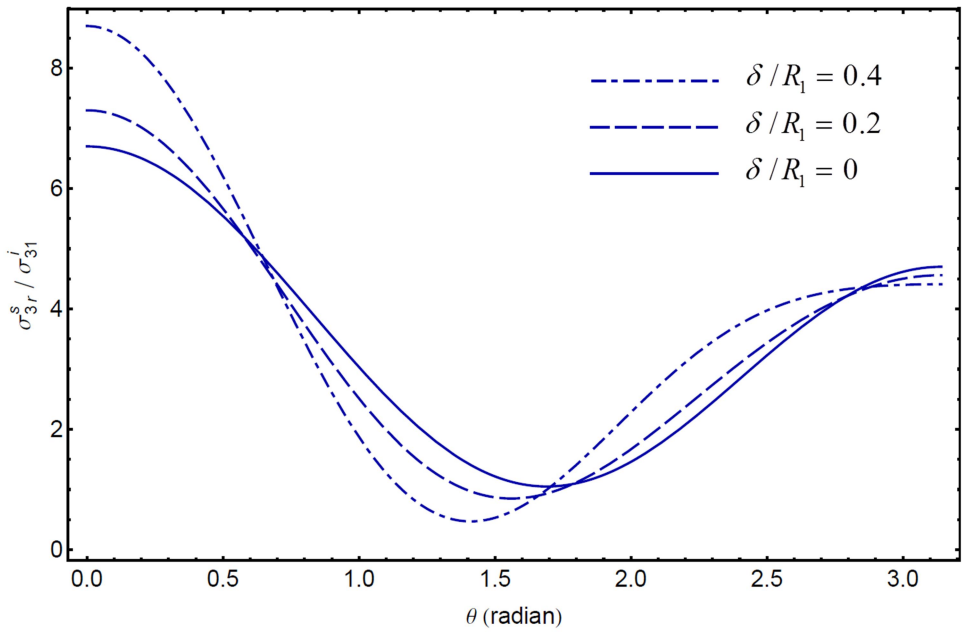

(b)

Fig. 3.9. Variations of (a) $\sigma^s_{3\theta}/\sigma^i_{31}$ and (b) $\sigma^s_{3r}/\sigma^i_{31}$ along fiber-coating interface just inside the fiber, for different eccentricities, δ/R_1. Results pertain to a BTO fiber with CFO coating in an Epoxy matrix.

3.3.5. Scattered interface stresses in a CFO fiber with BTO coating embedded in an Epoxy matrix

In this example, the fiber, coating and matrix are made of CFO, BTO and Epoxy, respectively. Two cases of concentric and eccentric coating are considered here; for both cases the radius of the CFO fiber, R_1 is the same, and $R_2/R_1=1.5$ for the radius of BTO coating layer. For different normalized values of coating eccentricity, $\delta/R_1=0$ (concentric), 0.2 and 0.4, we utilize the present micromechanical theory to calculate the scattered fields of a SH-wave induced by the ascribed mutliferroic sensor. For the dimensionless wave number, $\lambda R_1=2$ the distribution of normalized stress components $\sigma^s_{3\theta}/\sigma^i_{31}$ and $\sigma^s_{3r}/\sigma^i_{31}$ along the fiber-coating interface (just inside the fiber) are illustrated in Figs. 3.9(a) and (b), respectively. These figures then demonstrate the effect of the coating eccentricity on the corresponding scattered interface stresses. As it is seen in Fig. 3.9(a), the $\sigma^s_{3\theta}/\sigma^i_{31}=0$ at $\theta=0$ and $\theta=\pi$ for both concentric and eccentric coatings. For the case of concentric coating $\sigma^s_{3\theta}/\sigma^i_{31}$ attains its minimum at $\theta=0.78$ and its maximum at $\theta=2.36$. However, in the case of the coating with non-uniform thickness the maximum and minimum values of $\sigma^s_{3\theta}/\sigma^i_{31}$ shifts a little to left. For instance, for eccentricity of $\delta/R_1=0.4$ the maximum and minimum values of $\sigma^s_{3\theta}/\sigma^i_{31}$ pertains to θ=0.61 and θ=2.12, respectively. Beside, Fig. 3.9(b) shows the absolute maximum value of $\sigma^s_{3r}/\sigma^i_{31}$ along the interface of fiber for all eccentricity scenarios occurs at $\theta=0$, which located on the interface opposite to the one facing the incident wave. Also, in all cases $\sigma^s_{3r}/\sigma^i_{31}$ has a local maximum at $\theta=\pi$. The case of eccentric coating in

comparison to concentric coating leads to a higher and lower values of $\sigma_{3r}^{s}/\sigma_{31}^{i}$ at $\theta=0$ and $\theta=\pi$, respectively. For eccentricities $\delta/R_1=0$ and 0.4 the minimum value of $\sigma_{3r}^{s}/\sigma_{31}^{i}$ occurs at θ=1.68 and 1.43, respectively, indicating that the minimum values of $\sigma_{3r}^{s}/\sigma_{31}^{i}$ shifts to the left with increasing the coating eccentricities.

3.4. Concluding remarks

In this chapter, an analytical methodology (so-called magneto-electro-mechanical DEIM) has been developed for determination of the magneto-electro-elastic fields of an SH-wave scattered by a two-phase multiferroic inhomogeneity embedded in an infinite transversely isotropic piezoelectric or piezomagnetic medium. To put its wide range of applicability in perspective, the present formulation was applied to several descriptive examples with various degrees of complexities. The calculated results revealed the profound influence of magneto-electro-elastic properties of constituent phases, the thickness and eccentricity of coating layer, as well as the frequency of propagating SH-wave on the pertinent scattered fields induced by the multiferroic fiber within a piezoelectric or piezomagnetic medium. We expect that this investigation (i.e. the developed formulation together with the illustrated numerical results) can serve as a useful reference for further development of three-phase multiferroic composites with a durable and reliable performance under dynamics loadings.

Chapter 4.

Overall viscoelastic response of graphene/polymer nanocomposites with imperfect interface

4.1. Overview

As mentioned earlier, the outstanding properties of graphene make it actually the most fascinating choice to enhance the thermal, electrical and mechanical properties of polymers. In this context, we know that there is a great demand in the electrical industry for polymer composites with excellent electrical performance and high mechanical strength. The polymeric materials are insulator which can be made conductive by adding a dilute volume fraction of graphene fillers. The recent achievements in surface functionalization technologies has made it possible to tailor the quality of graphene/matrix interface to meet various desirable specifications (Novoselov et al., 2004; Ramanathan et al., 2008; Kuilla, 2010;Zhang et al., 2012; Yuan et al., 2014; Wan et al., 2014). For instance, as a primary challenge in the manufacturing processes of graphene nanocomposites, it is known that the pristine graphene is not compatible with organic polymers, and usually do not form a homogeneous composite material. The electrochemical modification of graphene surface is then an essential step to address this issue, and obtain a uniform molecular level dispersion of fillers in the polymer matrix (Worsley et al., 2007; Park et al., 2008; Bai et al., 2009; Zhang et al., 2012; Wan et al., 2014). However, it is a noted phenomenon that the interface

condition between graphene inclusions and the host matrix is never perfect. This mainly originates from the high property contrast between the graphene and host polymers. Besides, due to the chemical interactions during the fabrication of nanocomposites a very thin interphase layer often forms between the fillers and surrounding matrix. Even though the interface layer virtually is very thin, it plays a significant role in controlling the physical processes inside the carbonaceous nanocomposites, owning to the high specific area of nano-sized fillers. For example, in the study of electrical properties of nanocomposites the interfacial resistance and capacitance are known to play a critical role (Seidel and Puydupin-Jamin, 2011; Bao et al., 2012; Wang et al., 2014), and in the investigation on their thermal conductivity the interfacial thermal resistance has proven to be a dominant factor (Nan, et al., 2004; Chen et al., 2005; Yavari et al., 2011). In addition, the quality of load transfer at filler-matrix interface is also known to have a profound effect on the effective Young's modulus and yield strength of nanocomposites (Hashemi et al., 2015; Meguid et al., 2010; Barai and Weng, 2011; Pan et al., 2013). In view of all substantial contributions that can be given by the interface, the surface functionalization of graphene fillers and its influence on the effective properties of graphene-based nanocomposite remains a stimulating problem in the design and fabrication process of these materials.

While the benefits of utilizing graphene fillers in a polymer material can be seen in many ways, our main concern here is on the mechanical properties, with special reference to viscoelasticity. Needless to mention that when the graphene fillers are loaded into a polymer the outcome is a viscoelastic nanocomposite, whose time-dependent behavior necessarily should be studied for its durable and reliable performance in many engineering applications,

specifically at high environment temperatures. In retrospect, the viscoelastic behavior of graphene-based nanocomposites recently has received some attentions. Among them, the experimental contributions of Zandiatashbar et al. (2012a, b), Stanier et al. (2014), Tang et al. (2014), King et al. (2015), Wang et al. (2015a) and Wang et al. (2015b) have shed significant insights into the viscoelastic characteristics of graphene/polymer nanocomposites, but none has touched this issue from a theoretical standpoint. Such a shortcoming motivated us to present a theory for the viscoelastic analysis of nanocomposites, which can be regarded as a simple but widely useful alternative to heavy computational simulations and onerous experimental investigations. In particular, by developing an effective medium theory with two different interface models we intend to uncover how the interface condition affects the overall creep, stress relaxation and strain-rate sensitivity of nanocomposites as the volume fraction and aspect ratio of graphene fillers increase. It is notable in passing that the quality of interfacial interactions between the graphene fillers and polymer matrix plays a crucial role for determining the final creep and recovery performance of graphene/polymer nanocomposites. In fact, the vast interfacial area created by well-dispersed graphene fillers can influence the behavior of surrounding polymer matrix even at a very low content, leading to the formation of a co-continuous network of greatly altered polymer chains. In this light, some factors such as the tailored surface chemistry, high specific area and corrugated feature of graphene fillers can favorably improve the interfacial adhesion, restrict the segmental movement of polymer chains, and eventually alter the viscoelastic characteristics of nanocomposite. Otherwise, the polymer molecules can easily slide along the weak interfaces. This interfacial sliding hiders the load transfer from matrix to inclusions, and substantially

brings down the extent of beneficial impact that can be made by graphene fillers. In the context of viscoelastic response of graphene/polymer nanocomposite, condition of interface then has a profound influence on the effectiveness of graphene reinforcement.

In this chapter, we aim to develop a homogenization theory that can embody the most essential features of a graphene nanocomposite, i.e. volume concentration of fillers, randomness of their orientations, the elastic anisotropy of graphene fillers under the assumed condition of homogenous dispersion, and the relevant parameters of imperfect interface. To this end, we essentially adopt the correspondence principle as the backbone of our formulation, in a way that some known schemes and mathematical formulations for the treatment of elastic composites can be utilized here to disclose the time-dependent viscoelastic behavior of graphene nanocomposites. It is remarkable that, in retrospect, the correspondence principle has been proved as the most convenient rout for the theoretical analysis of viscoelastic composites under various loading conditions (Hashin, 1965; Fisher and Brinson, 2001; Li and Weng, 2013). In this light, we call upon the Mori-Tanaka scheme for a two-phase composite with random microstructure in order to obtain the effective viscoelastic properties of the graphene nanocomposites with perfect interface. As a result, the closed form expressions for the overall bulk and shear moduli of graphene/polymer nanocomposite are obtained in the transformed Laplace domain. Afterwards, we will adopt two different approaches in order to include the interface effect in our homogenization theory. At the end, through consideration of different sets of experimental data, we apply the proposed scheme to uncover the interface effect on the time-dependent creep, stress relaxation and strain-rate sensitivity of graphene/polymer nanocomposites.

4.2. The theory

4.2.1. Constitutive equations of constituent phases

Consider a two-phase nanocomposite with a polymer matrix and 3-D randomly oriented graphene inclusions, carrying the volume concentrations of c_0 and c_1, respectively ($c_0 + c_1 = 1$). The microgeometry of the composite system is schematically shown in Fig. 4.1. The polymer matrix is assumed to be an isotropic material with the time-dependent viscoelastic behavior. In order to make the necessary connection with available literature, and for the sake of comparison with experimental data of Wang et al. (2015a) and Wang et al. (2015b) we suppose that the mechanical behavior of pure polymer matrix can be represented by the 4-parameter Burgers model.

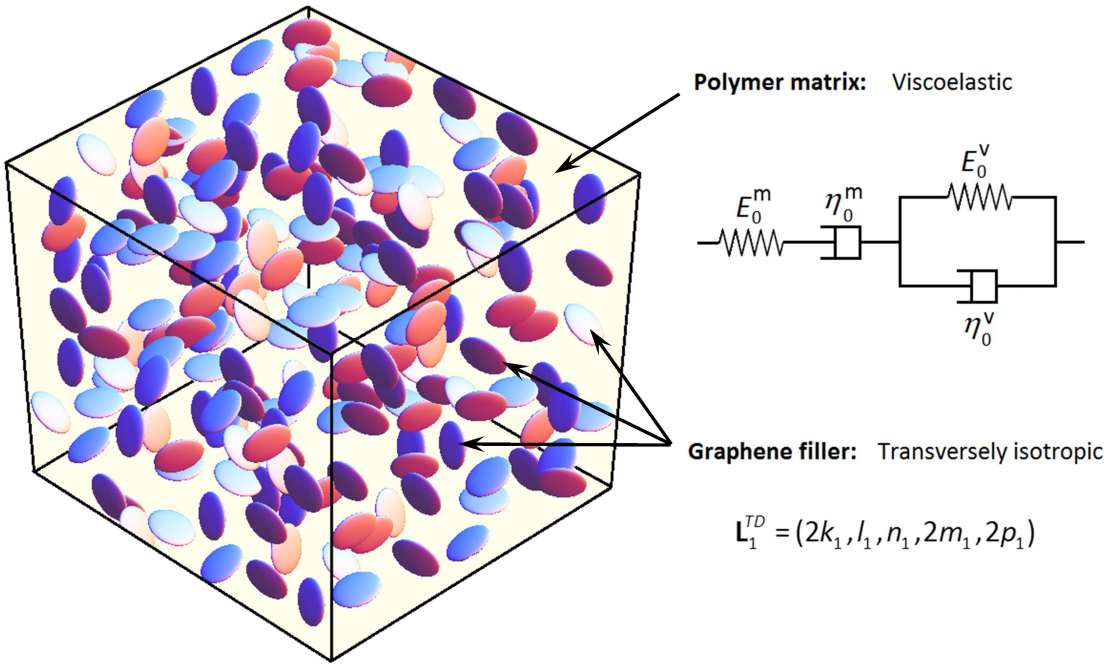

Fig. 4.1. A schematic diagram of viscoelastic graphene/polymer nanocomposite. Polymer is modeled by a Burgers rheological model with four parameters, and graphene fillers are treated as transversely isotropic material with five independent elastic constants.

In this way, the Burgers parameters reported in previous studies can be used as the input parameters of the present micromechanical formulation. This rheological model has the following one-dimensional governing differential equation:

$$\sigma_{11}+\left(\frac{\eta_0^M}{E_0^M}+\frac{\eta_0^V}{E_0^V}+\frac{\eta_0^M}{E_0^V}\right)\dot{\sigma}_{11}+\left(\frac{\eta_0^M\eta_0^V}{E_0^M E_0^V}\right)\ddot{\sigma}_{11}=\eta_0^M\dot{\varepsilon}_{11}+\left(\frac{\eta_0^M\eta_0^V}{E_0^V}\right)\ddot{\varepsilon}_{11}, \tag{4.1}$$

where E_0^M, η_0^M, E_0^V and η_0^V are associated with the Maxwell and Voigt spring and dashpot models. These material parameters can be directly identified from the tensile creep test on the corresponding polymer matrix. As mentioned earlier, for the study of creep, stress relaxation and strain-rate sensitivity of nanocomposite material, we conveniently call upon the correspondence principle in the Laplace transformed domain. In this way, we carry the Laplace transform into the viscoelastic constitutive equation of polymer matrix, Eq. (4.1), to obtain its stress-strain relation in the transformed domain (TD). Accordingly, it is straightforward to show that the transformed Young's modulus of viscoelastic matrix can be written as:

$$E_0^{TD}=\frac{E_0^M\eta_0^V(E_0^V+\eta_0^V s)s}{E_0^M E_0^V+\left[E_0^V\eta_0^M+E_0^M\left(\eta_0^M+\eta_0^V\right)\right]s+\eta_0^M\eta_0^V s^2}. \tag{4.2}$$

In addition, the Poisson's ratio of polymer matrix has been assumed to remain unchanged in the course of deformation, i.e. $\nu_0^{TD}=\nu_0$ (one may assume that $\kappa_0^{TD}=\kappa_0$ for the transformed bulk modulus of matrix, but as the viscoelastic behavior of most polymers are known to be pressure dependent, this does not seem to be a good assumption). Other moduli of matrix in the transformed domain, such as its bulk and shear moduli, then follow from the isotropic

connections, such that $\kappa_0^{TD} = E_0^{TD} / 3(1-2\nu_0^{TD})$ and $\mu_0^{TD} = E_0^{TD} / 2(1+\nu_0^{TD})$. At the end, the constitutive equation of polymer matrix in the transformed domain can be written as:

$$\hat{\boldsymbol{\sigma}}^{(0)}(s) = \mathbf{L}_0^{TD}\, \hat{\boldsymbol{\varepsilon}}^{(0)}(s), \quad \text{where} \quad \mathbf{L}_0^{TD} = (3\kappa_0^{TD}, 2\mu_0^{TD}). \tag{4.3}$$

where $\hat{\boldsymbol{\sigma}}^{(0)}$ and $\hat{\boldsymbol{\varepsilon}}^{(0)}$ are Laplace transform of stress and strain tensors in polymer matrix, as

$$\hat{f}(s) = \int_0^{\infty} f(t)\,.\, e^{-st} dt, \tag{4.4}$$

and $\mathbf{L}_0^{TD}$ is the transformed moduli tensor, expressed in terms of corresponding bulk and shear moduli. The explicit form of Eq. (4.3) can be written in terms of the hydrostatic and deviatoric parts, respectively, as:

$$\hat{\sigma}_{kk}^{(0)}(s) = 3\kappa_0^{TD}(s)\ \ \hat{\varepsilon}_{kk}^{(0)}(s),$$

$$\hat{\sigma}_{kk}'^{(0)}(s) = 2\mu_0^{TD}(s)\ \ \hat{\varepsilon}_{kk}'^{(0)}(s). \tag{4.5}$$

In present analysis, the reinforcing fillers have been supposed to possess common spheroidal shapes with almost same dimensions, as shown in Fig. 4.1. It is noted that the graphene fillers in the composite are somewhat in the wrinkled and curved configurations. Since relating the complex geometrical details of such a disordered reinforcement to the overall behavior of the nanocomposite is not straightforward, some priori assumptions have to be made here. In this light, to present our theory in a simple and analytical form the graphene fillers have been necessarily idealized as thin oblate inclusions under an assumed condition of homogenous dispersion in the corresponding matrix. Compared to the graphene fillers, a disk-like inclusion possesses almost the same shape when its thickness-to-diameter ratio is sufficiently

small, as is usually the case. In addition, we suppose that the graphene fillers are virtually defect-free, and their mechanical response can be considered as predominantly elastic. In fact, the hexagonal distribution of carbon atoms on the graphene surface renders its in-plane property isotropic; however, the stiffness of graphene in normal-to-plane direction is substantially lower than its in-plane one (Lee et al., 2008; Michel and Verberck, 2008; Cadelano et al., 2010; Scarpa et al., 2010; Bera et al., 2010; Gao and Huang, 2014). In view of that, both GNS and GNP can be treated as transversely isotropic materials. Following the Hill's notation for the constitutive equation of a transversely isotropic material, the moduli tensor for reinforcing fillers can be written in terms of five independent constants (Hill, 1964):

$$\mathbf{L}_1 = (2k_1, l_1, n_1, 2m_1, 2p_1), \tag{4.6}$$

where k_1, l_1, n_1, m_1 and p_1 are the plane-strain bulk modulus, cross modulus, through-the-thickness modulus, in-plane shear modulus and transverse shear modulus, respectively. In terms of the common engineering constants with direction 1 symmetric and plane 2-3 isotropic, Eq. (4.6) can alternatively be recast into $\mathbf{L}_1 = (2\kappa_{23}, C_{12}, C_{11}, 2\mu_{23}, 2\mu_{12})$. The through-the-thickness Young's modulus and transverse Poisson's ratio also are given by $E_{11} = n_1 - l_1^2 / k_1$ and $\nu_{12} = l_1 / 2k_1$. To make use of correspondence principle, we now write the constitutive equation of inclusions in the transformed domain, as:

$$\hat{\boldsymbol{\sigma}}^{(1)}(s) = \mathbf{L}_1^{TD}\, \hat{\boldsymbol{\varepsilon}}^{(1)}(s), \quad \text{where} \quad \mathbf{L}_1^{TD} = (2k_1, l_1, n_1, 2m_1, 2p_1), \tag{4.7}$$

where $\hat{\boldsymbol{\sigma}}^{(1)}$ and $\hat{\boldsymbol{\varepsilon}}^{(1)}$ are the Laplace transform of associated stress and strain tensors in phase 1. This stress-strain relation in graphene fillers then carries the following explicit form:

$$\begin{aligned}&(\hat{\sigma}_{22}+\hat{\sigma}_{33})=2k_1(\hat{\varepsilon}_{22}+\hat{\varepsilon}_{33})+2l_1\hat{\varepsilon}_{11},\quad \hat{\sigma}_{11}=l_1(\hat{\varepsilon}_{22}+\hat{\varepsilon}_{33})+n_1\hat{\varepsilon}_{11},\\&(\hat{\sigma}_{22}-\hat{\sigma}_{33})=2m(\hat{\varepsilon}_{22}-\hat{\varepsilon}_{33}),\quad \hat{\sigma}_{23}=2m_1\hat{\varepsilon}_{23},\quad \hat{\sigma}_{12}=2p_1\hat{\varepsilon}_{12}.\end{aligned} \tag{4.8}$$

The advantage of invoking such a notation is that Walpole's scheme (1969, 1981) for the manipulation of transversely isotropic tensors, such as inner product and inverse, can be called upon to obtain the explicit results for the effective properties of graphene/polymer nanocomposite.

4.2.2. Effective properties of graphene nanocomposite with perfect interface

Let the overall stress-strain relation of nanocomposite be written as:

$$\hat{\bar{\boldsymbol{\sigma}}}(s)=\bar{\mathbf{L}}^{TD}\,\hat{\bar{\boldsymbol{\varepsilon}}}(s), \tag{4.9}$$

where $\bar{\mathbf{L}}^{TD}$ is the effective moduli tensor in the transformed domain. In view of the random microstructure of nanocomposite, the effective medium can be envisioned to be isotropic, such that:

$$\bar{\mathbf{L}}^{TD}=(3\bar{\kappa}^{TD},2\bar{\mu}^{TD}), \tag{4.10}$$

where $\bar{\kappa}^{TD}$ and $\bar{\mu}^{TD}$ represents the effective bulk and shear moduli of nanocomposite, respectively. According to correspondence principle, the overall viscoelastic moduli of our

nanocomposite with perfect interface can be determined by calling upon the Mori-Tanaka method for a heterogeneous medium with random microstructure, as:

$$\bar{\mathbf{L}}^{TD}=\left(c_1\left\langle \mathbf{L}_1^{TD}\mathbf{A}^{TD}\right\rangle+c_0\mathbf{L}_0^{TD}\right)\left(c_1\left\langle \mathbf{A}^{TD}\right\rangle+c_0\mathbf{I}\right)^{-1},\ \text{with}\ \ \mathbf{A}^{TD}=\left[\mathbf{I}+\mathbf{S}\,\mathbf{L}_0^{TD\,-1}\left(\mathbf{L}_1^{TD}-\mathbf{L}_0^{TD}\right)\right]^{-1}. \tag{4.11}$$

In this formula, $\langle\cdot\rangle$ represents the orientational average of the said quantity, $\mathbf{I}$ is the fourth-rank identity tensor, and $\mathbf{S}$ is the Eshelby's tensor, evaluated with the Poisson's ratio of matrix, ν_0^{TD}, and the aspect ratio of spheroidal inclusions, α. Noteworthy to mention that several micromechanical theories could be invoked here, but in order to keep the results explicit we adopted the Mori–Tanaka approach developed by Weng (1984, 1990), Qiu and Weng (1990) and Benveniste (1987). This model provides sufficiently accurate estimates when the inclusion concentration is not particularly high, as it is usually the case for graphene nanocomposites. Now, upon substitution of $\mathbf{L}_1^{TD}$ and $\mathbf{L}_0^{TD}$ from Eqs. (4.3) and (4.7) into Eq. (4.11), effective bulk and shear moduli of viscoelastic nanocomposite can be explicitly calculated in the transformed domain, as:

$$\bar{\kappa}^{TD}=\frac{c_0\kappa_0^{TD}+c_1\xi_{\mathrm{I}}^{TD}}{c_0+3c_1\xi_{\mathrm{II}}^{TD}},\qquad \bar{\mu}^{TD}=\frac{c_0\mu_0^{TD}+c_1\zeta_{\mathrm{I}}^{TD}}{c_0+2c_1\zeta_{\mathrm{II}}^{TD}}, \tag{4.12}$$

in which

$$\begin{aligned}
\xi_{\mathrm{I}}^{TD}&=\left[4\left(k_1d-l_1g\right)+2\left(l_1d-n_1g+l_1b-2k_1h\right)+\left(n_1b-2l_1h\right)\right]/9\left(bd-2gh\right),\\
\xi_{\mathrm{II}}^{TD}&=\left[2d-2\left(g+h\right)+b\right]/9\left(bd-2gh\right),\\
\zeta_{\mathrm{I}}^{TD}&=\left[\left(k_1d-l_1g\right)-\left(l_1d-n_1g+l_1b-2k_1h\right)+\left(n_1b-2l_1h\right)\right]/15\left(bd-2gh\right)\\
&\quad+2m/5e+2p/5f,\\
\zeta_{\mathrm{II}}^{TD}&=\left[d+2\left(g-h\right)+2b\right]/30\left(bd-2gh\right)+1/5e+1/5f.
\end{aligned} \tag{4.13}$$

Constants $b,\ d,\ e,\ f,\ g$ and h are transversely isotropic parameters that appear in Walpole's scheme for the manipulation of transversely isotropic tensors, as summarized in Qiu and Weng (1990). These six parameters depend on the transformed moduli of matrix (i.e. κ_0^{TD} and μ_0^{TD}), five elastic constants of fillers (i.e. k_1, l_1, n_1, m_1 and p_1), and Eshelby's **S**-tensor of the oblate inclusions with direction-1 as their symmetric axis, such that:

$$
\begin{aligned}
b &= 1+2\left(k_1-k_0^{TD}\right)\left[(1-\nu_0)(S_{2222}+S_{2233})-2\nu_0 S_{2211}\right]/E_0^{TD} \\
&\quad +2\left(l_1-l_0^{TD}\right)\left[(1-\nu_0)S_{1122}-\nu_0 S_{1111}\right]/E_0^{TD}, \\
d &= 1+\left\{\left(n_1-n_0^{TD}\right)\left[S_{1111}-2\nu_0 S_{1122}\right]+2\left(l_1-l_0^{TD}\right)\left[(1-\nu_0)S_{1122}-\nu_0 S_{1111}\right]\right\}/E_0^{TD}, \\
e &= 1+2\left(m_1-m_0^{TD}\right)S_{2323}/m_0^{TD}, \\
f &= 1+2\left(p_1-p_0^{TD}\right)S_{1212}/p_0^{TD}, \\
g &= \left\{2\left(k_1-k_0^{TD}\right)\left[(1-\nu_0)S_{1122}-\nu_0 S_{1111}\right]+\left(l_1-l_0^{TD}\right)\left[S_{1111}-2\nu_0 S_{1122}\right]\right\}/E_0^{TD}, \\
h &= \left(n_1-n_0^{TD}\right)\left[S_{2211}-\nu_0(S_{2222}+S_{2233})\right]/E_0^{TD} \\
&\quad +\left(l_1-l_0^{TD}\right)\left[(1-\nu_0)(S_{2222}+S_{2233})-2\nu_0 S_{2211}\right]/E_0^{TD},
\end{aligned}
\tag{4.14}
$$

where $k_0^{TD}, l_0^{TD},\ n_0^{TD},\ m_0^{TD}$ and p_0^{TD} are the counterparts of k_1, l_1, n_1, m_1 and p_1 for the viscoelastic isotropic matrix, given by $k_0^{TD}=\kappa_0^{TD}+\mu_0^{TD}/3,\quad l_0^{TD}=\kappa_0^{TD}-2\mu_0^{TD}/3,$ $n_0^{TD}=\kappa_0^{TD}+4\mu_0^{TD}/3$ and $m_0^{TD}=p_0^{TD}=\mu_0^{TD}$.

The fundamental viscoelastic characteristics of graphene nanocomposites can be readily examined once the expressions for $\bar{\kappa}^{TD}$ and $\bar{\mu}^{TD}$ are known from expressions (4.12). For the study of time-dependent creep under constant stress, $\bar{\sigma}_{11}=constant$, the overall strain in the transformed domain can be expressed as $\hat{\bar{\varepsilon}}_{11}=\bar{\sigma}_{11}/s\,\bar{E}^{TD}(s)$, in which $\bar{E}^{TD}=9\bar{\kappa}^{TD}\bar{\mu}^{TD}/(3\bar{\kappa}^{TD}+\bar{\mu}^{TD})$. The time-dependent strain then can be obtained from the standard Laplace inversion, as:

$$\bar{\varepsilon}_{11}(t)=\frac{1}{2\pi i}\int_{\delta-i\infty}^{\delta+i\infty}\frac{\hat{\bar{\sigma}}_{11}(s)}{\bar{E}^{TD}(s)}e^{st}\,ds=\frac{\bar{\sigma}_{11}}{2\pi i}\int_{\delta-i\infty}^{\delta+i\infty}\frac{1}{s\,\bar{E}^{TD}(s)}e^{st}ds, \tag{4.15}$$

where δ is a positive and i is the imaginary number. Likewise, under a constant applied strain, $\bar{\varepsilon}_{11}=constant$, the stress relaxation follows from:

$$\bar{\sigma}_{11}(t)=\frac{1}{2\pi i}\int_{\delta-i\infty}^{\delta+i\infty}\bar{E}^{TD}(s)\hat{\bar{\varepsilon}}_{11}(s)e^{st}\,ds=\frac{\bar{\varepsilon}_{11}}{2\pi i}\int_{\delta-i\infty}^{\delta+i\infty}\frac{\bar{E}^{TD}(s)}{s}e^{st}ds. \tag{4.16}$$

In the same fashion, for the study of strain-rate sensitivity we suppose that nanocomposite is under a constant strain rate, $\dot{\bar{\varepsilon}}_{11}=constant.$ Accordingly, the evolution of flow stress can be obtained from:

$$\bar{\sigma}_{11}(t)=\frac{\dot{\bar{\varepsilon}}_{11}}{2\pi i}\int_{\delta-i\infty}^{\delta+i\infty}\frac{\bar{E}^{TD}(s)}{s^{2}}e^{st}ds. \tag{4.17}$$

This completes the formulation for determining the overall time-dependent behavior of graphene nanocomposite with perfect interface.

4.2.3. The interface effects

We now consider the interface effect on the effective viscoelastic properties of graphene nanocomposites. Eq. (4.12) was derived based on the assumption of perfect interface; but in reality, the interface condition is never perfect. In this light, the interface contribution in the overall time-dependent behavior of nanocomposite is inevitable. It will be shown later that the consideration of interface effect gives the best prediction for the experimental data. To

address the issue of interface effect in the context of homogenization theory presented in Section 4.2.2 we call upon two different interface models, as follow.

4.2.3.1. Model 1: Weakened interphase layer with a diminishing thickness introduced between graphene fillers and polymer

In this section, the interface effect will be modeled by the introduction of a diminishing layer of interphase between the graphene fillers and surrounding matrix. It is noteworthy that, in retrospect, similar approach has been adopted previously by some notable contributions for treatment of imperfect interface in various composite materials. Among others, we mention in particular the investigation of Wang et al. (2014) for determining the electrical properties of graphene and CNT nanocomposites, and the contribution made by Wang et al. (2015*c*) for the study on magnetoelectric coupling in multiferroic composites with imperfect interface. According to this methodology, we first consider the existence of a spheroidal layer of interphase by adding a thickness t to the semi-axis of original inclusion. Interphase is then taken to surround the inclusion, making it similar to a "thinly coated" graphene filler. In other words, this thin layer and the core particle are taken to form an inclusion system, in which the volume concentration of the interface is denoted as c_{int}, and that of the inclusion as (1- c_{int}). Compared to dimensions of original inclusion, coating thickness is taken to be diminishingly small; we now intend to make it zero to turn the interphase into an interface. (1-c_{int}) is the volume fraction of the original graphene in the "coated" graphene, given by $1-c_{\text{int}} = DR^2 / \left[\left(D+2t \right) \left(R+t \right)^2 \right]$, where D and R are the thickness and radius of thin oblate inclusions, respectively. Now, by taking $t << D$, it is straightforward to show that:

$$c_{\text{int}} = 2\left(1+2\alpha\right) t/D, \tag{4.18}$$

where $\alpha = D/2R$ denotes the aspect ratio of graphene fillers. The interphase layer is further assumed to be viscoelastic with stiffness tensor of $\mathbf{L}_{\text{int}}^{TD}$ in transformed domain. In this light, we suppose that the viscoelastic behavior of interface layer can be described by a Voight rheological model, such that its constitutive equation under tension can be represented by:

$$\hat{\sigma}_{11}(s) = E_{\text{int}}^{TD}\,\hat{\varepsilon}_{11}(s), \quad \text{where} \quad E_{\text{int}}^{TD} = E_{\text{int}}^{V} + \eta_{\text{int}}^{V}\, s. \tag{4.19}$$

In this formula, E_{int}^{V} and η_{int}^{V} are unknown interfacial constants which are associated with the Voight spring and dashpot model. As it will be demonstrated later in the numerical studies, due to the imperfect interface the interfacial stiffness are usually much lower than the intrinsic stiffness of core graphene filler. Besides, the Poisson's ratio of interface layer is also assumed to remain unchanged, and be equal to that of matrix, $\nu_{\text{int}}^{TD} = \nu_0$. In this light, the transformed moduli of interface layer then can be recast into $\mathbf{L}_{\text{int}}^{TD} = (3\kappa_{\text{int}}^{TD},\, 2\mu_{\text{int}}^{TD})$, in which $\kappa_{\text{int}}^{TD} = E_{\text{int}}^{TD}/3(1-2\nu_{\text{int}}^{TD})$ and $\mu_{\text{int}}^{TD} = E_{\text{int}}^{TD}/2(1+\nu_{\text{int}}^{TD})$. Now, the effective viscoelastic property of inclusion system, denoted by $\bar{\mathbf{L}}_{\text{coat}}^{TD}$, can be obtained by using the Mori-Tanaka method for a composite with aligned fillers (Weng, 1984 & 1990):

$$\mathbf{L}_{\text{coat}}^{TD} = \mathbf{L}_{\text{int}}^{TD} + (1-c_{\text{int}})\left(\mathbf{L}_{1}^{TD} - \mathbf{L}_{\text{int}}^{TD}\right)\left[\mathbf{I} + c_{\text{int}}\,\mathbf{S}_{\text{int}}\,\mathbf{L}_{\text{int}}^{TD\,-1}\left(\mathbf{L}_{1}^{TD} - \mathbf{L}_{\text{int}}^{TD}\right)\right]^{-1}, \tag{4.20}$$

where $\mathbf{S}_{\text{int}}$ means that the Eshelby's tensor is evaluated with the property of the interface; however, in the limiting case of diminishing thickness for the interface layer, the "thinly coated" inclusion and original inclusion share the same shape and the same $\mathbf{S}$-tensor, $\mathbf{S}_{\text{int}} = \mathbf{S}$,

since the Eshelby's tensor depends only on the interface Poisson's ratio and the shape of core inclusion. Finally, upon substitution of $\mathbf{L}_1^{TD}$, $\mathbf{L}_{\text{int}}^{TD}$ and $\mathbf{S}_{\text{int}}^{TD}$ into Eq. (4.20), the explicit expressions for the overall viscoelastic moduli of inclusion system, $\mathbf{L}_{coat}^{TD} = (2k_{coat}^{TD}, l_{coat}^{TD}, n_{coat}^{TD}, 2m_{coat}^{TD}, 2p_{coat}^{TD})$, can be determined. Accordingly, five effective constants of the particle ensemble (i.e. graphene filler and its thin coating) are obtained to be:

$$k_{coat}^{TD} = \left\{ \left[c_{\text{int}} k_{\text{int}}^{TD} \left(\tilde{b}\tilde{d} - 2\tilde{g}\tilde{h} \right) + \left(1 - c_{\text{int}}\right) \left(k_1 \tilde{d} - l_1 \tilde{g} \right) \right] \left[c_{\text{int}} \left(\tilde{b}\tilde{d} - 2\tilde{g}\tilde{h} \right) + \left(1 - c_{\text{int}}\right) \tilde{b} \right] \right.$$
$$\left. + \left(1 - c_{\text{int}}\right) \tilde{g} \left[c_{\text{int}} l_{\text{int}}^{TD} \left(\tilde{b}\tilde{d} - 2\tilde{g}\tilde{h} \right) + \left(1 - c_{\text{int}}\right) \left(l_1 \tilde{b} - 2k_1 \tilde{h} \right) \right] \right\} / \lambda,$$

$$l_{coat}^{TD} = \left\{ \left[c_{\text{int}} l_{\text{int}}^{TD} \left(\tilde{b}\tilde{d} - 2\tilde{g}\tilde{h} \right) + \left(1 - c_{\text{int}}\right) \left(l_1 \tilde{d} - n_1 \tilde{g} \right) \right] \left[c_{\text{int}} \left(\tilde{b}\tilde{d} - 2\tilde{g}\tilde{h} \right) + \left(1 - c_{\text{int}}\right) \tilde{b} \right] \right.$$
$$\left. + \left(1 - c_{\text{int}}\right) \tilde{g} \left[c_{\text{int}} n_{\text{int}}^{TD} \left(\tilde{b}\tilde{d} - 2\tilde{g}\tilde{h} \right) + \left(1 - c_{\text{int}}\right) \left(n_1 \tilde{b} - 2l_1 \tilde{h} \right) \right] \right\} / \lambda,$$

$$n_{coat}^{TD} = \left\{ \left[c_{\text{int}} n_{\text{int}}^{TD} \left(\tilde{b}\tilde{d} - 2\tilde{g}\tilde{h} \right) + \left(1 - c_{\text{int}}\right) \left(n_1 \tilde{b} - 2l_1 \tilde{h} \right) \right] \left[c_{\text{int}} \left(\tilde{b}\tilde{d} - 2\tilde{g}\tilde{h} \right) + \left(1 - c_{\text{int}}\right) \tilde{d} \right] \right.$$
$$\left. + 2\left(1 - c_{\text{int}}\right) \tilde{h} \left[c_{\text{int}} l_{\text{int}}^{TD} \left(\tilde{b}\tilde{d} - 2\tilde{g}\tilde{h} \right) + \left(1 - c_{\text{int}}\right) \left(l_1 \tilde{d} - n_1 \tilde{g} \right) \right] \right\} / \lambda,$$

$$m_{coat}^{TD} = \left[c_{\text{int}} m_{\text{int}}^{TD} \tilde{e} + \left(1 - c_{\text{int}}\right) m_1 \right] / \left(c_{\text{int}} \tilde{e} + \left(1 - c_{\text{int}}\right) \right),$$

$$p_{coat}^{TD} = \left[c_{\text{int}} p_{\text{int}}^{TD} \tilde{f} + \left(1 - c_{\text{int}}\right) p_1 \right] / \left(c_{\text{int}} \tilde{f} + \left(1 - c_{\text{int}}\right) \right), \tag{4.21}$$

in which $\lambda = \left[c_{\text{int}} \left(\tilde{b}\tilde{d} - 2\tilde{g}\tilde{h} \right) + \left(1 - c_{\text{int}}\right) \tilde{d} \right] \left[c_{\text{int}} \left(\tilde{b}\tilde{d} - 2\tilde{g}\tilde{h} \right) + \left(1 - c_{\text{int}}\right) \tilde{b} \right] - 2\left(1 - c_{\text{int}}\right)^2 \tilde{g}\tilde{h}.$ In this formula, $\tilde{b}$, $\tilde{d}$, $\tilde{e}$, $\tilde{f}$, $\tilde{g}$ and $\tilde{h}$ are six transversely isotropic parameters that appear in Walpole's notations, given by:

$$\tilde{b}=1+2\left(k_1-k_{\text{int}}^{TD}\right)\left[(1-\nu_0)(S_{2222}+S_{2233})-2\nu_0 S_{2211}\right]/E_{\text{int}}^{TD}$$
$$+\left(l_1-l_{\text{int}}^{TD}\right)\left[(1-\nu_0)S_{1122}-\nu_0 S_{1111}\right]/E_{\text{int}}^{TD},$$
$$\tilde{d}=1+\left\{\left(n_1-n_{\text{int}}^{TD}\right)\left[S_{1111}-2\nu_0 S_{1122}\right]+2\left(l_1-l_{\text{int}}^{TD}\right)\left[(1-\nu_0)S_{1122}-\nu_0 S_{1111}\right]\right\}/E_{\text{int}}^{TD},$$
$$\tilde{e}=1+2\left(m_1-m_{\text{int}}^{TD}\right)S_{2211}/m_{\text{int}}^{TD},$$
$$\tilde{f}=1+2\left(p_1-p_{\text{int}}^{TD}\right)S_{1212}/p_{\text{int}}^{TD},$$
$$\tilde{g}=\left\{2\left(k_1-k_{\text{int}}^{TD}\right)\left[(1-\nu_0)S_{1122}-\nu_0 S_{1111}\right]+\left(l_1-l_{\text{int}}^{TD}\right)\left[S_{1111}-2\nu_0 S_{1122}\right]\right\}/E_{\text{int}}^{TD},$$
$$\tilde{h}=\left(n_1-n_{\text{int}}^{TD}\right)\left[S_{2211}-\nu_0(S_{2222}+S_{2233})\right]/E_{\text{int}}^{TD}$$
$$+\left(l_1-l_{\text{int}}^{TD}\right)\left[(1-\nu_0)(S_{2222}+S_{2233})-2\nu_0 S_{2211}\right]/E_{\text{int}}^{TD}. \tag{4.22}$$

where constants $k_{\text{int}}^{TD}=\kappa_{\text{int}}^{TD}+\mu_{\text{int}}^{TD}/3$, $l_{\text{int}}^{TD}=\kappa_{\text{int}}^{TD}-2\mu_{\text{int}}^{TD}/3$, $n_{\text{int}}^{TD}=\kappa_{\text{int}}^{TD}+4\mu_{\text{int}}^{TD}/3$ and $m_{\text{int}}^{TD}=p_{\text{int}}^{TD}=\mu_{\text{int}}^{TD}$ stand for the viscoelastic interface.

For the study of interface effect, the inclusion system is then embedded into the original polymer matrix to determine the effective viscoelastic properties of corresponding nanocomposite, again by Eq. (4.12). In doing so, material parameters k_1, l_1, n_1, m_1 and p_1 in expressions (4.12), (4.13) and (4.14) should be replaced by the counterpart effective constants of thinly-coated inclusion system, i.e. k_{coat}^{TD}, l_{coat}^{TD}, n_{coat}^{TD}, m_{coat}^{TD} and p_{coat}^{TD} given by Eq. (4.21). In this way, the overall bulk and shear moduli, $\bar{\kappa}^{TD}$ and $\bar{\mu}^{TD}$, for the graphene/polymer nanocomposite with a weakened interface condition can be calculated. This completes our first methodology (referred to as model 1) for the theoretical treatment of imperfect interface.

4.2.3.2. Model 2: Displacement jump at graphene-polymer interface, characterized by sliding parameter γ

In formulation of Section 4.2.2, no discontinuity between the graphene filler and adjacent matrix in terms of corresponding traction or displacement has been considered. In reality, however, such a perfect continuity in displacement at the graphene-polymer interface cannot be assured. In this light, we now call upon the concept of slightly weakened interfaces Qu (1993a, b) to model the imperfect interface condition in graphene/polymer nanocomposites. According to this methodology, the traction continuity will be maintained,

$$\Delta\sigma_{ij} n_j = \left[\sigma_{ij}(\boldsymbol{x})\right] n_j = 0, \tag{4.23}$$

but, the displacement jump will be taken to follow the linear spring layer model proposed by Benveniste (1985), Hashin (1990) and Qu (1993a, b), as

$$\Delta u_i = \left[u_i(\boldsymbol{x})\right] = \lambda_{ij}\, \sigma_{jk}\, n_k, \tag{4.24}$$

Here, $[\cdot]$ represent the jump of the said quantity at the interface with an outward normal, n_i, from graphene filler to the matrix, and λ_{ij} represents the compliance of interface layer. A particularly useful form of this interface parameter is

$$\lambda_{ij} = \gamma\, \delta_{ij} + (\beta - \gamma)\, n_i\, n_j. \tag{4.25}$$

When β =0, the interface is allowed to slide but not to have normal separation or interpenetration, as it is usually the case in graphene/polymer nanocomposites. This condition will be assumed in present methodology. Our concern then will be the influence of sliding

parameter γ on the overall viscoelastic response of nanocomposite. It is evident that, when $\gamma \to 0,$ it becomes a perfectly bonded interface, and when $\gamma \to \infty$ the interface is totally unbonded. According to present scheme for treatment of imperfect interface condition, the Eshelby's **S**-tensor in Eq. (4.11) should be modified to $\mathbf{S}^m,$ to account for the effect of interface sliding parameter, γ, as:

$$\mathbf{S}^m = \mathbf{S} + \left(\mathbf{I} - \mathbf{S}\right)\mathbf{H}\,\mathbf{L}_0^{TD}\left(\mathbf{I} - \mathbf{S}\right), \tag{4.26}$$

with $\mathbf{H} = \gamma\left(\mathbf{P} - \mathbf{Q}\right).$ This relation for modified Eshelby's tensor has been taken from Eq. (2.13) of Qu (1993a), but written in the transformed domain. In Eq. (4.26), $\mathbf{S}$ is the regular Eshelby's tensor, $\mathbf{L}_0^{TD}$ is the transformed stiffness moduli of polymer matrix, **I** is the identity tensor, and **H** represents the imperfection compliance tensor. The formula to derive the expression for the components of the **H**-tensor is provided in Appendix C of Qu (1993a). Considering only the tangential imperfection, γ, and making the normal imperfection zero, β = 0, one can write the imperfection compliance tensor as

$$H_{ijkl} = \gamma\left(P_{ijkl} - Q_{ijkl}\right), \tag{4.27}$$

where

$$\begin{aligned} P_{ijkl} &= \frac{3}{16\pi}\int_0^{\pi}\left[\int_0^{2\pi}\left(\delta_{ik}n_j'n_l' + \delta_{jk}n_i'n_l' + \delta_{il}n_k'n_j' + +\delta_{jl}n_k'n_i'\right)n^{-1}d\theta\right]\sin\phi\, d\phi, \\ Q_{ijkl} &= \frac{3}{4\pi}\int_0^{\pi}\left[\int_0^{2\pi}\left(n_i'n_j'n_l'n_k'\right)n^{-3}d\theta\right]\sin\phi\, d\phi, \end{aligned} \tag{4.28}$$

with $n_i' = \left(\cos\phi,\ \alpha\sin\phi\cos\theta,\ \alpha\sin\phi\sin\theta\right)/D$ and $n = \sqrt{n_i'n_i'}$. Using this formulation, the nanozero components of tensors **P** and **Q** can be obtained to

$$P_{1111}=\frac{3}{2D}\frac{1}{(1-\alpha^2)}\left[1-\frac{\alpha^2}{\sqrt{1-\alpha^2}}\mathrm{Sinh}^{-1}\frac{\sqrt{1-\alpha^2}}{\alpha}\right],$$
$$P_{2222}=\frac{3}{4D}\frac{\alpha^2}{(1-\alpha^2)}\left[\frac{2-\alpha^2}{\sqrt{1-\alpha^2}}\mathrm{Sinh}^{-1}\frac{\sqrt{1-\alpha^2}}{\alpha}-1\right],$$
$$P_{1212}=\frac{3}{8D}\left[\frac{\alpha^2}{\sqrt{1-\alpha^2}}\mathrm{Sinh}^{-1}\frac{\sqrt{1-\alpha^2}}{\alpha}-\frac{2-\alpha^2}{2(1-\alpha^2)}\left(\frac{\alpha^2}{\sqrt{1-\alpha^2}}\mathrm{Sinh}^{-1}\frac{\sqrt{1-\alpha^2}}{\alpha}-1\right)\right],$$
$$P_{3333}=P_{2222},\quad P_{2323}=P_{2222}/2,\quad P_{1313}=P_{1212},\tag{4.29}$$

and

$$Q_{1111}=\frac{3}{2D}\left[\frac{2\alpha^2+1}{(1-\alpha^2)^2}-\frac{3\alpha}{(1-\alpha^2)^{5/2}}\mathrm{Sinh}^{-1}\frac{\sqrt{1-\alpha^2}}{\alpha}\right],$$
$$Q_{2222}=\frac{9}{8D}\left[\alpha^2+\frac{\alpha^4(5-2\alpha^2)}{2(1-\alpha^2)^2}-\frac{\alpha^4(4-\alpha^2)}{2(1-\alpha^2)^{5/2}}\mathrm{Sinh}^{-1}\frac{\sqrt{1-\alpha^2}}{\alpha}\right],$$
$$Q_{1212}=\frac{3}{4D}\left[\frac{\alpha^2(\alpha^2+2)}{(1-\alpha^2)^{5/2}}\mathrm{Sinh}^{-1}\frac{\sqrt{1-\alpha^2}}{\alpha}-\frac{\alpha^2(4-\alpha^2)}{(1-\alpha^2)^2}\right],$$
$$Q_{3333}=Q_{2222},\quad Q_{1212}=Q_{1133}=Q_{1313}=Q_{1122},\quad Q_{1313}=Q_{1212},$$
$$Q_{2233}=Q_{2323}=Q_{2222}/3,\tag{4.30}$$

in which D and α, respectively, are the thickness and aspect ratio of the graphene fillers. Now, the modified Eshelby's tensor $\mathbf{S}^m$ can be substituted into Eq. (4.11). As a result, in parallel to Eq. (4.12) but including the additional contribution from the displacement jump at the interface, the effective bulk and shear moduli of graphene/polymer nanocomposite with an imperfect interface can be obtained as

$$\overline{\kappa}^{TD}=\frac{c_0\kappa_0^{TD}+c_1\xi_{\mathrm{I}}^{TD}}{c_0+3c_1\left(\xi_{\mathrm{II}}^{TD}+\xi_{\mathrm{H}}^{TD}\right)},\qquad \overline{\mu}^{TD}=\frac{c_0\mu_0^{TD}+c_1\zeta_{\mathrm{I}}^{TD}}{c_0+2c_1\left(\zeta_{\mathrm{II}}^{TD}+\zeta_{\mathrm{H}}^{TD}\right)},\tag{4.31}$$

in which the expressions of ξ_{I}^{TD}, ξ_{II}^{TD}, ζ_{I}^{TD} and ζ_{II}^{TD} have been already given in Eq. (4.13). Because of the effect of imperfect interface, contained by tensor **H**, the only extra terms that go into Eq. (4.31) are ξ_{H}^{TD} and ζ_{H}^{TD}. These additional terms, respectively, are the hydrostatic

and deviatoric components of the isotropic tensor $\left\langle \mathbf{H}\,\mathbf{L}_1^{TD}\left[\mathbf{I}+\mathbf{S}^m\,\mathbf{L}_0^{TD^{-1}}\left(\mathbf{L}_1^{TD}-\mathbf{L}_0^{TD}\right)\right]^{-1}\right\rangle$, by which values of ξ_{H}^{TD} and ζ_{H}^{TD} can be readily determined after calling upon the Walpole's mathematical scheme for evaluating the relevant orientational average. The modified $\bar{\kappa}^{TD}$ and $\bar{\mu}^{TD}$ given by Eq. (4.31) can be employed in conjunction with Eqs. (4.15) and (4.17) to predict the creep, relaxation and strain-rate sensitivity of graphene/polymer nanocomposites with weakened interface.

4.3. Numerical results and discussion

In this section, through consideration of some real examples of nanocomposites, we intend to uncover the interface effects on the fundamental viscoelastic characteristics of graphene/polymer composite materials. In this process, the applicability and robustness of the homogenization theory with proposed interface models also will be placed in perspective. Two different sets of experimental data available in the literature will be reconsidered in following sections. Section 4.3.1 is devoted to graphene/Polystyrene nanocomposite that has been tested by Wang et al. (2015a) at different volume concentrations of GNS fillers. Next example, posted in Section 4.3.2, is associated with a nanocomposite for which the graphene fillers with different aspect ratios have been incorporated into a Polylactide matrix. The measured creep data for such a material has been given by Wang et al. (2015b). For more illustration on the microstructure of abovementioned graphene nanocomposites, their microscopic images at some selected filler loadings have been depicted in Fig. 4.2. This

figure shows a sufficiently homogenous dispersion of graphene fillers in the corresponding matrix, a condition that is inherent in our preceding formulation.

In what follows, by making use of experimentally measured data for each type of nanocomposites, we first identify the corresponding interfacial parameters to well capture the quantitative creep behavior of that material. Once the interface constants are determined, their values will be employed in subsequent numerical calculations for the relaxation and strain-rate sensitivity analysis of pertinent nanocomposite. It is remarkable in passing that, to the best of author's knowledge, the strain-rate sensitivity and stress relaxation of graphene/polymer nanocomposites have not been studied in the preceding investigations, neither experimentally nor numerically.

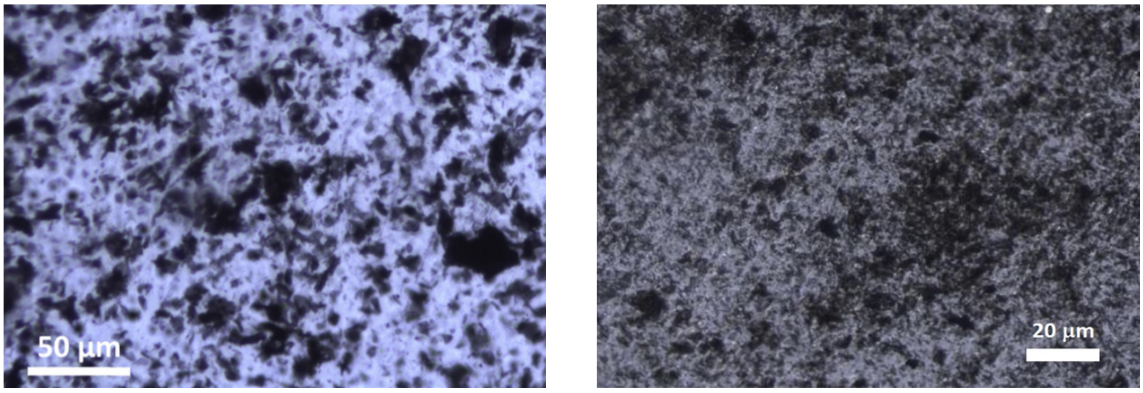

(a) (b)

Fig. 4.2. Microscopic images of graphene nanocomposites that will be examined numerically in Section 3 of present study: (a) TOM image of GNS/Polystyrene with filler content of 1.4 vol. % (Wang et al., 2015a), and (b) Optical image of GNS/Polylactide with filler content of 3 wt.% (Wang et al., 2015b).

4.3.1. Viscoelastic characteristics of graphene/Polystyrene nanocomposite

We first consider a nanocomposite consisting of graphene nanosheets distributed randomly within a Polystyrene matrix. The time-dependent creep behavior of such a material has been tested by Wang et al. (2015a) under tensile stress $\bar{\sigma}_{11} = 5$ MPa, at temperature 70 ^{o}C. For the numerical calculations, the graphene nanosheets are supposed to possess the average thickness of D = 0.5 nm with approximate aspect ratio of α = 1 x 10^{-3} (Tong et al., 2014; Wang et al., 2015a). Moreover, the in-plane elastic moduli of graphene fillers are considered to be $E_{33} = 1$ TPa and $\nu_{23} = 0.17$. These constants have been determined by Cadelano et al. (2010) based on the first-principles total-energy calculations in combination with the continuum elasticity. It is notable that these numerical values are in good agreement with the results of other investigations reported for the stiffness moduli of graphene and also bulk graphite in their basal plane (Scarpa, et al., 2010; Bera et al., 2010; Michel and Verberck, 2008; Gao and Huang, 2014; Kelly, 1981). The other three constants of graphene fillers, associated with its normal-to-plane properties, are assumed to be equal to those of single crystal graphite, such that $E_{11} = 36.5$ GPa, $\mu_{12} = 4$ GPa and $C_{12} = 15$ GPa (Kelly, 1981). Besides, the material constants of pure Polystyrene matrix, used in our numerical calculations, are supposed to be:

$E_0^M = 1.95$ GPa, $\eta_0^M = 1805$ GPa.s, $E_0^V = 7.5$ GPa, $\eta_0^V = 352$ GPa.s and $\nu_0 = 0.35$.

As mentioned earlier, we first examine the time-dependent creep of GNS/Polystyrene nanocomposite under the constant stress of $\bar{\sigma}_{11} = 5$ MPa. The calculated creep strains are shown in Fig. 4.3 at four graphene concentrations of c_1=0, 1.4, 2.4 and 3.9 vol.%.

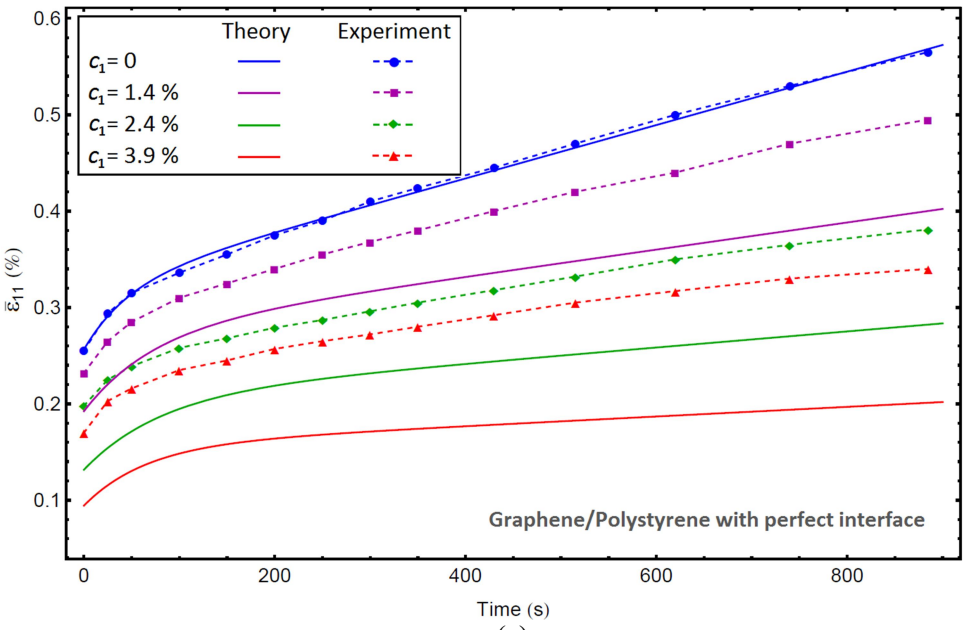

(a)

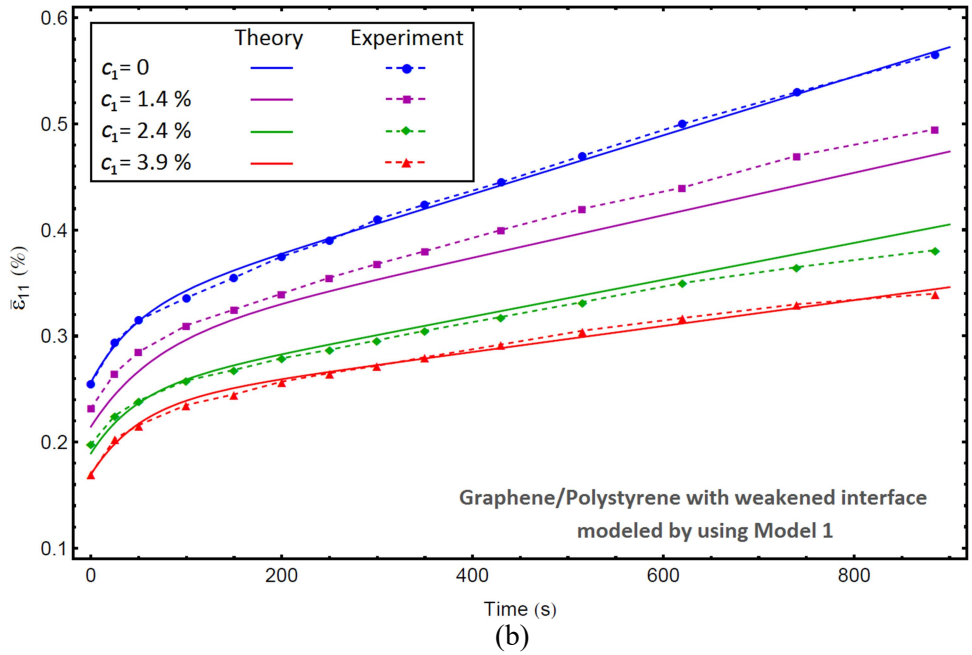

(b)

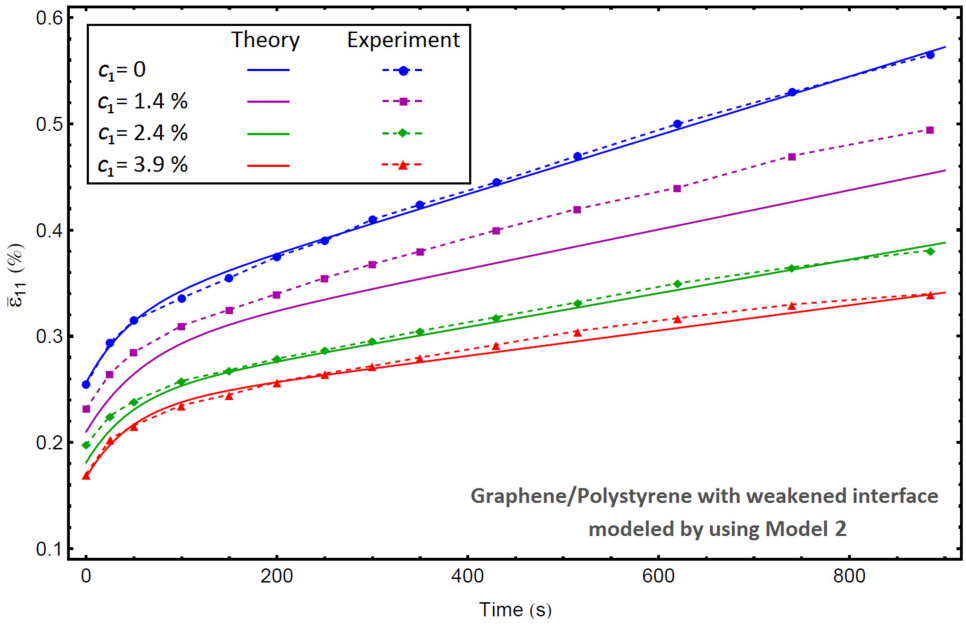

(c)

Fig. 4.3. Experimental data (dashed lines from Wang et al., 2015a) and theoretical results (solid lines) for creep response of graphene/Polystyrene nanocomposite with different GNS loadings. The solid curves in (a) were calculated under assumption of perfect interface, and curves in (b) were obtained by adopting model 1, with interfacial properties $E_{\text{int}}^{V} = 270$ MPa and $\eta_{\text{int}}^{V} = 18$ GPa.s, and theoretical results in (c) were calculated by using model 2, with $\gamma = 10^{-7.55}$ nm/MPa.

The solid curves in Fig. 4.3(a) were obtained by assuming that there is no interface effect, whereas the dashed curves are the experimental data taken from Wang et al. (2015a). It is evident that the theoretical curve for c_1 = 0% matches sufficiently well with the test data, implying that the four-parameter Burgers model is adequate to describes the creep behavior of Polystyrene. However, direct comparison between the computed results at c_1 = 1.4%, 2.4% and 3.9%, and the relevant experimental curves immediately reflects that our numerical results for the assumption of perfect interfacial bonding are substantially lower than the measured creep data. This is a strong evidence that the load transfer from matrix to graphene fillers, and vice versa, is not perfect. As a result, the weakened interface condition is

considered to calculate the creep strain for the same set of graphene loadings. In doing do, we first adopt the interface model 1 with interfacial properties $E_{\text{int}}^{V} = 270$ MPa and $\eta_{\text{int}}^{V} = 18$ GPa.s, in which the imperfect interface condition has been modeled by introduction of a weakened interphase layer with diminishing thickness between fillers and surrounding matrix. It is notable that there is no experimental measurement for the values of interfacial parameters. In view of that, the unknown constants E_{int}^{V} and η_{int}^{V} were determined numerically by matching the theoretical prediction with corresponding experimental results for creep behavior of GNS/Polystyrene nanocomposite. The theoretical results are illustrated as solid curves of Fig. 4.3(b). The calculated curves are now significantly higher than those theoretical results in Fig. 4.3(a). Even though the calculated results for c_1 = 1.4% and 2.4% are slightly different with the corresponding test data, the overall agreement is substantially better. In a similar fashion, we now call upon the interface model 2 with sliding parameter $\gamma = 10^{-7.55}$ nm/MPa to model the imperfect GNS-Polystyrene bonding by a displacement jump at the interface. Since our computed results were sensitive to the imperfect parameter, the value of γ was determined by matching the theoretical predictions with the corresponding test data for the creep response of nanocomposite. Fig. 4.3(c) shows the theoretical results (solid curves) along with the experimental data (dashed curves) for specified volume concentrations of GNSs. A comparison of new results with those of Fig. 4.3(a) reveals that the consideration of such a sliding interface significantly brought up the theoretical curves. In this way, the quantitative agreement between theoretical and experimental data sets now is substantially better, even though theoretical curves for c_1 = 1.4% and 2.4% are somewhat lower than the relevant test data. In general, Fig. 4.3 demonstrates that the measured creep data cannot be

well captured without considering the additional contribution of weakened interface condition; however, employing the imperfect interface models gives a very good prediction for the experimental data of GNS/Polystyrene nanocomposite. This clearly confirms the view that the interface effect is important, and it is the combination of our theory with the imperfect interface models that gives rise to a complete methodology for viscoelastic analysis of graphene/polymer nanocomposites.

We now study the time-dependent relaxation behavior of GNS/Polystyrene nanocomposite under a constant strain $\bar{\varepsilon}_{11} = 0.01$. Needless to mention that both imperfect interface models can be adopted here for the relaxation analysis of nanocomposite. For the sake of conciseness, however, we only demonstrate the theoretical results determined by employing the interface model 1. In doing so, we have used the interfacial constants $E_{\text{int}}^{V} = 270$ MPa and $\eta_{\text{int}}^{V} = 18$ GPa.s identified previously through the creep analysis of nanocomposite. The computed results for this nanocomposite with the perfect and weakened interface are shown in Fig. 4.4(a) and (b), respectively. It is obvious that the initial stress state under prefect interface condition is visibly higher due to the higher overall stiffness of composite system, while the stress state with an imperfect interface is lower. For instance, with the graphene concentration of c_1 = 3.9% the initial stresses are 56 MPa and 30 MPa for the perfect and imperfect interface conditions, respectively. This implies that the overall stiffness in the real graphene/Polystyrene is only about 54% of the ideal case of perfect bonding. This observation points to the importance of having a prefect interface in order to develop a stiffer graphene nanocomposite.

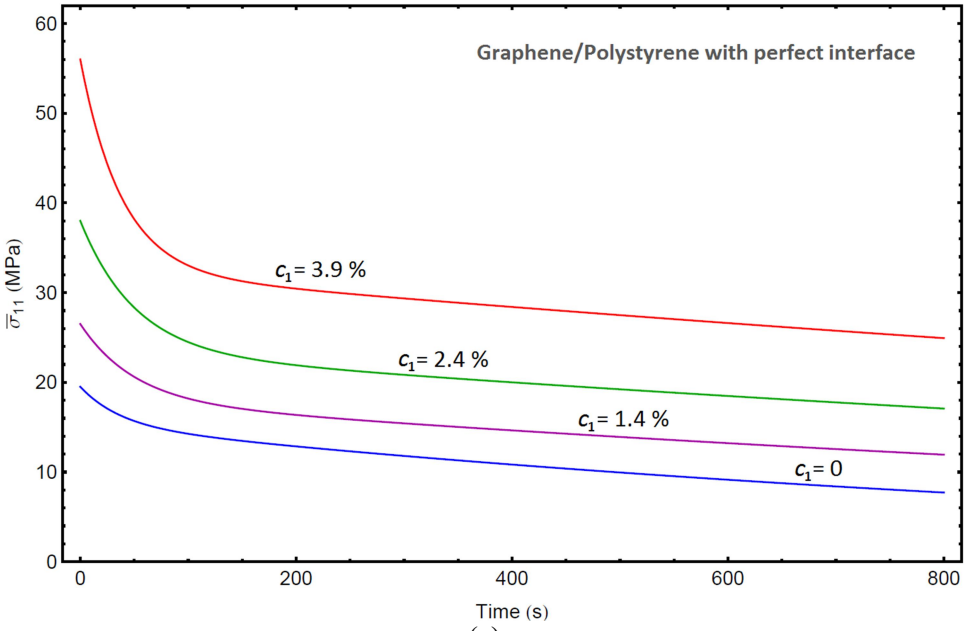

(a)

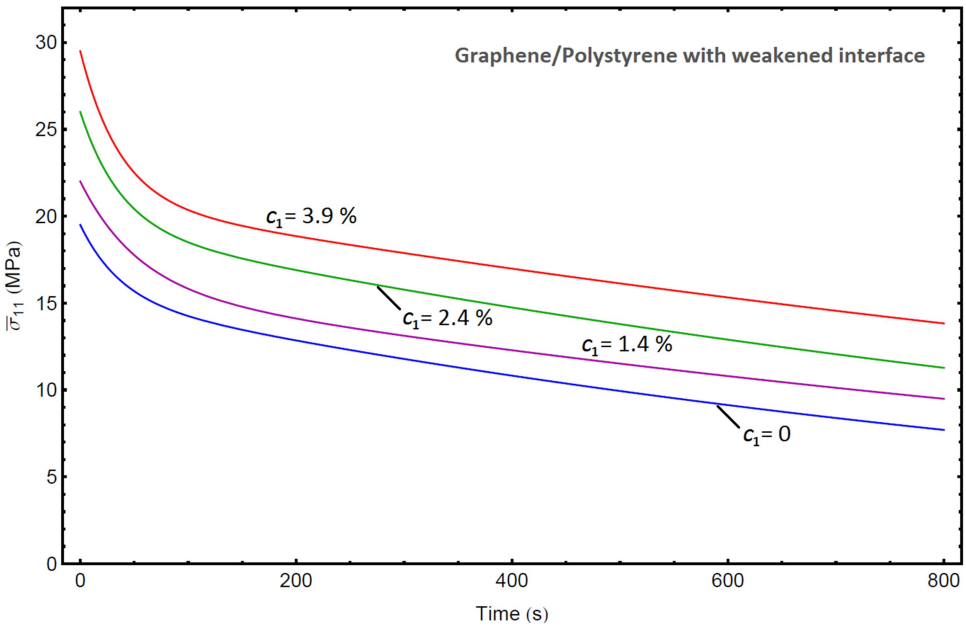

(b)

Fig. 4.4. Relaxation behavior of the graphene/Polystyrene nanocomposite with different GNS loadings, calculated for $\overline{\varepsilon}_{11} = 0.01$, under the assumptions of (a) perfect, and (b) weakened interface conditions.

Fig. 4.4 also reveals that the difference in the relaxation curves for various graphene loadings is more significant under the assumption of perfect interface than the imperfect one. In other words, the more interface contribution due to higher interface area at 3.9 vol.% in Fig. 4.4(b) has dramatically lowered its stress level to close the gap with the 2.4 vol.% one.

The stress-strain relations of graphene/Polystyrene nanocomposite are strain-rate dependent, due to the rate form of the constitutive equation of the polymer matrix. We now intend to study this issue by means of interface model 1 with interfacial constants $E_{\text{int}}^{V} = 270$ MPa and $\eta_{\text{int}}^{V} = 18$ GPa.s. In doing so, three orders of strain rates, at $\dot{\bar{\varepsilon}}_{11} = 10^{-4}$, 10^{-3} and 10^{-2} /s are employed in our calculation. For pure Polystyrene and nanocomposite with 3.9 vol.% graphene loading, the computed results are shown in Fig. 4.5(a) and (b) under the assumptions of perfect and imperfect interface conditions, respectively. It is seen from Fig. 4.5(a) that, for the perfect interface condition at each of the corresponding strain rates, the follow stress of nanocomposite is substantially higher than that of pure matrix. However, as shown in Fig. 4.5(b) for the case of imperfect interface, the flow stress of the graphene nanocomposite has significantly decreased. In fact, the viscoelastic stiffness of our nanocomposite is seen to be greatly compromised due to interface weakness regardless of the level of strain rate. It is conceivable that if the value of interfacial constant E_{int}^{V} is too low, the viscoelastic stiffness of the nanocomposite could become even lower than that of the pure matrix. This again points to the urgency of surface functionalization of graphene fillers for achieving an improved interface condition.

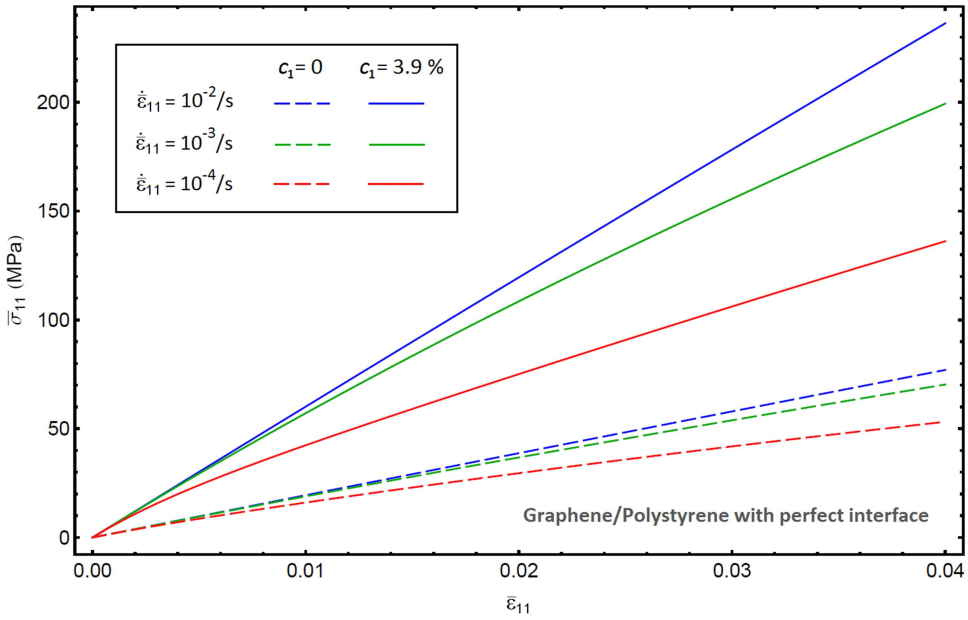

(a)

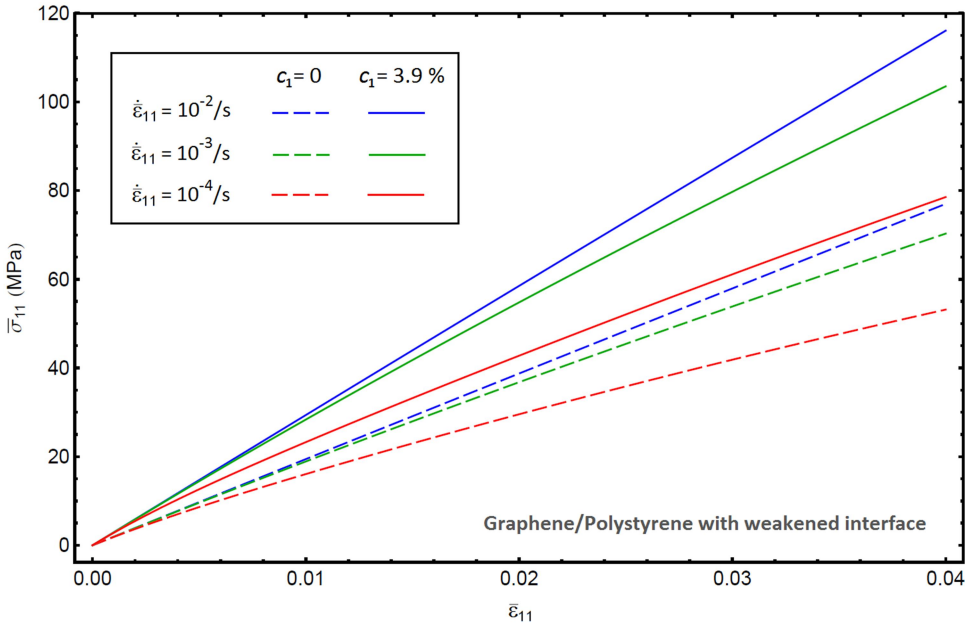

(b)

Fig. 4.5. Strain-rate sensitivity of the graphene/Polystyrene nanocomposite at the GNS loading of 3.9 vol.%, obtained under the assumptions of (a) perfect, and (b) weakened interface conditions.

4.3.2. Viscoelastic characteristics of graphene/Polylactide nanocomposites

We now employ the present theory to study the overall viscoelastic behavior of graphene/Polylactide nanocomposites. The time-dependent creep behavior of such a material has been tested by Wang et al. (2015b) under tensile stress $\bar{\sigma}_{11} = 1$ MPa, at temperature 35 ^{o}C. In order to make necessary contact with the existing literature, we particularly consider following nanocomposites reported by Wang et al. (2015b),

- Thick GNP/Polylactide composite: Long stacks of graphene layers (say thick GNPs), with the average thickness and aspect ratio of D = 25 nm and α = 2 x 10^{-3}, have been incorporated in the polymer matrix.
- Thin GNP/Polylactide composite: Short stacks of graphene layers (say thin GNPs), with the average thickness and aspect ratio of D = 5 nm and α = 10^{-3}, have been involved in the polymer matrix.
- GNS/Polylactide nanocomposite: GNSs, with the average thickness and aspect ratio of D = 1 nm and α =0.2 x 10^{-3}, have been incorporated in the Polylactide matrix.

It is notable that the filler loading in all abovementioned nanocomposites is taken to be identical at 3 wt.%, as specified in Wang at al. (2015b). In the light of these case studies, we can also uncover the influence of geometries of fillers on the viscoelastic characteristics of graphene/polymer nanocomposites with the imperfect interface. In following numerical calculations, the material constants for polymer matrix are considered to be

$E_0^M = 2.3$ GPa, $\eta_0^M = 3300$ GPa.s, $E_0^V = 14$ GPa , $\eta_0^V = 390$ GPa.s and $\nu_0 = 0.36$.

which have been determined from the corresponding creep test data for pure Polylactide.

We first study the creep behavior of the graphene/Polylactide nanocomposite, under the constant stress of $\bar{\sigma}_{11} = 1$ MPa. The calculated creep strains are shown in Fig. 4.6 for pure Polylactide matrix and three examples of nanocomposites listed above. The dashed curves in Fig. 4.6(a) pertain to experimental data taken from Wang et al. (2015b), whereas solid curves have been obtained by the present theory for the perfect interface condition. We readily recognize that the theoretical curve for pure Polylactide fully captures the corresponding test data, implying that the four-parameter Burgers model well describes the creep behavior of Polylactide matrix. However, a comparison between the solid and counterpart dashed curves for nanocomposites immediately reveals that theoretical results for perfect interfacial bonding are significantly lower than the experimentally measured data. This implies that the load transfer between inclusions and surrounding Polylactide matrix is not perfect. To address this issue we then call upon interface model 2, by which the imperfect interface condition is modeled by a displacement jump at the graphene-Polylactide interface (interface model 1 also could be used in present analysis, but, for the sake of conciseness we only demonstrate the results obtained by adopting interface model 2). In this process, interfacial sliding parameters are identified by matching our theoretical results with corresponding creep data for each case of graphene/Polylactide nanocomposite, as:

- Thick GNP/Polylactide nanocomposite: $\gamma = 10^{-4.53}$ nm/MPa

- Thin GNP/Polylactide nanocomposite: $\gamma = 10^{-4.86}$ nm/MPa

- GNS/Polylactide nanocomposite: $\gamma = 10^{-5.59}$ nm/MPa

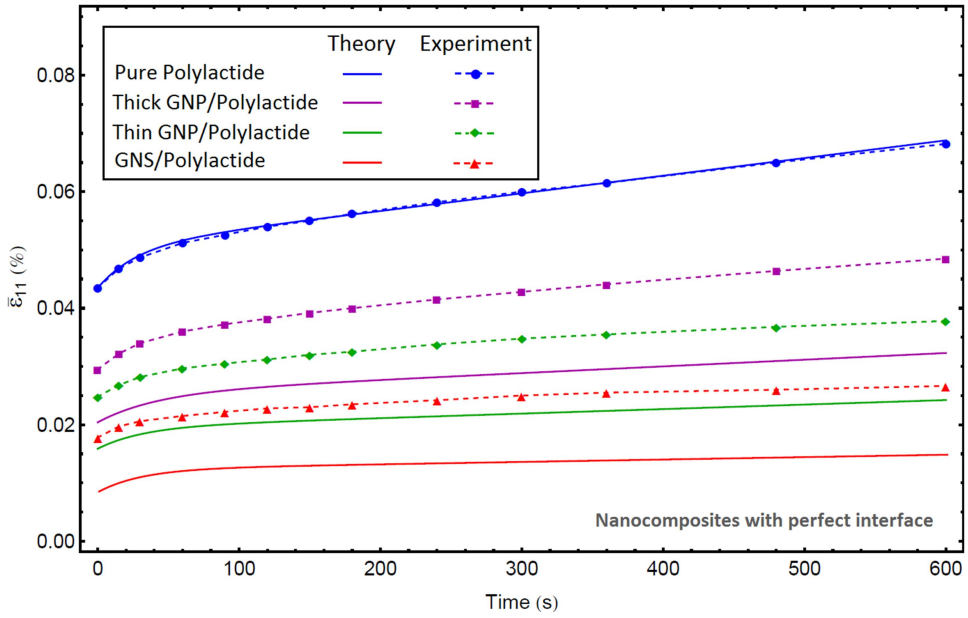

(a)

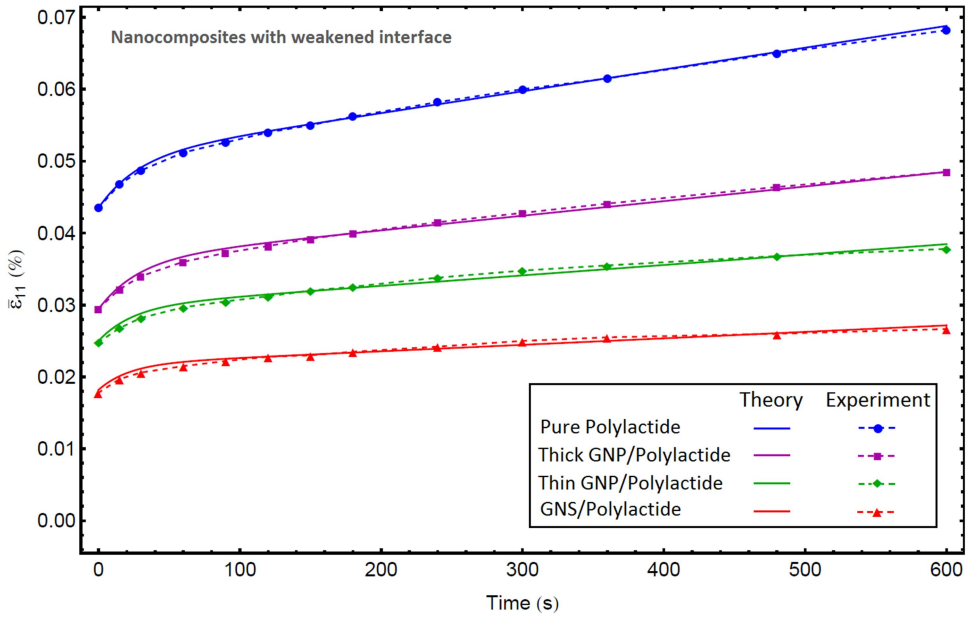

(b)

Fig. 4.6. Experimental data (dashed lines from Wang et al., 2015b) and theoretical results (solid lines) for the creep response of graphene/Polylactide nanocomposite with different types of fillers at identical concentration of 3 wt.%. The solid curves in (a) were calculated under the assumption of perfect interface, and curves in (b) were obtained by employing imperfect interface model 2.

The computed results for nanocomposites with imperfect interface are shown as solid curves of Fig. 4.6(b), along with the dashed lines which pertain to corresponding test data. It is evident that our theoretical calculation now matches almost perfectly with the experimental measurements for all types of nanocomposites. This observation proves that it is the combination of our original homogenization scheme with the imperfect interface models that eventually leads to a complete theory for the viscoelastic analysis of graphene-based nanocomposites.

Next, we examine the relaxation behavior of graphene/Polylactide nanocomposite under constant strain, $\bar{\varepsilon}_{11} = 0.01$. For pure Polylactide matrix and subsequent graphene-based nanocomposites, the calculated results have been depicted in Fig. 4.7(a) and (b), respectively, under the assumption of perfect and imperfect interface conditions. As we expected, for all cases the initial stress state under the perfect interface is higher due to higher overall stiffness of corresponding nanocomposite, while the stress state with a weak interface is significantly lower. Moreover, it is evident that the initial stresses at GNS/Polylactide nanocomposite are 113 MPa and 55 MPa for perfect and weakened interface conditions, respectively, implying that stiffness in the real GNS/Polylactide nancomposite is only 48% of the ideal case of perfect bonding. On the other hand, for the thin and thick nanoplatelets the overall stiffness in real nanocomposites with imperfect interface are respectively about 60% and 68% of the ideal composites with the perfect interfacial bonding. Accordingly, we can conclude that the interface condition plays a more profound role in the overall response of GNS/Polylactide nanocomposite.

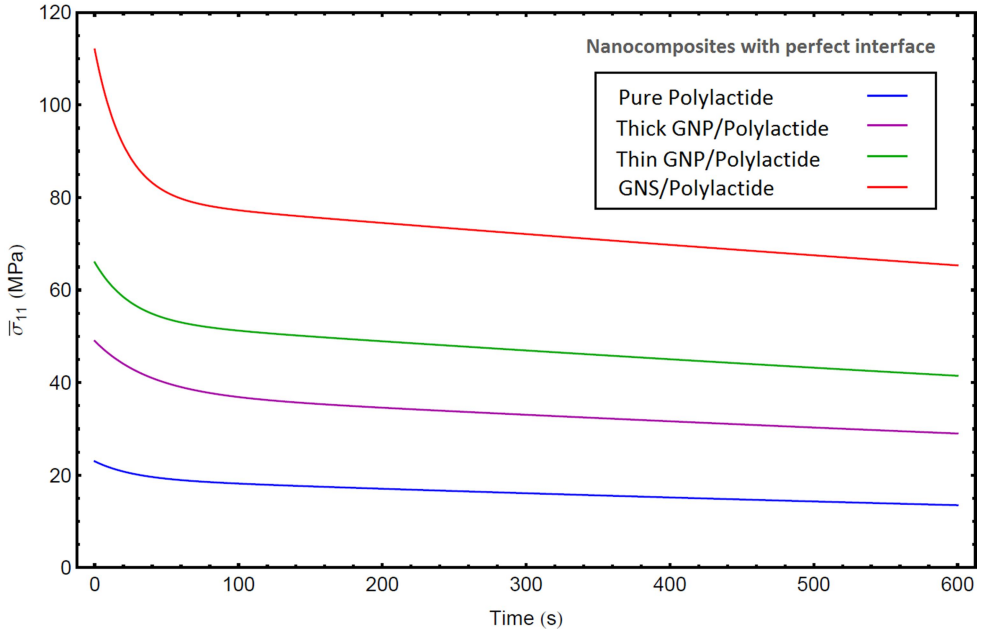

(a)

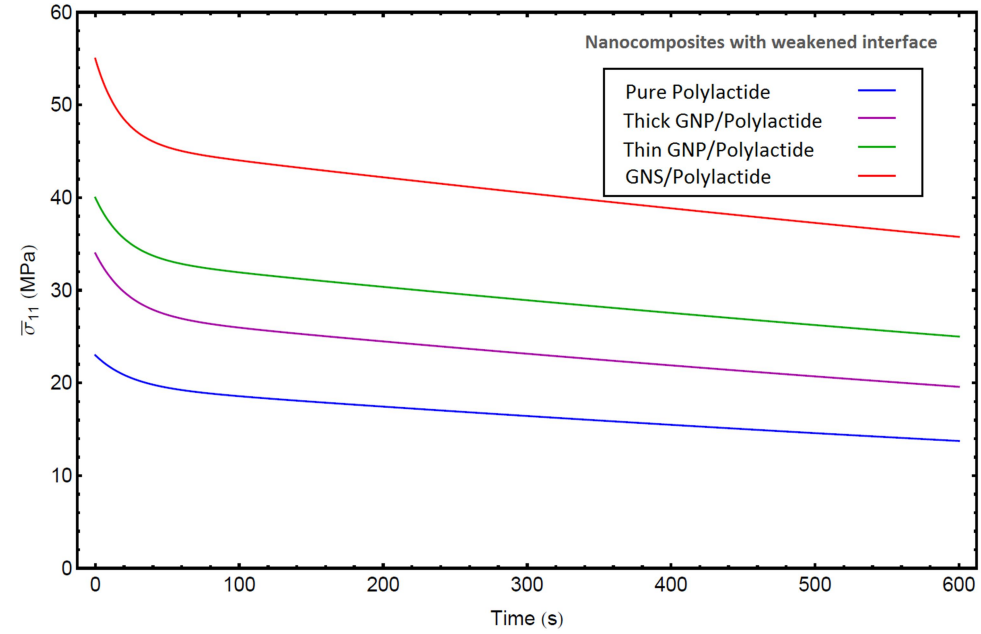

(b)

Fig. 4.7. Relaxation behavior of graphene/Polylactide nanocomposites with different types of fillers at the identical concentration of 3 wt.%, calculated for $\bar{\varepsilon}_{11} = 0.01$: (a) perfect interface model, and (b) weakened interface model.

As shown in Fig. 4.7(a), under the assumption of perfect interface condition the difference in relaxation curves between GNS/Polylactide nanocomposite with the other composites is relatively significant. However, it is evident from Fig. 4.7(b) that the interface effect has lowered the stress level of GNS/Polylactide nanocomposite, more drastically than the stress level in thin and thick GNP/Polylactide composites. This observation indicates that, in comparison with GNP/Polylactide composites, the overall behavior of GNS/Polylactide nanocomposite is relatively more sensitive to its interface quality. This higher sensitivity to the interface condition is due to the extreme geometry of graphene nanosheets which intensifies the influence of weak interface condition on the overall response of GNS/polymer composite. In view of this observation, one can conclude that a little improvement in the GNSs-polymer interface condition can lead to a significant beneficial impact on the stiffness and long-term performance of a GNS/Polymer nanocomposite.

The closing part of this section is devoted to strain-rate sensitivity analysis of graphene/Polylactide nanocomposites. Let us consider the constant strain rate of $\dot{\varepsilon}_{11} = 10^{-2}$ /hr. The theoretical prediction for strain-stress relations of Polylactide matrix and nanocomposites are illustrated in Fig. 4.8(a) and (b), respectively, for the conditions of perfect and imperfect interfacial bondings. The nonlinear strain-stress relation for all graphene/Polylactide nanocomposites is evident in these figures. It is further seen from Fig. 4.8(a) that the flow stress of GNS/Polylactide nanocomposite with perfect interface is substantially higher than that of thin or thick GNP/Polylactide composites. However, as shown in Fig. 4.8(b), the flow stress of the GNS/Polylactide composite with a weakened interface has significantly decreased to a lower state, to close the gap with other nanocomposites, implying that the

viscoelastic stiffness of that nanocomposite is greatly compromised due to the imperfect load transfer at GNSs-Polylactide interface.

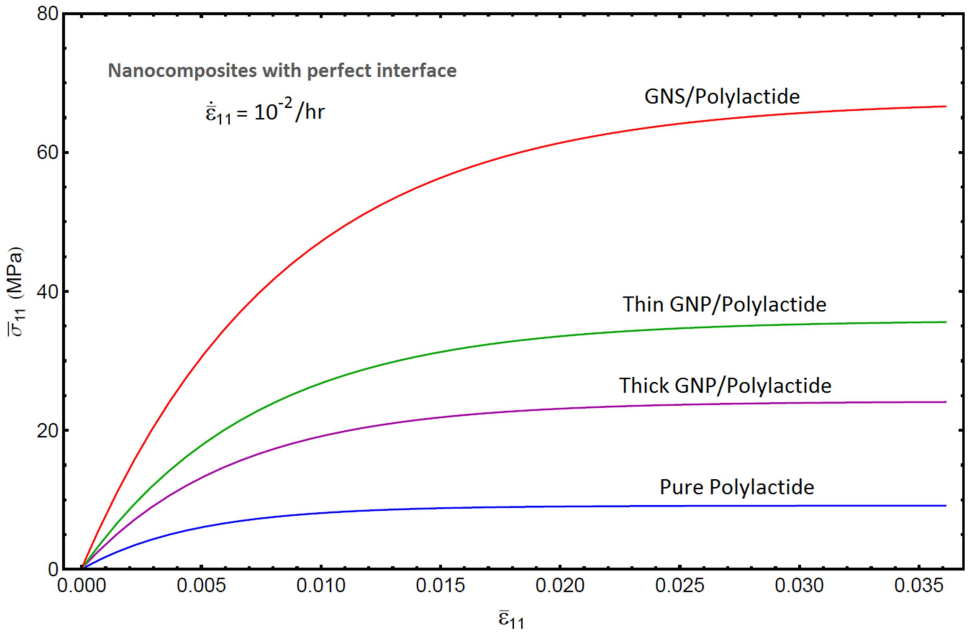

(a)

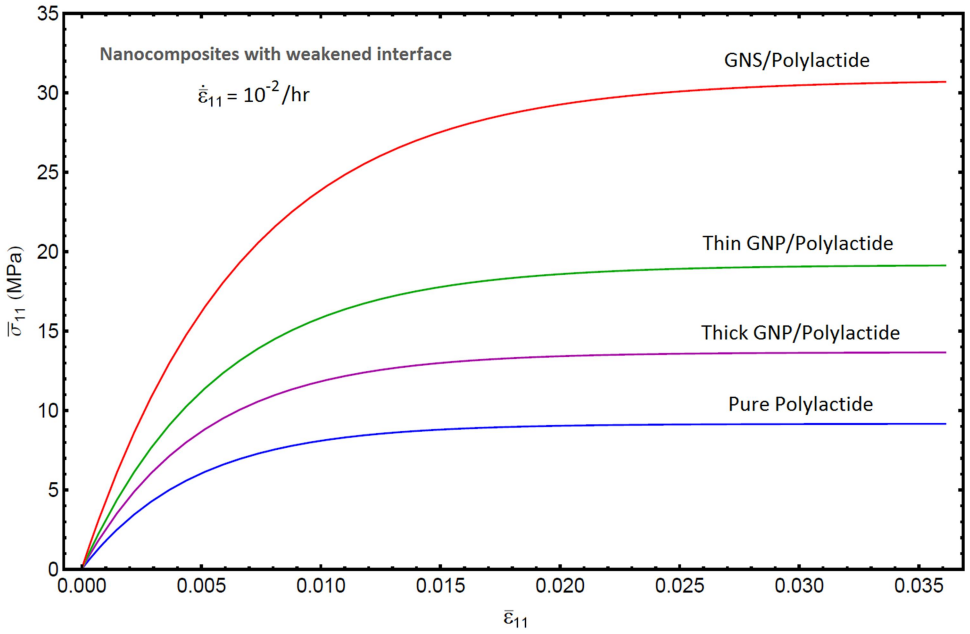

(b)

Fig. 4.8. Strain-stress relation of nanocomposites with different types of graphene-based fillers at the identical concentration of 3 wt.%, under assumptions of (a) perfect and (b) weakened interface conditions.

4.4. Concluding remarks

In order to study the viscoelastic characteristics of a graphene/polymer nanocomposite, first we presented a homogenization scheme in conjunction with two different approaches for treatment of imperfect interface between the constituent phases. Next, we applied the proposed theory to uncover the interface effect on the time-dependent creep, stress relaxation and stress-rate sensitivity of nanocomposite at various concentrations and aspect ratios of graphene fillers. Through consideration of experimentally measured data for various examples of nanocomposites, i.e. graphene/Polystyrene and graphene/Polylactide materials, we have demonstrated that without accounting for the imperfect interface the predicted creep compliances are too stiff; however, with the introduction of a weakened interface in our model, the quantitative behavior of experimental creep curves can be well captured. In addition, both stress relaxation and stress-strain relations were also found to greatly depend on the interface condition. The findings of this investigation could have a significant impact on the long-term durability and reliability of graphene nanocomposites, indicating that continued improvement in the surface functionalization is necessary to realize the full potential of graphene reinforcement. Besides, the robustness and applicability of developed theory encouraged us to propose it as a simple but yet widely useful tool for the viscoelastic analysis of graphene-based nanocomposites, instead of doing heavy computational simulations or recurring onerous experimental investigations. The availability of such a explicit expressions for the overall viscoelastic properties of graphene/polymer nanocomposites with imperfect interface can be greatly valuable in the design and optimization of high performance materials for a broad range of new applications.

Chapter 5.

Electrical conductivity and permittivity of graphene nanocomposites with percolation threshold, microcapacitor and electron-tunneling effects

5.1. Overview

As mentioned earlier, the addition of highly conductive graphene fillers into polymer matrix to form a nanocomposite with tunable electrical properties has stimulated a surge of scientific interests from the research communities. In this regard, a large number of conductive nanocomposites have been fabricated and characterized by incorporating graphene fillers in different polymers, e.g. epoxy, polypropylene, poly(vinylidene fluoride), polystyrene, etc. The most interesting common aspect of reported composites is that all enhancements in their electrical properties are observed at a very low concentration of graphene fillers, referred to as percolation threshold. This fundamental characteristic is the result of several possible mechanisms with complex natures. Even at extremely low filler concentrations many graphene fillers may be in direct contact with each other, because of their high aspect ratios. This results in the formation of several macroscale conductive pathways through the entire composite. Moreover, originated from the quantum mechanics of materials the electrons have the ability of hoping through two neighboring graphene sheets separated by a thin insulating film; this hoping property could enhance the conduction along the pathways. In view of this, a combination of mechanisms (i.e. direct particle-particle contact, electron tunneling and

intrinsic conduction of fillers) is responsible for the formation of conductive networks in graphene composites, which contributes to a sharp increase of their effective conductivity over a very narrow range near the percolation threshold.

Furthermore, graphene nanocomposites are very appealing for recent applications in electromagnetic shielding and high-energy-density capacitors, owing to unique property of dramatic increase in their dielectric constants near the percolation threshold (see Liang et al., 2009; Varrla et al., 2011; Singh et al., 2011; Gómez et al., 2011; Zhang et al., 2010; Huang et al., 2014). The pronounced enhancement in effective permittivity of graphene nanocomposites near their percolation threshold can be explained in the light of so-called microcapacitor effect (Wang et al., 2013; Liu et al. 2014; Shang et al., 2012; Kim et al., 2013; Cui et al., 2011; Fan et al., 2012; Dang et al., 2012). In fact, around the percolation limit many graphene fillers are isolated by very thin layers of polymer. This forms lots of microcapacitor structures throughout the composite, which significantly increase the intensity of local electric filed just around the conductive fillers. Consequently, this process promotes the charge carriers to migrate and then accumulate at the fillers-matrix interfaces. This interfacial effect, also known as Maxwell-Wagner-Sillar polarization, is the main reason for enhancement of effective dielectric property of pertinent graphene nanocomposites at low frequency. However, some geometrical and manufacturing parameters, e.g., aspect ratio of graphene sheets, electrochemical functionalization of graphene-matrix interface, and the homogeneity of filler dispersion in matrix, can affect the probability of microcapacitor formation in nanocomposite material.

Inspired by the unique properties mentioned above, a quantitative prediction on the overall electrical behavior of graphene composites is essential for the design and optimization of new high performance materials and devices. However, an accurate modeling of graphene composites is challenging due to the complex nature of existing physical processes, i.e. formation of percolation networks and microcapacitors throughout the composite material. Because of the multi-scale nature of this problem, the other difficulty in modeling of these nanomaterials lies in relating the microscopic characteristics of their internal microstructures to the macroscopic properties of interest. For instance, the numerical contrast of graphene electrical conductivity compared with most polymers is in the order of 10^{11}-10^{21}. Moreover, the aspect ratio and surface area of graphene is very large in comparison with conventional fillers. Therefore, from the continuum prospective we are dealing with a high contrast and high aspect ratio problem which is dramatically different from the classical cases treated by the conventional continuum models. A thorough investigation of literature reveals that although considerable experimental efforts have been made in exploring the properties of graphene composites, the theoretical and computational studies on these materials are rarely reported. As the most common computational treatment for this class of problems, Monte Carlo (MC) simulation recently has been employed to calculate the conductivity of graphene composites (Hicks et al., 2009; Fan et al., 2015; Li and OStling, 2013; Safdari and Al-Haik, 2012). MC simulation can provide a valuable insight into the microscopic processes; however, its high computational expense undermines its capability for the simulation of systems where fillers have extreme range of geometry and material properties. Recognizing the potential gain that theoretical models could deliver, several notable investigations with

the continuum backbone have been reported for the treatment of different types of conductive carbonaceous nanocomposites, in particular CNT-based composites (Yan et al., 2007; Deng and Zheng, 2008; Seidel and Puydupin-Jamin, 2011; Berhan and Sastry, 2007; Gardea and Lagoudas, 2014; Wang et al., 2014). A series of homogenization theories, addressed in these investigations, potentially could be developed and then applied to the graphene nanocomposites. To the best of authors' knowledge, existing models suffer from several limitations. As the most important shortcoming, all previous investigations are pertinent to the Direct Current (DC) conductivity of carbonaceous nanocomposites; none addressed the Alternating Current (AC) properties of these materials in the light of homogenization models. Besides, some of adopted models in previous investigations did not possess a percolation threshold and had to borrow this critical feature from other models. For instance, Kim et al. (2015) recently employed the modified Mori-Tanaka theory to calculate the effective conductivity of graphene composites. However, in order to incorporate the important parameter of percolation threshold in their formulation they had to adopt the hard/soft core model, which was originally developed by Berhan and Sastry (2007) based on the MC simulation. It is notable that when the percolation threshold has to be borrowed from other theory, it implies that the developed homogenization scheme is not self-contained. This is an issue that we want to avoid in present study.

This chapter concerns with the determination of effective conductivity and permittivity constants of graphene nanocomposites in the AC electrical conditions. To do so, we first call upon a self-consistent effective medium theory as the backbone of our analysis. Although the formation of conductive networks and microscale capacitors is difficult to be simulated in a

continuum methodology, we will include their effects in a phenomenological way so that these physical processes will not be completely lost. Accordingly, the electron tunneling and formation of microcapacitors will be taken as two statistical processes that their effects on the interfacial properties can be characterized by the appropriate probability functions. At the end, upon consideration of an example of graphene/polymer nanocomposite it will be shown that the proposed methodology can quantitatively capture the experimental data of corresponding material.

5.2. Theory

Consider a two-phase heterogeneous body with a polymer matrix and 3D randomly oriented graphene fillers of common spheroidal shapes and almost same dimensions. Suppose that graphene nanocomposite is subjected to an AC electrical loading, say harmonic electric field. Subsequently, the long-term response of the composite material and its constituent phases is also harmonic. In order to keep the necessary connection with the literature, the parallel combination of a capacitor and a resistor could be employed here as the equivalent circuit model for the simulation of the nanocomposite in the AC setting. In light of this equivalency, the electric field in the composite system, $\mathbf{E}$ and corresponding electric density, $\mathbf{J}$ are then related to each other through

$$\mathbf{J} = \boldsymbol{\sigma}_e^* \mathbf{E}, \tag{5.1}$$

in which $\boldsymbol{\sigma}_e^*$ is the effective complex conductivity tensor of the nanocomposite, written as

$$\boldsymbol{\sigma}_e^* = \boldsymbol{\sigma}_e + j\boldsymbol{\varepsilon}_e\omega, \tag{5.2}$$

where $\boldsymbol{\sigma}_e$ and $\boldsymbol{\varepsilon}_e$, respectively, are unknown conductivity and permittivity tensors of effective medium, j is the imaginary number, and $\omega = 2\pi f$, in which f is the corresponding AC frequency. Likewise, the electric density amplitude vector of kth constituent phase, $\mathbf{J}_k$ ($k \equiv m$ or g), can be expressed in terms of associated electric field, $\mathbf{E}_k$, as $\mathbf{J}_k = \boldsymbol{\sigma}_k^* \mathbf{E}_k$ in which $\boldsymbol{\sigma}_k^* = \boldsymbol{\sigma}_k + j\boldsymbol{\varepsilon}_k\omega$. Our objective in the present study is to establish how the effective conductivity and permittivity of nanocomposite, $\boldsymbol{\sigma}_e$ and $\boldsymbol{\varepsilon}_e$ depend on the electrical properties of its constituent phases for a given frequency.

Several micromechanical theories could be invoked here as the backbone of present study; however, in order to capture the important futures of the percolative conduction as an integral part of our continuum model, we shall adopt the self-consistent effective medium theory in conjunction with complex conductivity moduli for the constituents. In retrospect, different ways can be adopted here to derive the self-consistent effective medium theory. The simplest one is the Maxwell's approach of far-field matching, as recently formulated by Weng (2010). So, in order to pave the way for our analysis in the most concise way, we then briefly recapitulate the Maxwell's approach, but written in terms of complex conductivity tensors of the constituents. Consider a representative volume element (RVE) of composite system, which is embedded in an infinitely extended homogenous reference medium with conductivity tensor of $\boldsymbol{\sigma}_r^*$. The matrix and graphene fillers in corresponding RVE carry volume concentrations of c_m and c_g, respectively (with $c_\mathrm{m} + c_\mathrm{g} = 1$). Now, suppose that the RVE under consideration could be replaced by an equivalent homogenous composite element with the same volume but yet unknown effective tensor, $\boldsymbol{\sigma}_e^*$, which is embedded in the same

infinitely extended reference medium. According to the Maxwell's far-field matching principle, this equivalency is theoretically possible just if the scattered field in both cases can be equal. Accordingly, the consistency condition associated with these equivalent RVEs can be written as:

$$c_m\left[\left(\boldsymbol{\sigma}_m^*-\boldsymbol{\sigma}_r^*\right)^{-1}+\mathbf{S}_m\,\boldsymbol{\sigma}_r^{*\,-1}\right]^{-1}+c_g\left[\left(\boldsymbol{\sigma}_g^*-\boldsymbol{\sigma}_r^*\right)^{-1}+\mathbf{S}_g\,\boldsymbol{\sigma}_r^{*\,-1}\right]^{-1}=\left[\left(\boldsymbol{\sigma}_e^*-\boldsymbol{\sigma}_r^*\right)^{-1}+\mathbf{S}_e\,\boldsymbol{\sigma}_r^{*\,-1}\right]^{-1}, \tag{5.3}$$

in which $\mathbf{S}$ is the shape-dependent depolarization tensors of associated phases. Now, according to the self-consistent theory the electrical property of the reference medium can be assumed to be that of the effective medium, so that $\boldsymbol{\sigma}_r^*=\boldsymbol{\sigma}_e^*$. Since there is no scattering field induced by the effective medium RVE, embedded in an infinitely extended effective medium, the right-hand side of Eq. (5.3) then automatically vanishes. Meanwhile, since the inclusions are randomly oriented in the 3D space the orientational average of remaining terms must be taken. In this way, the effective medium theory for the overall electrical behavior of a medium with random microstructure can be represented by:

$$c_0\left\langle c_m\left[\left(\boldsymbol{\sigma}_m^*-\boldsymbol{\sigma}_r^*\right)^{-1}+\mathbf{S}_m\,\boldsymbol{\sigma}_r^{*\,-1}\right]^{-1}\right\rangle+c_1\left\langle c_g\left[\left(\boldsymbol{\sigma}_g^*-\boldsymbol{\sigma}_r^*\right)^{-1}+\mathbf{S}_g\,\boldsymbol{\sigma}_r^{*\,-1}\right]^{-1}\right\rangle=0, \tag{5.4}$$

where the curly brackets $\langle\cdot\rangle$ denotes the orientational average of the said quantity. This equation applies to constituent phases with general anisotropy, but in following formulation we will focus on our specific case of study, in which the matrix is isotropic and graphene fillers are transversely isotropic. In view of this methodology, the conductivity and permittivity of matrix will be taken to be σ_0 and ε_0, respectively. On the other hand, taking direction-3 as the symmetric axis of a given graphene filler with idealized oblate geometry, its transvers (or normal-to-plane) conductivity and permittivity will be denoted by σ_3 and

ε_3, respectively, while its associated in-plane properties will be considered to be $\sigma_2 = \sigma_1$ and $\varepsilon_2 = \varepsilon_1$. Meanwhile, in the view of axisymmetric geometry of graphene fillers their depolarization tensor is also transversely isotropic. The nonzero components of tensor $\mathbf{S}_1$ for the oblate inclusions can be expressed as:

$$S_{11} = S_{22} = \frac{\alpha}{2\left(1-\alpha^2\right)^{\frac{3}{2}}}\left[\cos^{-1}\alpha - \alpha\left(1-\alpha^2\right)^{\frac{1}{2}}\right], \tag{5.5}$$

and $S_{33} = 1 - 2S_{11}$, where α is the aspect ratio (thickness-to-diameter ratio) of graphene fillers with the range of $\alpha < 1$. On the other hand, owing to random microstructure of nanocomposite and subsequent isotropic nature of effective medium, the effective shape of matrix could be envisioned to be spherically symmetric, so that $\mathbf{S}_m$ carries the components of 1/3 in all directions. Now, upon substituting the depolarization and complex conductivity tensors of the graphene fillers, polymeric matrix and the composite material into Eq. (5.4), the effective medium formula for the graphene nanocomposite can be written as:

$$\frac{c_0\left(\boldsymbol{\sigma}^*_0 - \boldsymbol{\sigma}^*_e\right)}{\boldsymbol{\sigma}^*_e + \left(\boldsymbol{\sigma}^*_0 - \boldsymbol{\sigma}^*_e\right)/3} + \frac{c_1}{3}\left\{\frac{2\left(\boldsymbol{\sigma}^*_1 - \boldsymbol{\sigma}^*_e\right)}{\boldsymbol{\sigma}^*_e + S_{11}\left(\boldsymbol{\sigma}^*_1 - \boldsymbol{\sigma}^*_e\right)} + \frac{\left(\boldsymbol{\sigma}^*_3 - \boldsymbol{\sigma}^*_e\right)}{\boldsymbol{\sigma}^*_e + S_{33}\left(\boldsymbol{\sigma}^*_3 - \boldsymbol{\sigma}^*_e\right)}\right\} = 0 \tag{5.6}$$

Upon substitution of $\boldsymbol{\sigma}^*_n$ (n = 0, 1 and 3) in this formula, one can obtain the effective conductivity and permittivity of nanocomposite, σ_e and ε_e.

The percolation threshold, c^*_g at low frequencies $(\omega \approx 0)$ can be determined directly from Eq. (5.6) by adopting following procedure. In general, the matrix is almost insulating while graphene fillers are highly conducive. Therefore, σ_i (i = 1 or 3, the same below) are usually several orders of magnitude larger than σ_0, which makes $\sigma_0 / \sigma_i \to 0$. According to the

percolation theory, when $c_g < c_g^*$, σ_e will have almost the same order of magnitude as σ_0, but after $c_g > c_g^*$, σ_e will approach σ_i. Therefore at $c_g = c_g^*$, σ_e is at the transition stage, with both $\sigma_e / \sigma_i \to 0$ and $\sigma_e / \sigma_0 \to \infty$ at the same time. Applying these conditions to Eq. (5.6) and solving for c_g^*, we arrive at

$$c_g^* = \frac{18S_{11}^2 - 9S_{11}}{18S_{11}^2 - 3S_{11} - 4}, \tag{5.7}$$

in which, S_{11} depends on the aspect ratio of the oblate graphene fillers, α. So, c_g^* is strictly a geometrical parameter, which represents the onset of the connective networks through the nanocomposite. We use Eq. (5.7) to plot the dependence of c_g^* on α in Fig. 5.1. This figure also shows a dashed curve plotted by the equation $c_g^* = \alpha$, which is given by Pan et al. (2011) for the onset of percolation in a composite material with oblate particles. Their formulation was based on consideration of a Ponte Castañeda–Willis (PCW) microstructure for a nanocomposite. It can be seen in Fig. 5.1 that c_g^* decreases by decreasing aspect ratio of oblate fillers, as we expected. Moreover, for spherical inclusions, we get $c_g^* = 1/3$, which is a value in agreement with published results (Pike and Seager, 1974; Balberg et al., 1984). Also, for the thin oblate inclusions $(\alpha \le 0.1)$ it appears that the feature of our results for onset of percolation is in close agreement with c_g^* given by Pan et al. (2011).

As mentioned earlier, as a result of chemical interactions during the manufacturing process of nanocomposites, a transition zone undesirably forms between the reinforcing inclusions and the matrix. Even though this interphase layer is very thin (say interface), its condition plays a

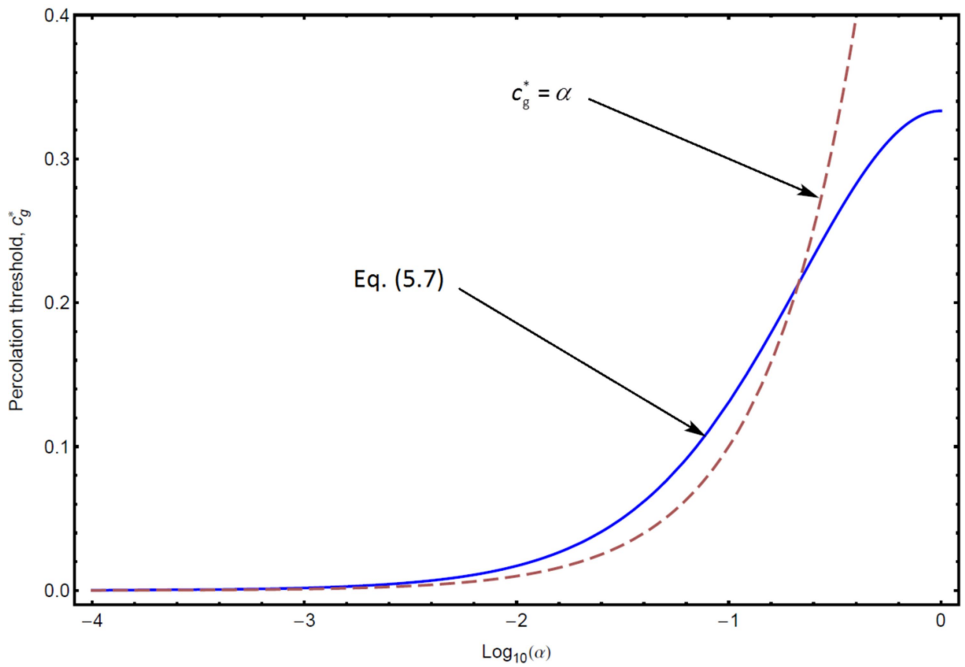

Fig. 5.1. Percolation threshold for the graphene fillers as a function of the inclusion aspect ratio.

profound role in controlling the mechanical, thermal and electrical phenomena in nanocomposites. On the other hand, the influence of some complex physical phenomenon, such as the interfacial tunneling and Maxwell-Wagner-Sillars polarization effects, can be characterized in a phenomenological way by the statistical modification of interfacial properties. It is a well-established phenomenon that the electron hoping from one filler to the surface of other fillers can lead to an enhanced conductivity in the graphene nanocomposite. The electron tunneling is of quantum nature, hence, it is difficult to be simulated in a continuum fashion. However, through a phenomenological way we can model it as a physical process which substantially enhances the electrical connectivity between the graphene filler and its surrounding effective medium. In this light, the tunneling activity will be taken as an added contribution to the interfacial conductivity of fillers, which can be facilitated with the formation of percolating paths throughout the nanocomposite. Besides, the significant

increase of effective dielectric constant around the percolation threshold can be mainly attributed to the formation of microcapacitor structures in nanocomposite which leads to interfacial polarization at the fillers-matrix interfaces. Namely, each of two neighboring graphene fillers can be treated as a local microscale capacitor with the fillers as two electrodes and a very thin polymer layer in between as dielectric. This gives rise to a substantial increase in the intensity of local electric field around the fillers, which subsequently promotes the charge carriers to migrate and accumulate at the interface of electrodes. The large specific area of fillers provides numerous sites for this interfacial polarization. Accordingly, a network of microcapacitors expands throughout the nanocomposite with increasing the filler content. Around the percolation threshold each microcapacitor contributes an abnormally large capacitance because of small distance between the electrodes. This large capacity is correlated with a significant increase in the effective permittivity of nanocomposite. Upon adopting a phenomenological approach, the formation of microscale capacitors can then be modeled as an additional contribution to interfacial permittivity of fillers, through the observation that the charge carriers accumulate at the fillers' interface due to abovementioned microcapacitor effect.

In view of the physical motives mentioned above, the incorporation of interphase effect into our continuum theory is inevitable. To address this issue, we assume that a very thin layer of material with uniform thickness exists between the graphene fillers and matrix. This thin layer and the core filler then from a thinly-coated inclusion system, in which the volume concentration of the interface (or thin interphase) is denoted as c_{int}, and that of core inclusion as $1\text{-}c_{\text{int}}$. In this way, the volume fraction of original graphene in the inclusion system can be

written as $1-c_{\text{int}} = D^3 / \left[\left(D+2t \right) \left(D+2\alpha t \right)^2 \right]$, where t denotes the thickness of interlayer, and D and α are the thickness and aspect ratio of thin oblate inclusions, respectively. We further assume that interphase property is isotropic, with σ^{int} and ε^{int} as its conductivity and permittivity constants, respectively. Now, the effective properties of thinly-coated graphene filler, denoted by σ_i^{coat} and $\varepsilon_i^{\text{coat}}$, can be obtained in an explicit form by employing the Mori-Tanaka scheme (Weng, 1990):

$$\sigma_i^{\text{coat}} = \sigma^{\text{int}} \left[1 + \frac{(1-c_{\text{int}}) \left(\sigma_i - \sigma^{\text{int}} \right)}{c_{\text{int}} S_{ii} \left(\sigma_i - \sigma^{\text{int}} \right) + \sigma^{\text{int}}} \right],$$

$$\varepsilon_i^{\text{coat}} = \varepsilon^{\text{int}} \left[1 + \frac{(1-c_{\text{int}}) \left(\varepsilon_i - \varepsilon^{\text{int}} \right)}{c_{\text{int}} S_{ii} \left(\varepsilon_i - \varepsilon^{\text{int}} \right) + \varepsilon^{\text{int}}} \right], \tag{5.8}$$

where $i = 1$ or 3 $\left(\text{no sum over } i \right)$, and S_{ii} is the component of depolarization tensor evaluated with property of interphase. It should be emphasized that, in limiting case of diminishing interphase thickness, the "coated" inclusion and original inclusion share the same shape and subsequently the same **S**-tensor. As mentioned above, we take the electron tunneling activity and formation of microcapacitors as two statistical processes that depend on the volume concentration of graphene fillers, c_g^*. In establishing the corresponding probabilistic functions, we divide the evolution process of these phenomena into three stages. Initially, when small amount of fillers are incorporated into the matrix, i.e. at dilute concentration, the distance between fillers is large and there is a little possibility for tunneling activity and also for the formation of microcapacitors. With increase of graphene content in polymer matrix, the distance between neighboring fillers are continuously reduced, resulting in a network of

virtual microcapacitors to be slowly built up throughout the nanocomposite. However, near the percolation threshold the distance between the graphene fillers is greatly reduced. As a consequence, the capacitance of microcapacitors undergoes a sharp increase, and the tunneling activity also will become intense. Above the c_g^*, the distance between the fillers gets closer, so that even some fillers get in direct contact with each other due to their high aspect ratio. Accordingly, new microcapacitor structures with high virtual capacitance are formed by those graphene fillers which are not yet in contact with each other. Meanwhile, the electron tunneling still takes place between neighboring fillers and/or clusters. In view of that, after the percolation threshold the tunneling activity and microcapacitor effects will continue to be at high level. It was found that the Cauchy's probabilistic model to be particularly well suited to describe these complex phenomena in a continuum fashion. This model can be presented by a cumulative distribution function, *F*, as

$$F(c_g; c_g^*, \gamma) = \frac{1}{\pi}\arctan\left(\frac{c_g - c_g^*}{\gamma}\right) + \frac{1}{2}, \tag{5.9}$$

where γ is a scale parameter which denotes the rate of change for function *F* around $c_g = c_g^*$. For a schematic demonstration on the nature of Cauchy's distribution, it is plotted in Fig. 5.2(a) as a function of graphene volume concentration, for the given numerical values of $c_g^* = 0.05$ and $\gamma = 0.003$. As shown in this figure, function *F* shows a rapid increase as c_g passes through c_g^*. It is the overall spectrum of the cumulative function that can signify the added contributions to the interfacial conductivity and capacitance of fillers by the electron tunneling and formation of microcapacitors, respectively. In this light, with the Cauchy's

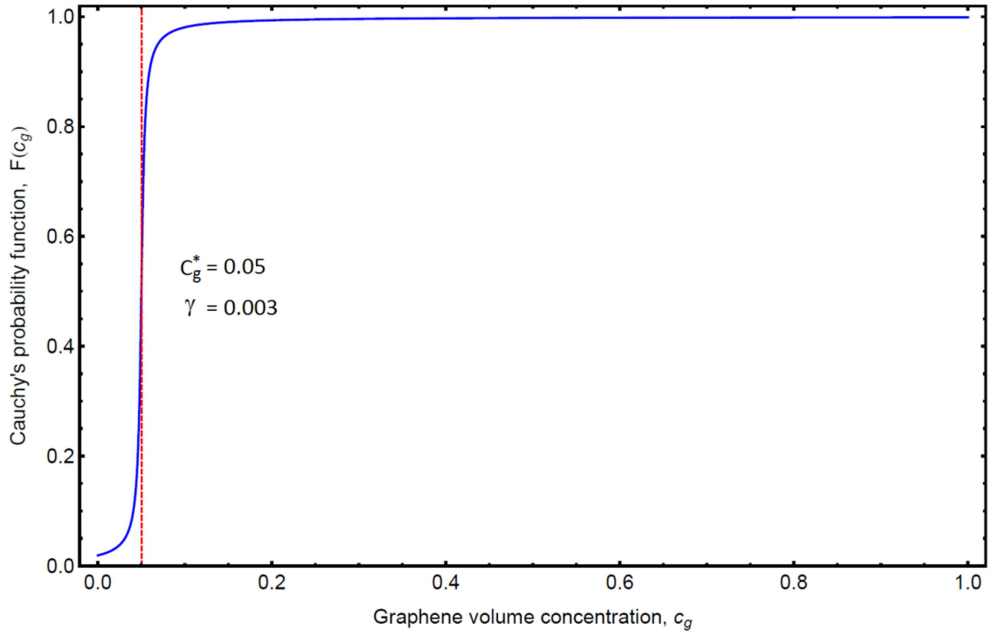

(a)

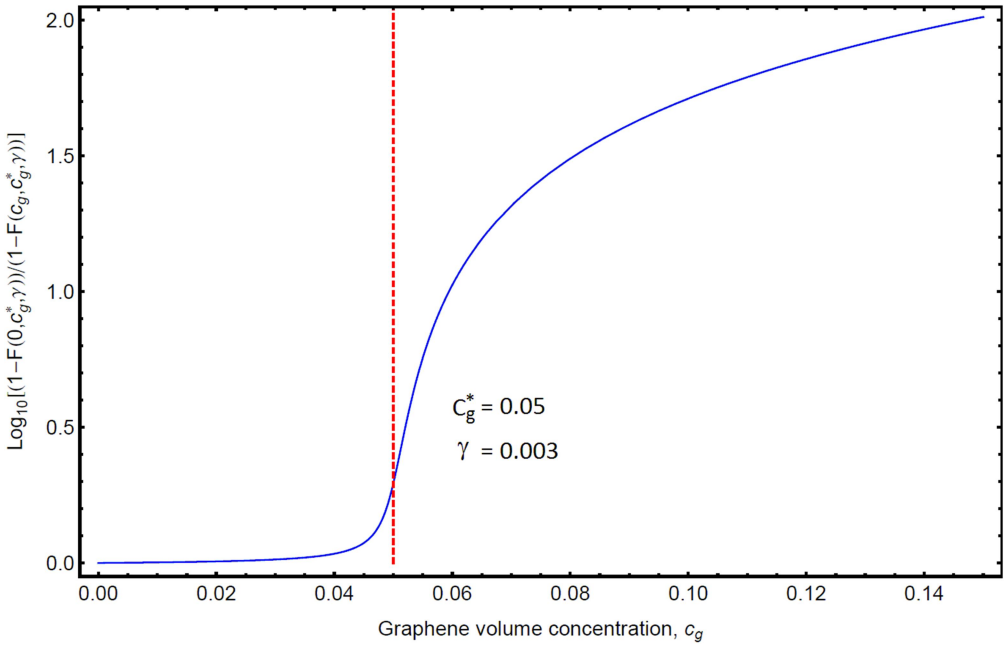

(b)

Fig. 5.2 (a) Cauchy's distribution function, (b) the effects of microcapacitor (or electron-tunneling) activities on the increase of interfacial permittivity (or conductivity), as filler concentration increases.

function the interfacial conductivity and permittivity in Eq. (5.8) can be set to depend on filler concentration, respectively as:

$$\sigma^{\text{int}} = \tilde{\sigma}^{\text{int}}\ [1 - F(0, c_g^*, \gamma_\sigma)] / [1 - F(c_g, c_g^*, \gamma_\sigma)],$$

$$\varepsilon^{\text{int}} = \tilde{\varepsilon}^{\text{int}}\ [1 - F(0, c_g^*, \gamma_\varepsilon)] / [1 - F(c_g, c_g^*, \gamma_\varepsilon)], \tag{5.10}$$

in which $\tilde{\sigma}^{\text{int}}$ and $\tilde{\varepsilon}^{\text{int}}$, respectively, are the interlayer conductivity and permittivity at $c_g = 0$. Eqs. (5.10) then play the role of electron tunneling and microcapacitor effects in our formulation. To see their implications more clearly, we plot functions $[1 - F(0, c_g^*, \gamma)] / [1 - F(c_g, c_g^*, \gamma)]$ in Fig. 5.2 (b), for $\gamma = 0.003$ and $c_g^* = 0.05$. In the end, upon substitution of expressions (5.10) into Eq. (5.8) one can obtain the modified conductivity and permittivity constants of a thinly-coated graphene filler, σ_i^{coat} and $\varepsilon_i^{\text{coat}}$, respectively. This coated graphene is then embedded into the original matrix to compute the effective properties of nanocomposite with the interfacial tunneling and polarization effects, by Eq. (5.6), where σ_i and ε_i are now replaced respectively by those of the thinly coated inclusion, σ_i^{coat} and $\varepsilon_i^{\text{coat}}$, given in Eq. (5.8). In this way, the effective conductivity and permittivity moduli of the graphene nanocomposites with an interface effect, σ_e and ε_e, can be obtained.

This completes our continuum-based formulation for determination of the effective properties of graphene/polymer composites in AC setting.

5.3. Numerical results and discussion

To put the applicability of developed theory in perspective, we consider a nanocomposite material made of the graphene nanoplatelets (GNPs) and Polyvinylidene fluoride (PVDF) matrix. The experimental data for AC conductivity and permittivity moduli of this GNP/PVDE nanocomposite have been given by He et al. (2009). The percolation threshold of $c_g^* = 0.0105$ was reported for the material. Employing the present model with the set of physical parameters listed in Table 5.1, the conductivity and permittivity constants of nanacomposite are calculated as a function of graphene volume concentration, c_g. The numerical calculation is implemented separately for three selected frequencies of f = 50, 1000 and 5000 Hz. For these frequencies, the calculated results along with the corresponding experimental data are plotted in Figs. 5.3, 5.4 and 5.5, respectively, in which the effective permittivity was normalized with respect to the vacuum permittivity, $\varepsilon_v = 8.85 \times 10^{-12}$ F/m. From all figures it is evident that our numerical results for a given frequency could successfully capture the quantitative behavior of relevant experimental data for both conductivity and permittivity constants. Overall, this demonstrates that the combination of effective-medium theory and the phenomenological modification of interlayer properties due to microcapacitor and tunneling activities gives rise to a complete theory for the graphene/polymer nanocomposites in AC electrical settings.

Table 5.1. Physical values used in the numerical calculation for effective AC conductivity and permittivity of GNP/PVDF nanocomposite

Properties	Numerical values		
Percolation threshold, c_g^*	0.0106		
Aspect ratio of GNPs, α	0.00607		
Thickness of GNPs, D (nm)	20		
Thickness ratio of interlayer, t/D	0.01		
In-plane conductivity of GNPs, σ_1 (S/m)	8.5×10^4		
Out-plane conductivity of GNPs, σ_3 (S/m)	85		
In-plane permittivity of GNPs, $\varepsilon_1/\varepsilon_v$	15		
Out-plane permittivity of GNPs, $\varepsilon_3/\varepsilon_v$	9		
AC frequencies, f (Hz)	50	1000	5000
Matrix conductivity, σ_0 (S/m)	1×10^{-9}	8×10^{-9}	35×10^{-9}
Permittivity of matrix, $\varepsilon_0/\varepsilon_v$	8	7	6
Interlayer conductivity, $\tilde{\sigma}^{int}$ (S/m)	0.4×10^{-5}	0.4×10^{-5}	0.4×10^{-5}
Interlayer conductivity, $\tilde{\varepsilon}^{int}/\varepsilon_v$	4080	0.25	0.0001
Electron-tunneling scale parameter, γ_σ	0.002	0.002	0.002
Microcapacitor scale parameter, γ_ε	1.2×10^{-11}	5.9×10^{-13}	6×10^{-15}

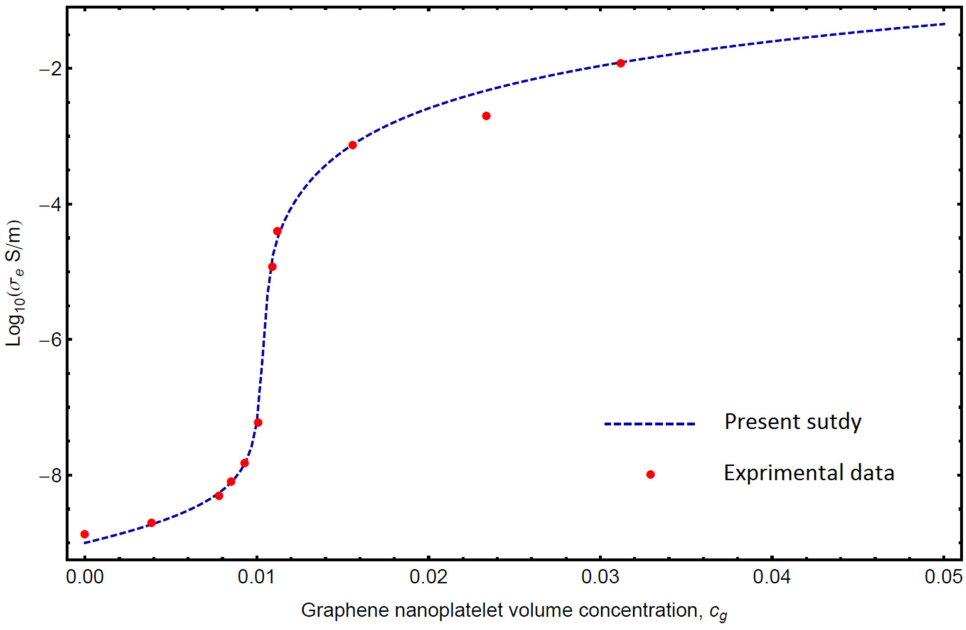

(a)

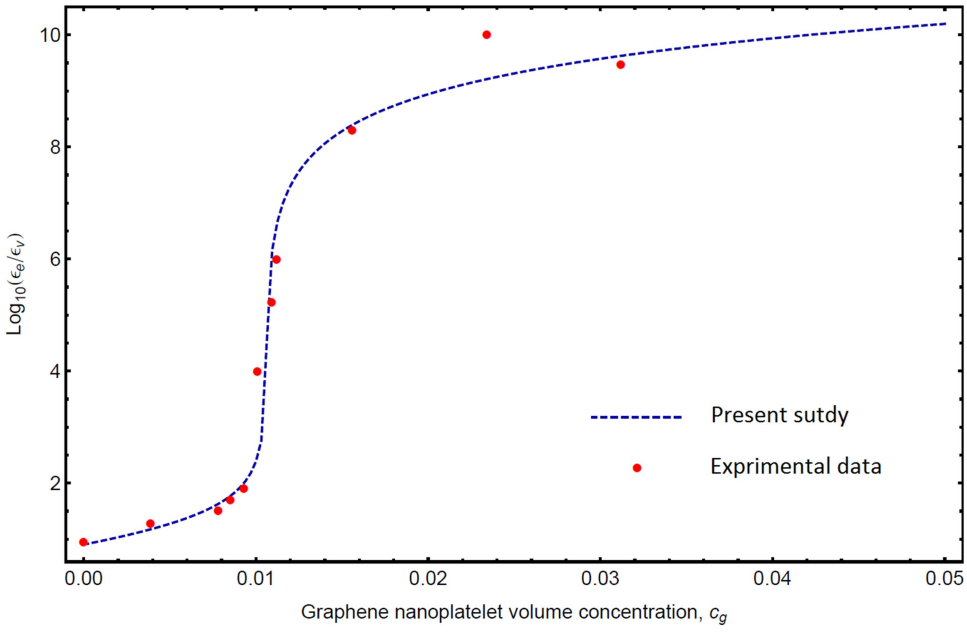

(b)

Fig. 5.3. Effective (a) conductivity and (b) permittivity of the graphene nanocomposite, predicted by present model for f = 50 Hz, along with experimental data of He et al. (2009).

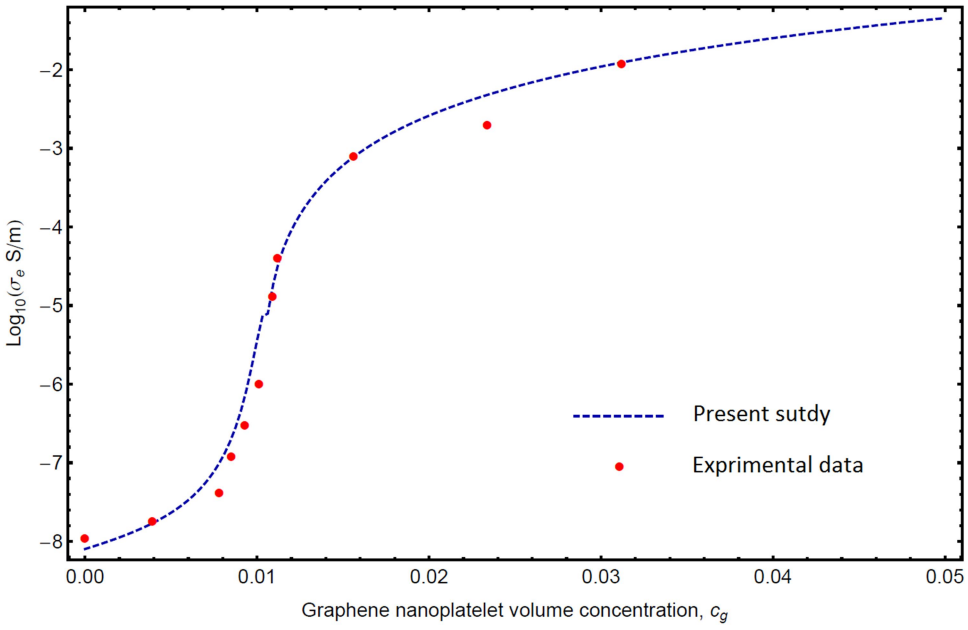

(a)

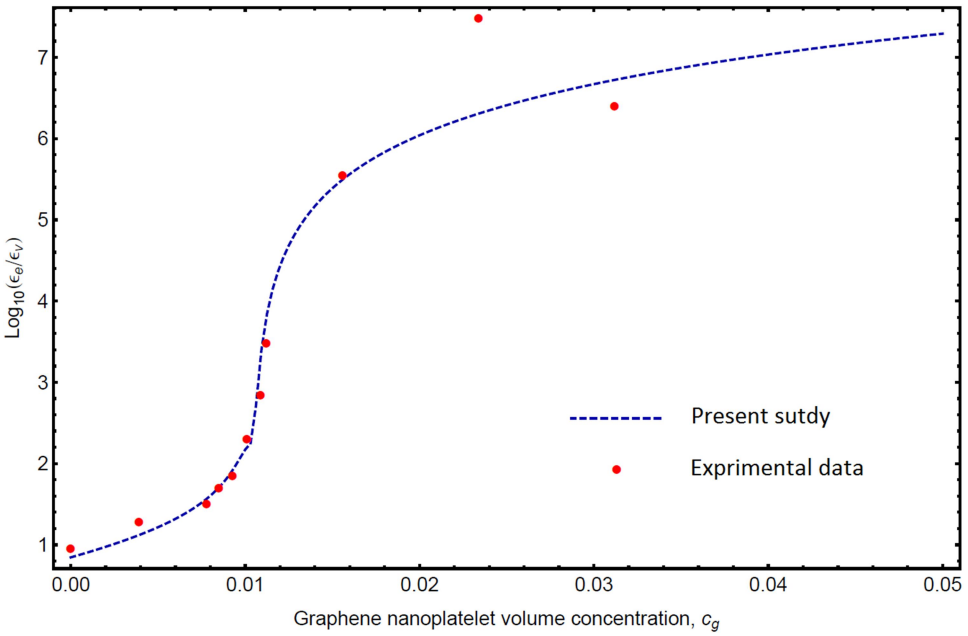

(b)

Fig. 5.4. Effective (a) conductivity and (b) permittivity of the graphene nanocomposite, predicted by present model for f = 1000 Hz, along with experimental data of He et al. (2009).

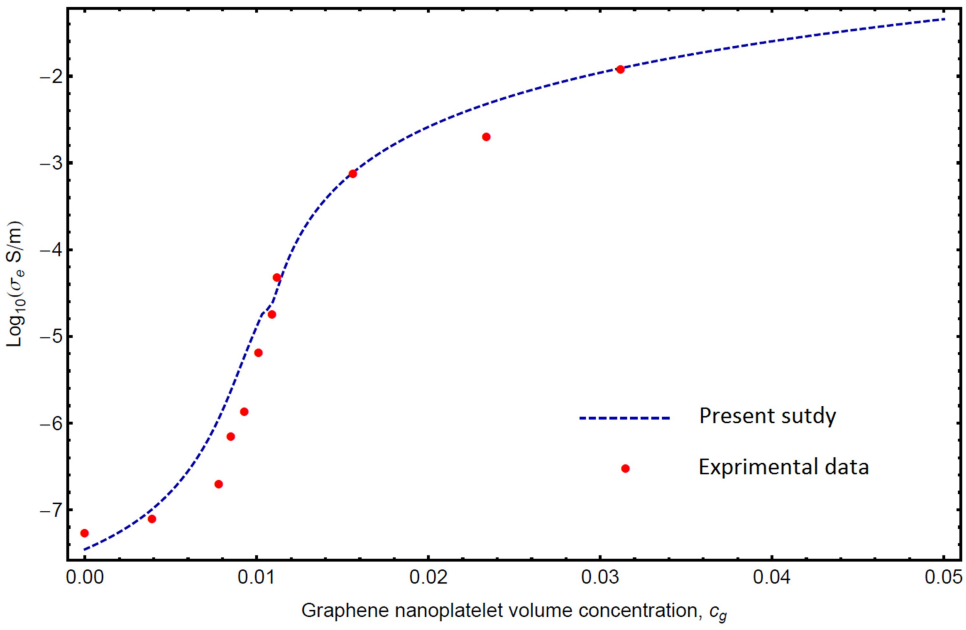

(a)

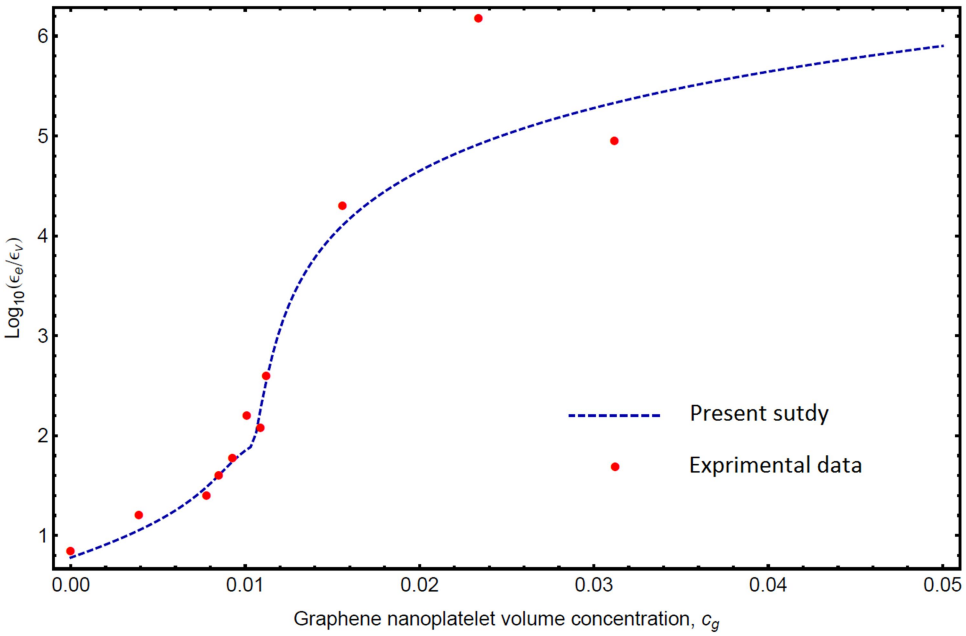

(b)

Fig. 5.5. Effective (a) conductivity and (b) permittivity of the graphene nanocomposite, predicted by present model for f = 5000 Hz, along with experimental data of He et al. (2009).

5.4. Concluding remarks

In this chapter, we formulated a homogenization scheme for determination of the effective AC electrical properties of graphene nanocomposites. The proposed theory embodies the most fundamental characteristics of the graphene nanocomposites, i.e. percolation threshold, and additional contribution of microcapacitor structures and electron-hoping phenomenon to interfacial properties. The outcome is a simple and yet useful model that has the necessary connection with the physics of electrical process in graphene nanocomposites, despite the corresponding formula involves only limited number of input parameters. The applicability of developed model was verified through consideration of experimental data for a real sample of nanocomposite at different loading frequencies. It was demonstrated that the proposed model can successfully recover the quantitative behavior of various data sets in AC electrical settings. The availability of such a robust model can be useful for the design and optimization of high performance materials, needed for new advanced applications, such as the electromagnetic shielding, high-energy-density capacitors and etc.

Chapter 6.

Future works

In the study of multiferroic composites, via a robust analytical solution we examined the scattered fields of a SH-wave induced by an eccentric multiferroic fiber. Through that investigation, the fiber ensemble was perfectly bonded to the surrounding piezoelectric or piezomagnetic matrix. However, it is well known that the interface in real composites is usually not perfect, and a weak interface can greatly affect the local microscopic fields as well as the overall macroscopic response of composite materials. In this regard, utilizing the methodology proposed in chapter 3 one may assess the effect of interface condition on the wave scattering phenomenon in the three-phase composites. This study will be of practical and theoretical interest, in that the forgoing studies on the dynamics of composite materials with imperfect interface have been sparse in literature.

In the study of graphene-based nanocomposite, we have shown that the imperfect interface plays a crucial role in the determination of the overall creep, stress relaxation and strain-rate sensitivity responses of graphene/polymer materials. Extending that investigation it is valuable to examine the interface effects on the storage and loss moduli of graphene/polymer composites under harmonic mechanical loadings. This issue is of particular importance for the long-term reliability of the graphene-based nanocomposites. The methodology proposed in chapter 4 also can be developed to uncover the effects of interface condition as well as other micromechanical parameters (e.g. the agglomeration phenomenon) on the overall elastoplastic response of graphene/metal nanocomposites.

Appendix

In order to carry out the integrations involved in Chapter 3, we adopt the following approach for the decomposition of the integration region into some subdomains. To do so, first let $I_{\Omega_1 \cup \Omega_2}$ denotes the integration over $\Omega_1 \cup \Omega_2$ in expressions (3.10). To calculate this integral, we introduce new circular regions Ψ^* and Ψ^{**} (Shodja et al., 2014), as:

$$\Psi^* = \left\{ \boldsymbol{x} : R_1 < |\boldsymbol{x}| < R_2 - \delta \right\},$$

$$\Psi^{**} = \left\{ \boldsymbol{x} : R_2 - \delta < |\boldsymbol{x}| < R_2 + \delta \right\},$$

where point $\boldsymbol{x}$ associated with the polar coordinates $(r,\ \theta)$ is the observation point. On the other hand, in the light of Eqs. (3.11) and (3.12) point $\boldsymbol{x}'$ pertinent to (r', θ') is the location of the applied unit impulse load. Associated to each point $\boldsymbol{x}'$ there is a point on the boundary of $\Omega_1 \cup \Omega_2$ with position vector $\mathbf{R}(\theta')$, in such a way that

$$\left|\mathbf{R}(\theta')\right| = -\delta \cos(\theta') + \sqrt{\left(\delta \cos\theta'\right)^2 - \delta^2 + {R_2}^2}.$$

According to the location of observation point $\boldsymbol{x}$ in each of regions Ω_1, Ψ^* and Ψ^{**} the integration $I_{\Omega_1 \cup \Omega_2}$ then can be evaluated conveniently as follows:

$$I_{\Omega_1 \cup \Omega_2} = \int_0^{2\pi} \int_0^{r} \ldots dr' d\theta' + \int_0^{2\pi} \int_r^{R_1} \ldots dr' d\theta' + \int_0^{2\pi} \int_{R_1}^{|\mathbf{R}(\theta')|} \ldots dr' d\theta', \quad \boldsymbol{x} \in \Omega_1,$$

$$I_{\Omega_1 \cup \Omega_2} = \int_0^{2\pi} \int_0^{R_1} \ldots dr' d\theta' + \int_0^{2\pi} \int_{R_1}^{r} \ldots dr' d\theta' + \int_0^{2\pi} \int_r^{|\mathbf{R}(\theta')|} \ldots dr' d\theta', \quad \boldsymbol{x} \in \Psi^*,$$

$$I_{\Omega_1 \cup \Omega_2} = \int_0^{2\pi} \int_0^{R_1} \ldots dr' d\theta' + \int_0^{2\pi} \int_{R_1}^{r} \ldots dr' d\theta' - \int_0^{2\pi} \int_{R_1}^{|\mathbf{R}(\theta')|} \ldots dr' d\theta' - \int_{-\boldsymbol{\theta}(r)}^{\boldsymbol{\theta}(r)} \int_{|\mathbf{R}(\theta')|}^{r} \ldots dr' d\theta', \quad \boldsymbol{x} \in \Psi^{**},$$

in which $\boldsymbol{\theta}(r) = \cos^{-1}\left[\dfrac{{R_2}^2 - \delta^2 - r^2}{2\delta r}\right]$. On the other hand, when the point $\boldsymbol{x}$ is outside mentioned regions, the integrations simply become:

$$I_{\Omega_1 \cup \Omega_2} = \int_0^{2\pi} \int_0^{|\mathbf{R}(\theta')|} \ldots \, dr' d\theta', \qquad \boldsymbol{x} \in D - \left\{ \Omega_1 \bigcup \Psi^* \bigcup \Psi^{**} \right\}.$$

In light of this integration process, the functions $U_n^{(j)}$, $W_n^{(j)}$, $V_n^{(j)}$ and $Z^{(j)}(r)$ associated with Eqs. (3.18) and (3.19) can be evaluated in terms of the unknown functions $f_n^{(j)}(r)$ and $g_n^{(j)}(r)$ (n = 0, 1, 2, … ; j = 1, 2, 3, 4, 5, 6, 7). Accordingly, the expression of these functions for the field point, $\boldsymbol{x}$ within each of the regions Ω_1, Ψ^* and Ψ^{**} are the following forms:

$$\left\{ U_n^{(j)};\ W_n^{(j)} \right\} = \left\{ -\frac{i\kappa}{4\left(\kappa c + e^2\right)};\ -\frac{i\mu}{4\left(\mu c + q^2\right)} \right\} \times$$
$$\left[\pi H_n^{(1)}(\lambda r) \int_0^r f_n^{(j)}(r') J_n(\lambda r') r' dr' \right.$$
$$+ \pi J_n(\lambda r) \int_0^{R_1} f_n^{(j)}(r') H_n^{(1)}(\lambda r') r' dr'$$
$$\left. + a_n J_n(\lambda r) \int_0^{\pi} \int_{R_1}^{|\mathbf{R}(\theta')|} F_n^{(j)}(r', \theta') H_n^{(1)}(\lambda r') r' \, dr' d\theta' \right], \quad \boldsymbol{x} \in \Omega_1,$$

$$\left\{ U_n^{(j)};\ W_n^{(j)} \right\} = \left\{ -\frac{i\kappa}{4\left(\kappa c + e^2\right)};\ -\frac{i\mu}{4\left(\mu c + q^2\right)} \right\} \times$$
$$\left[\pi H_n^{(1)}(\lambda r) \int_0^{R_1} f_n^{(j)}(r') J_n(\lambda r') r' dr' \right.$$
$$+ \pi H_n^{(1)}(\lambda r) \int_{R_1}^r g_n^{(j)}(r') J_n(\lambda r') r' dr'$$
$$\left. + a_n J_n(\lambda r) \int_0^{\pi} \int_r^{|\mathbf{R}(\theta')|} F_n^{(j)}(r', \theta') H_n^{(1)}(\lambda r') r' \, dr' d\theta' \right], \quad \boldsymbol{x} \in \Psi^*,$$

$$\left\{ U_n^{(j)};\ W_n^{(j)} \right\} = \left\{ -\frac{i\kappa}{4\left(\kappa c + e^2\right)};\ -\frac{i\mu}{4\left(\mu c + q^2\right)} \right\} \times$$
$$\left[\pi H_n^{(1)}(\lambda r) \int_0^{R_1} f_n^{(j)}(r') J_n(\lambda r') r' dr' \right.$$
$$+ \pi H_n^{(1)}(\lambda r) \int_{R_1}^r g_n^{(j)}(r') J_n(\lambda r') r' dr'$$
$$+ a_n J_n(\lambda r) \int_0^{\pi} \int_r^{|\mathbf{R}(\theta')|} F_n^{(j)}(r', \theta') H_n^{(1)}(\lambda r') r' \, dr' d\theta'$$
$$- a_n J_n(\lambda r) \int_0^{\boldsymbol{\theta}(r)} \int_r^{|\mathbf{R}(\theta')|} F_n^{(j)}(r', \theta') H_n^{(1)}(\lambda r') r' \, dr' d\theta'$$
$$\left. + a_n H_n^{(1)}(\lambda r) \int_0^{\boldsymbol{\theta}(r)} \int_r^{|\mathbf{R}(\theta')|} F_n^{(j)}(r', \theta') J_n(\lambda r') r' \, dr' d\theta' \right], \quad \boldsymbol{x} \in \Psi^{**},$$

$$V_n^{(j)} = \frac{r^{-n}}{4n}\int_0^r (r')^{n+1} f_n^{(j)}(r')\,dr' + \frac{r^n}{4n}\int_r^{R_1} (r')^{-n+1} f_n^{(j)}(r')\,dr' + \frac{r^n}{2\pi n}\int_0^{\pi}\int_{R_1}^{|\mathbf{R}(\theta')|} (r')^{-n+1} F_n^{(j)}(r',\theta')\,r'\,dr'd\theta', \qquad \boldsymbol{x}\in\Omega_1,$$

$$V_n^{(j)} = \frac{r^{-n}}{4n}\int_0^{R_1} (r')^{n+1} f_n^{(j)}(r')\,dr' + \frac{r^{-n}}{4n}\int_r^{R_1} (r')^{n+1} g_n^{(j)}(r')\,dr' + \frac{r^n}{2\pi n}\int_0^{\pi}\int_r^{|\mathbf{R}(\theta')|} (r')^{-n} F_n^{(j)}(r',\theta')\,r'\,dr'd\theta', \qquad \boldsymbol{x}\in\Psi^*,$$

$$V_n^{(j)} = \frac{r^{-n}}{4n}\int_0^{R_1} (r')^{n+1} f_n^{(j)}(r')\,dr' + \frac{r^{-n}}{4n}\int_{R_1}^{r} (r')^{n+1} g_n^{(j)}(r')\,dr' + \frac{r^n}{2\pi n}\int_0^{\pi}\int_r^{|\mathbf{R}(\theta')|} (r')^{-n+1} F_n^{(j)}(r',\theta')\,dr'd\theta' - \frac{r^{-n}}{2\pi n}\int_0^{\boldsymbol{\theta}(r)}\int_r^{|\mathbf{R}(\theta')|} (r')^{n+1} F_n^{(j)}(r',\theta')\,dr'd\theta' - \frac{r^{-n}}{2\pi n}\int_0^{\boldsymbol{\theta}(r)}\int_r^{|\mathbf{R}(\theta')|} (r')^{-n+1} F_n^{(j)}(r',\theta')\,dr'd\theta', \qquad \boldsymbol{x}\in\Psi^{**},$$

$$Z^{(j)}(r) = \frac{1}{r}\int_0^r f_0^{(j)}(r')\,r'\,dr', \qquad \boldsymbol{x}\in\Omega_1,$$

$$Z^{(j)}(r) = \frac{1}{r}\left\{\int_0^{R_1} f_0^{(j)}(r')\,r'\,dr' + \int_{R_1}^r g_0^{(j)}(r')\,r'\,dr'\right\}, \qquad \boldsymbol{x}\in\Psi^*,$$

$$Z^{(j)}(r) = \frac{1}{r}\left\{\int_0^{R_1} f_0^{(j)}(r')\,r'\,dr' + \int_{R_1}^r g_0^{(j)}(r')\,r'\,dr' - \frac{1}{\pi}\int_0^{\boldsymbol{\theta}(r)}\int_r^{|\mathbf{R}(\theta')|} F_0^{(j)}(r',\theta')\,r'\,dr'd\theta'\right\}, \quad \boldsymbol{x}\in\Psi^{**},$$

In these expressions, function $F_n^{(j)}(r',\theta')$ is

$$F_n^{(j)}(r',\theta') = \begin{cases} \cos(n\theta')\sum_{m=0}^{\infty} g_m^{(j)}(r')\cos(m\theta'), & j = 1,3,4,6, \\ \sin(n\theta')\sum_{m=0}^{\infty} g_m^{(j)}(r')\sin(m\theta'), & j = 2,5,7. \end{cases}$$

Likewise, the expression for the functions $T^{(j)}(r)$ (j = 4, 6) and $\Gamma_n^{(j)}(r)$ (j = 4, 5, 6, 7) in Eqs. (3.20) and (3.22), and coefficients $\xi_n^{(j)}(r)$ and $\eta_n^{(j)}(r)$ (n = 0, 1, 2, … ; j = 1, 2, 3, 4, 5, 6, 7) in Eqs. (3.21) and (3.23) can be obtained, respectively, as:

$$T^{(j)}(r) = \frac{1}{r}\left[\int_0^{R_1} f_0^{(j)}(r')\,r'\,dr' + \frac{1}{\pi}\int_0^{\pi}\int_{R_1}^{|\mathbf{R}(\theta')|} F_0^{(j)}(r',\theta')\,r'\,dr'd\theta'\right],$$

$$\Gamma^{(j)}(r)=\frac{1}{2}\int_0^{R_1}(r')^{n+1}\,f_n^{(j)}(r')\,dr'+\frac{2}{\pi}\int_0^{\pi}\int_{R_1}^{|\mathbf{R}(\theta')|}(r')^{n+1}F_n^{(j)}(r',\theta')\,dr'd\theta',$$

$$\left\{\xi_n^{(j)};\ \eta_n^{(j)}\right\}=\left\{-\frac{i\kappa}{4\left(\kappa c+e^2\right)};\ -\frac{i\mu}{4\left(\mu c+q^2\right)}\right\}\times\left[\pi\int_0^{R_1}f_n^{(j)}(r')J_n(\lambda r')r'\,dr'\right.$$
$$\left.+a_n\int_0^{\pi}\int_0^{|\mathbf{R}(\theta')|}F_n^{(j)}(r',\theta')J_n(\lambda r')r'\,dr'd\theta'\right].$$

References

Aboudi, J. (2001). Micromechanical analysis of fully coupled electro–magneto–thermo-elastic multiphase composites. *Smart Materials and Structures*, **10**, 867–877.

Alshits, V. I., Darinskii, A. N., & Lothe, J. (1992). On the existence of surface waves with piezoelectric and piezomagnetic properties. *Wave Motion*, **16**, 265-283.

Ansari, S., & Giannelis, E. P. (2009). Functionalized graphene sheet poly(vinylidene fluoride) conductive nanocomposites. *J. Polym. Sci. Part B Polym. Phys.*, **47**, 888-897.

Bai, H., Xu, Y., Zhao, L., Li, C., & Shi, G. (2009). Non-covalent functionalization of graphene sheets by sulfonated polyaniline. *Chem. Commun.*, **13**, 1667-1669.

Balandin, A. A., Ghosh, S., Bao, W., Calizo, I., Teweldebrhan, D., Miao, F., & Lau, C. N. (2008). Superior thermal conductivity of single-layer graphene. *Nano Lett.*, **8** (3), 902-907.

Balberg, I., Binenbaum, N., & Wagner, N. (1984). Percolation Thresholds in the Three-Dimensional Sticks System. *Phys. Rev. Lett.,* **52**, 1465.

Bao, W. S., Meguid, S. A., Zhu, Z. H., Pan, Y., & Weng, G. J. (2012). A novel approach to predict the electrical conductivity of multifunctional nanocomposites. *Mech. Mater.*, **46**, 129–138.

Barai, P., & Weng, G. J. (2011). A theory of plasticity for carbon nanotube reinforced composites. *Int. J. Plast.*, **27**, 539–559.

Barnett, D. M., & Lothe, J. (1975). Dislocations and line charges in anisotropic piezoelectric insulators. Phys. *Status Solidi. B*, **67**, 105–111.

Benveniste, Y. (1995). Magnetoelectric effect in fibrous composites with piezoelectric and piezomagnetic phases. *Phys. Rev. B*, **51**, 16424–16427.

Benveniste, Y. (1985). The effective mechanical behavior of composite materials with imperfect contact between the constituents. *Mech. Mater.*, **4**, 197–208.

Benveniste, Y. (1987). A new approach to the application of Mori–Tanaka's theory in composite materials. *Mech. Mater.*, **6**, 147–157.

Bera, S., Arnold, A., Evers, F., Narayanan, R., & Wölfle, P. (2010). Elastic properties of graphene flakes: Boundary effects and lattice vibrations. *Phys. Rev. B*, **82**, 195445.

Berhan, L., & Sastry, A. M. (2007). Modeling percolation in high-aspect-ratio fiber systems. I. Soft-core versus hard-core models. *Phys Rev E.*, **75**, 1-8.

Cadelano, E., Palla, P. L., Giordano, S., & Colombo, L. (2010). Elastic properties of hydrogenated graphene. *Phys. Rev. B*., **82**, 235414.

Camacho-Montes, H., Sabina, F.J., Bravo-Castillero, J., Guinovart-Díaz, R., & Rodríguez-Ramos, R. (2009). Magnetoelectric coupling and cross-property connections in a square array of a binary composite. *Int. J. Eng. Sci.,* **47**, 294–312.

Chen, J., Pan, E., & Chen, H. (2007). Wave propagation in magneto-electro-elastic multilayered plates. *International Journal of Solids and Structures*, **44**, 1073–1085.

Chen, P., & Shen, Y. (2007). Propagation of axial shear magneto-electro-elastic waves in piezoelectric-piezomagnetic composites with randomly distributed cylindrical inhomogeneities. *International Journal of Solids and Structures*, **44**, 1511–1532.

Chen, T., Weng, G. J., & Liu, W. C. (2005). Effect of Kapitza contact and consideration of tube-end transport on the effective conductivity in nanotube-based composites. *J. Appl. Phys.*, **97**, 104312.

Cui, L. L., Lu, X. F., Chao, D. M., Liu, H. T., Li, Y. X., & Wang, C. (2011). Graphene composite materials with high dielectric permittivity via an in situ reduction method. *Phys. Status Solidi*, **208**, 459-461.

Dang, Z. M., Yuan, J. K., Zha, J. W., Zhou, T., Li, S. T., & Hu, G. H. (2012). Fundamentals, processes and applications of high-permittivity polymer–matrix composites. *Progress in Materials Science*, **57**, 660-723.

Deng, F., & Zheng, Q. S. (2008). An analytical model of effective electrical conductivity of carbon nanotube composites. *Appl. Phys. Lett.,* **92**, 071902.

Dinzart, F., & Sabar, H. (2011). Magneto-electro-elastic coated inclusion problem and its application to magnetic-piezoelectric composite materials. Int. J. Solids Struct., **48**, 2393–2401.

Du, J. K., Shen, Y. P., Ye, D. Y., & Yue, F. R. (2004). Scattering of anti-plane shear waves at a partially debonded magneto-electro-elastic circular cylindrical inhomogeneity. International Journal of Engineering Science, **42**, 887–913.

Eda, G., & Chhowalla, M. (2009). Graphene composite thin films for electronics, *Nano Lett.*, **9**, 814-818.

Eringen, A. C., & Suhubi, E. S. (1975). Elastodynamics, vol. II. Academic Press, New York, San Francisco, London.

Eshelby, J. D. (1957). The determination of the elastic field of an ellipsoidal inclusion and related problems. Proc. R. Soc. A. **241**, 376–396.

Espinosa-Almeyda, Y., López-Realpozo, J. C., Rodríguez-Ramos, R., Bravo-Castillero, J., Guinovart-Díaz, R., Camacho-Montes, H., & Sabina, F. J. (2011). Effects of interface contacts on the magneto-electro-elastic coupling for fiber reinforced. Int. J. Solids Struct., **48**, 1525–1533.

Espinosa-Almeyda, Y., Rodríguez-Ramos, R., Guinovart-Díaz, R., Bravo-Castillero, J., López-Realpozo, J. C., Camacho-Montes, H., Sabina, F. J., & Lebon, F. (2014). Antiplane magneto-electro-elastic effective properties of three-phase fiber composites. Int. J. Solids Struct., **51**, 3508–3521.

Fan, P., Wang, L., Yang, J., Chen, F., & Zhong, M. (2012). Graphene/poly(vinylidene fluoride) composites with high dielectric constant and low percolation threshold. *Nanotechnology*, **23**, 365702.

Fan, Z., Gong, F., Nguyen, S. T., & Duong, H. M. (2015). Advanced multifunctional graphene aerogel – Poly (methyl methacrylate) composites: Experiments and modeling. *Carbon*, **81**, 396-404.

Fisher, F. T., & Brinson, L. C. (2001). Viscoelastic interphases in polymer-matrix composites: theoretical models and finite-element analysis. *Compos. Sci. Technol.*, **61**, 731–748.

Fu, L. S., & Mura, T. (1983). The determination of elastodynamic fields of an ellipsoidal inhomogeneity. *ASME J. Appl. Mech.,* **50**, 390–396.

Gao, W., & Huang, R., (2014). Thermomechanics of monolayer graphene: Rippling, thermal expansion and elasticity. *Journal of the Mechanics and Physics of Solids*, **66**, 42–58.

Gardea, F., & Lagoudas, D. C. (2014). Characterization of electrical and thermal properties of carbon nanotube/epoxy composites. *Composites Part B.,* **6**, 611.

Gómez, H., Ram, M. K., Alvi, F., Villalba, P., Stefanakos, E. L., & Kumar, A. (2011). Graphene-conducting polymer nanocomposite as novel electrode for supercapacitors. *Journal of Power Sources*, **196**, 4102-4108

Guinovart-Díaz, R., Rodríguez-Ramos, R., Bravo-Castillero, J., Sabina, F. J., Monsivais Galindo, G., & Wang, Y. S. (2013). Plane magneto-electro-elastic moduli of fiber composites with interphase. Mech. Adv. Mater. Struct., **20**, 552–563.

Hashemi R., Spring, D. W., & Paulino, G. H. (2015). On small deformation interfacial debonding in composite materials containing multi-coated particles. Journal of Composite Materials, **49** (15), 3439-3455.

Hashemi, R., Weng, G. J., Kargarnovin, M. H., & Shodja H. M. (2010). Piezoelectric composites with periodic multi-coated inhomogeneities. *International Journal of Solids and Structures*, **47**(21), 2893-2904.

Hashin, Z. (1965). Viscoelastic behavior of heterogeneous media. *J. Appl. Mech.*, **32**, 630–636.

Hashin, Z. (1990). Thermoelastic properties of fiber composites with imperfect interface. *Mech. Mater.*, **8**, 333–348.

He, F., Lau, S., Chan, H. L., & Fan, J. (2009). High Dielectric Permittivity and Low Percolation Threshold in Nanocomposites Based on Poly(vinylidene fluoride) and Exfoliated Graphite Nanoplates. *Adv. Mater.*, **21**, 710–715.

Hicks, J., Behnam, A., & Ural, A. (2009). A computational study of tunneling-percolation electrical transport in graphene nanocomposites. *Applied Physics Letters*, **95**, 213103.

Hill, R., (1964), Theory of mechanical properties of fiber-strengthened materials: I. Elastic behavior. *J. Mech. Phys. Solids*, **12**, 199–212.

Huang, J. H. (1998). Analytical predictions for the magnetoelectric coupling in piezomagnetic materials reinforced by piezoelectric ellipsoidal inclusions. *Physical Review B*, **58** (1), 12–15.

Huang, J. H., & Kuo, W. S. (1997). The analysis of piezoelectric/piezomagnetic composite materials containing ellipsoidal inclusions. *J. Appl. Phys.*, **81**, 1378–1386.

Huang, L., Li, C., & Gaoquan., S. (2014). High-performance and flexible electrochemical capacitors based on graphene/polymer composite films. *J. Mater. Chem.*, A, **2**, 968-974.

Huang, Y., Li, X. F., & Lee, K. Y. (2009). Interfacial shear horizontal (SH) waves propagating in a two-phase piezoelectric/piezomagnetic structure with an imperfect interface. *Philosophical Magazine Letters*, **89**, 95–103.

Kargarnovin, M. H., Shodja, H. M., & Hashemi, R. (2011). A general treatment of piezoelectric double-inhomogeneities and their associated interaction problems, *Acta Mechanica*, **220**, 167-182.

Kelly, B.T. (1981). *Physics of Graphite*, London: Applied Science.

Kim, J. Y., Lee, W. H., Suk, J. W., Potts, J. R., Chou, H., Kholmanov, I. N., et al. (2013). Chlorination of reduced graphene oxide enhances the dielectric constant of reduced graphene oxide/polymer composites. *Adv. Mater.*, **25**, 2308-2313.

Kim, S. Y., Noh, Y. J., & Yu, J. (2015). Prediction and experimental validation of electrical percolation by applying a modified micromechanics model considering multiple heterogeneous inclusions. *Composites Science and Technology*, **106**, 156-162.

King J. A., Klimek, D. R., Miskioglu, I., & Odegard, G. M. (2015). Mechanical properties of graphene nanoplatelet/epoxy composites. *Journal of Composite Materials*., **49**, 6, 659-668.

Kuilla, T., Bhadra, S., Yao, D., Kim, N. H., Bose, S., & Lee, J. H. (2010). Recent advances in graphene based polymer composites. *Progress in Polymer Science*, **35**, 1350-1375.

Kuo, H. Y. (2011). Multicoated elliptic fibrous composites of piezoelectric and piezomagnetic phases. *Int. J. Eng. Sci.*, **49**, 561–575.

Kuo, H. Y. (2013). Effective property of multiferroic composites with imperfect interfaces. *Smart Materials and Structures*, **22**, 105005.

Kuo, H. Y., & Pan, E. (2011). Effective magnetoelectric effect in multicoated circular fibrous multiferroic composites. *J. Appl. Phys.*, **109**, 104901.

Kuo, H. Y., & Peng, C. Y. (2013). Magnetoelectricity in coated fibrous composites of piezoelectric and piezomagnetic phases. *International Journal of Engineering Science*, **62**, 70–83.

Kuo, H. Y., & Yu, S. H. (2014). Effect of the imperfect interface on the scattering of SH wave in a piezoelectric cylinder in a piezomagnetic matrix. *International Journal of Engineering Science*, **85**, 186–202.

Lawes, G., & Srinivasan, G. (2011). Introduction to magnetoelectric coupling and multiferroic films. *Journal of Physics D: Applied Physics*, **44**, 243001.

Lee, C. G., Wei, X. D., Kysar, J. W., & Hone, J. (2008). Measurement of the elastic properties and intrinsic strength of monolayer graphene. *Science*, **321**, 385-388.

Lee, J., Boyd IV, J. G., & Lagoudas, D. C. (2005). Effective properties of three phase electro-magneto-elastic composites. *Int. J. Eng. Sci.*, **43**, 790–825.

Levin, V. M., Michelitsch, T. M., & Gao, H. (2002). Propagation of electroacoustic waves in the transversely isotropic piezoelectric medium reinforced by randomly distributed cylindrical inhomogeneities. *International Journal of Solids and Structures*, **39**, 5013–5051.

Li, J. Y. (2000). Magnetoelectroelastic multi-inclusion and inhomogeneity problems and their applications in composite materials. *Int. J. Eng. Sci.*, **38**, 1993–2011.

Li, J. Y., & Dunn, M. L. (1998). Micromechanics of magnetoelectroelastic composite materials: average fields and effective behavior. *J. Intell. Mater. Syst. Struct.*, **9**, 404–416.

Li, J., & OStling, M. (2013). Percolation thresholds of two-dimensional continuum systems of rectangles. *Physical Review E*, **88**, 012101.

Li, J., & Weng, G. J. (2013). A micromechanical approach to the stress–strain relations, strain-rate sensitivity and activation volume of nanocrystalline materials. *International Journal of Mechanics and Materials in Design*, **9**, 141-152.

Liang, J., Wang, Y., Huang, Y., Ma, Y., Liu, Z., Cai, J., et al. (2009). Electromagnetic interference shielding of graphene/epoxy composites. *Carbon*, **47**, 922-5.

Liu, G., Nan, C. W., Cai, N., & Lin, Y. (2004). Calculations of giant magnetoelectric effect in multiferroic composites of rare-earth-iron alloys and PZT by finite element method. *Int. J. Solids Struct.*, **41**, 4423–4434.

Liu, J. X., Fang, D. N., Wei, W. Y., & Zhao, X. F. (2008). Love waves in layered piezoelectric/piezomagnetic structures. *Journal of Sound and Vibration*, **315**, 146–156.

Liu, J., Fang, D., & Liu, X. (2007). A shear horizontal surface wave in magnetoelectric materials. *IEEE Transactions on Ultrasonics Ferroelectrics and Frequency Control*, **54**, 1287–1289.

Liu, J., Tian, G., Qi, S., Wu, Z., & Wu, D. (2014). Enhanced dielectricpermittivity of a flexiblethree-phase polyimide–graphene–BaTiO3 composite material. *Materials Letters,* **124**, 117-119.

Liu, L. P., & Kuo H. Y. (2012). Closed-form solutions to the effective properties of fibrous magnetoelectric composites and their applications. *International Journal of Solids and Structures*, **49** (22), 3055-3062.

Liu, W., & Kriz, R. D. (1996). Axial shear waves in fiber-reinforced composites multiple interfacial layers between fiber core and matrix. *Mech. Mater.*, **31**, 117–129.

Lv, S., Ma, Y., Qiu, C., Sun, T., Liu, J., & Zhou, Q. (2013). Mechanical properties and microstructure of a graphene oxide–cement composite. *Construction and Building Materials*, **49**, 121-127.

Ma, J. M., Hu, J., Li, Z., & Nan, C. W. (2011). Recent progress in multiferroic magnetoelectric composites: From bulk to thin films. *Advanced Materials*, **23**, 1062–1087.

Meguid, S. A., Wernik, J. M., & Cheng, Z. Q. (2010). Atomic-based continuum representation of the effective properties of nano-reinforced epoxy. *Int. J. Solid Struct.,* **47**, 1723–1736.

Michel, K. H., & Verberck, B. (2008). Theory of the elastic constants of graphite and graphene. *Phys. Status Solidi B*, **245**, 2177-2180.

Michelitsch, T. M., Gao, H., & Levin, V. M. (2003). Dynamic Eshelby tensor and potential inclusion. *Proc. R. Soc. London, Ser. A* **459**, 863–890.

Mikata, Y., & Nemat-Nasser, S. (1991). Interaction of a harmonic wave with a dynamically transforming inhomogeneity. *J. Appl. Phys.* **70**, 2071–2078.

Milgrom, M., & Shtrikman, S. (1989). Linear response of two-phase composites with cross moduli: Exact universal relations. *Physical Review A*, **40**, 1568–1575.

Mironov, V. S., Kim, J. K., Park, M., Lim, S., & Cho, W. K. (2007). Comparison of electrical conductivity data obtained by four-electrode and four-point probe methods for graphite-based polymer composites. *Polymer Test*, **26**, 547-555.

Mori, T., & Tanaka, K. (1973). Average stress in the matrix and average elastic energy of materials with misfitting inclusions. *Acta Metall*. **21**, 571–574.

Mrozek, R. A., Cole, P. J., Mondy, L. A., Rao, R. R., Bieg, L. F., & Lenhar, J. L. (2010). Highly conductive, melt processable polymer composites based on nickel and low melting eutectic metal. *Polymer*, **51**, 2954-2958.

Nan, C. W. (1994). Magnetoelectric effect in composites of piezoelectric and piezomagnetic phases. *Phys. Rev., B.* **50**, 6082–6088.

Nan, C. W., Bichurin, M. I., Dong, S., Viehland, D., & Srinivasan, G. (2008). Multiferroic magnetoelectric composites: Historical perspective, status, and future directions. *Journal of Applied Physics*, **103**, 031101.

Nan, C. W., Liu, G., Lin, Y. H., & Li, M. (2004). Interface effect on thermal conductivity of carbon nanotube composites. *Appl. Phys. Lett.*, **85**, 3549–3551.

Novoselov, K. S., Geim, A. K., Morozov, S. V., Jiang, D., Zhang, Y., Dubonos, S. V., Grigorieva, I. V., & Firsov, A. A., (2004). Electric field effect in atomically thin carbon films. *Science*, **306**, 666-669.

Orlita, M., Faugeras, C., Plochocka, P., Neugebauer, P., Martinez, G., Maude, D. K., Barra, A. L., Sprinkle, M., Berger, C., de Heer, W. A., & Potemski M. (2008). Approaching the dirac point in high mobility multilayer epitaxial graphene. *Phys. Rev. Lett.*, **101**, 26, 267601.

Pan, Y., Weng, G. J., Meguid, S. A., Bao, W. S., Zhu, Z. H., & Hamouda, A. M. (2013). Interface effects on the viscoelastic characteristics of carbon nanotube polymer matrix composites. *Mechanics of Materials*, **58**, 1-11.

Pan, Y., Weng, G. J., Meguid, S. A., Bao, W. S., Zhu, Z. H., & Hamouda, A. M. (2011) Percolation threshold and electrical conductivity of a two-phase composite containing randomly oriented ellipsoidal inclusions. *Journal of Applied Physics*, **110**, 123715.

Pang, Y., Liu, J. X., Wang, Y. S., & Zhao, X. F. (2008). Propagation of Rayleigh-type surface waves in a transversely isotropic piezoelectric layer on a piezomagnetic half-space. *Journal of Applied Physics*, **103**, 074901.

Park, S., An, J., Piner, R. D., Jung, I., Yang, D., Velamakanni, A., Nguyen, S. T., & Ruoff, R. S., (2008). Aqueous suspension and characterization of chemically modified graphene sheets. *Chem. Mater.*, **20**, 6592-4.

Pike, G. E., & Seager, C. H. (1974). Percolation and conductivity: A computer study. *Phys. Rev. B*, **10**, 1421.

Psarras, G. C., (2006). Hopping conductivity in polymer matrix–metal particles composites. *Composites Part A*, **37**, 1545-1553.

Qiu, Y. P., & Weng, G. J. (1990). On the application of Mori–Tanaka's theory involving transversely isotropic spheroidal inclusions. *Int. J. Eng. Sci*., **28**, 1121–1137.

Qu, J. (1993a). Eshelby tensor for an elastic inclusion with slightly weakened interface. *J. Appl. Mech.*, **60**, 1048–1050.

Qu, J. (1993b). The effect of slightly weakened interfaces on the overall elastic properties of composite materials. *Mech. Mater.*, **14**, 269–281.

Ramanathan, T., Abdala, A. A., Stankovich, S., Dikin, D. A., & Herrera-Alonso, M. (2008). Functionalized graphene sheets for polymer nanocomposites. *Nature Nanotechnology*, **3**, 327-331.

Safdari, M., & Al-Haik, MS. (2012). Electrical conductivity of synergistically hybridized nanocomposites based on graphite nanoplatelets and carbon nanotubes. *Nanotechnology*, **23**, 405202.

Sarvestani, A. S., Shodja, H. M., & Delfani, M. R. (2008). Determination of the scattered fields of an SH-wave by an eccentric coating-fiber ensemble using DEIM. *Int. J. Eng. Sci.,* **46**, 1136–1146.

Sato, H., & Shindo, Y. (2001). Multiple scattering of a plane elastic waves in fiber-reinforced composite with graded interfacial layers. *Int. J. Solids Struct.,* **38**, 2549–2571.

Scarpa, F., Adhikari, S., Gil, A. J., & Remillat, C. (2010). The bending of single layer graphene sheets: the lattice versus continuum approach. *Nanotechnology*, **21**, 125702.

Seidel, G. D., & Puydupin-Jamin, A. S., (2011). Analysis of clustering, interphase region, and orientation effects on the electrical conductivity of carbon nanotube–polymer nanocomposites via computational micromechancis, *Mech. Mater.*, **43**, 755-774.

Selsil, O., Movchan, A. B., & Halvorsen, S. A. (2001). On oscillation of inhomogeneous fibers with imperfect interface. *Q. J. Mech. Appl. Math.,* **54**, 431–448.

Shang, J., Zhang, Y., Yu, L., Shen, B., Lv, F., & Chu, P. K. (2012). Fabrication and dielectric properties of oriented polyvinylidene fluoride nanocomposites incorporated with graphene nanosheets. *Materials Chemistry and Physics*, **134**, 867-874.

Shindo, Y., & Niwa, N. (1996). Scattering of anti-plane shear waves in a fiberreinforced composite medium with interfacial layers. *Acta Mech.*, **117**, 181–190.

Shindo, Y., Niwa, N., & Togawa, R. (1997). Multiple scattering of anti-plane shear waves on fiber reinforced composite medium with interfacial layer. *Int. J. Solids Struct.*, **35**, 733–745.

Shodja, H. M., & Delfani, M. R. (2009). 3D elastodynamic fields of nonuniformly coated obstacles: notion of eigenstress and eigenbodyforce fields. *Mech. Mater.*, **41**, 989–999.

Shodja, H. M., & Roumi, F. (2005). Overall behavior of composites with periodic multiinhomogeneities. *Mech. Mater.*, **37**, 346–53.

Shodja, H.M., Jarfi, H., & Rashidinejad, E. (2014). The electro-elastic scattered fields of an SH-wave by an eccentric two-phase circular piezoelectric sensor in an unbounded piezoelectric medium. *Mechanics of Materials*, **75**, 1-12.

Singh, A. P., Mishra, M., Chandra, A., & Dhawan, S. K. (2011). Graphene oxide/ferrofluid/cement composites for electromagnetic interference shielding application. *Nanotechnology*, **22**(46), 465701.

Soh, A. K., & Liu, J. X. (2006). Interfacial shear horizontal waves in a piezoelectric-pieozmagnetic bi-material. *Philosophical Magazine Letters*, **86**, 31–35.

Spaldin, N. A., & Fiebig, M. (2005). The renaissance of magnetoelectric multiferroics. *Science*, **309**, 391–392.

Srinivas, S., Li, J. Y., Zhou, Y. C., & Soh, A. K. (2006). The effective magnetoelectroelastic moduli of matrix-based multiferroic composites. *J. Appl. Phys.*, **99**, 043905.

Stanier, D. C., Patil, A. J., Sriwong, C., Rahatekar, S. S., & Ciambella, J., (2014). The reinforcement effect of exfoliated graphene oxide nanoplatelets on the mechanical and

viscoelastic properties of natural rubber. *Composites Science and Technology*, **95**, 59–66.

Stankovich, S., Dikin, D. A., Dommett, G. H. B., Kohlhaas, K. M., Zimney, E. J., Stach, E. A., Piner, R. D., Nguyen, S. T., & Ruoff, R. S. (2006). Graphene composite materials. *Nature*, **442**, 282-286.

Sun, W. H., Ju, G. L., Pan, J. W., & Li, Y. D. (2011). Effects of the imperfect interface and piezoelectric/piezomagnetic stiffening on the SH wave in a multiferroic composite. *Ultrasonics*, **51**, 831–838.

Tang, L. C., Wang, X., Gong, L. X., Peng, K., Zhao, L., Chen, Q., Wu, L. B., Jiang, J. X., & Lai, G. Q. (2014). Creep and recovery of polystyrene composites filled with graphene additives. *Composites Science and Technology*, **91**, 63–70.

Tong, Z. H., Lo, S. H., Jiang, C. P., & Cheung, Y. K. (2008). An exact solution for the three-phase thermo-electro-magneto-elastic cylinder model and its application to piezoelectric-magnetic fiber composites. *Int. J. Solids Struct.*, **45**, 5205–5219.

Van Suchtelen, J. (1972). Product properties: a new application of composite materials. *Philips Res. Rep.*, **27**, 28–37.

Varrla, E., Venkataraman, S., & Sundara, R. (2011). Functionalized Graphene-PVDF Foam Composites for EMI Shielding. *Macromol. Mater. Eng.*, **10**, 296-894.

Walpole, L. J. (1969). On the overall elastic moduli of composite materials. *J. Mech. Phys. Solids*, **17**, 235–251.

Walpole, L. J. (1981). Elastic behavior of composite materials: theoretical foundations. *Adv. Appl. Mech.*, **21**, 169–242.

Wan, Y. J., Gong, L. X., Tang, L. C., Wu, L. B., & Jiang, J. X. (2014). Mechanical properties of epoxy composites filled with silane-functionalized graphene oxide. *Composites Part A*, **64**, 79-89.

Wang, B. L., Mai, Y. W., & Niraula, O. P. (2007). A horizontal shear surface wave in magnetoelectroelastic materials. *Philosophical Magazine Letters*, **87**, 53–58.

Wang, D., Zhang, X., Zha, J. W., Zhao, J., Dang, Z. M., & Hu, G. H. (2013). Dielectric properties of reduced graphene oxide/polypropylene composites with ultralow percolation threshold. *Polymer*, **54**, 1916-1922.

Wang, X., & Pan, E. (2007). Magnetoelectric effects in multiferroic fibrous composite with imperfect interface. *Phys. Rev. B*, **76**, 214107.

Wang, X., Gong, L. X., Tang, L. C., Peng, K., Pei, Y. B., Zhao, L., Wu, L. B., & Jiang, J. X. (2015*a*). Temperature dependence of creep and recovery behaviors of polymer composites filled with chemically reduced graphene oxide. *Composites: Part A*, **69**, 288-298.

Wang, Y., Cheng, Y., Chen, J., Wu, D., Qiu, Y., Yao, X., Zhou, Y., & Chen, C. (2015*b*). Percolation networks and transient rheology of polylactide composites containing graphite nanosheets with various thicknesses. *Polymer*, **67**, 216-226.

Wang, Y., Su, Y., Li, J. & Weng, G. J. (2015*c*). A theory of magnetoelectric coupling with interface effects and aspect-ratio dependence in piezoelectric-piezomagnetic composites. *Journal of Applied Physcis*, **117**, 164106.

Wang, Y., Weng, G. J., Meguid, S. A., & Hamouda, A. M. (2014). A continuum model with a percolation threshold and tunneling-assisted interfacial conductivity for carbon nanotube-based nanocomposites. *J. Appl. Phys*., **115**, 193706.

Weng, G. J. (1984). Some elastic properties of reinforced solids, with special reference to isotropic ones containing spherical inclusions. *Int. J. Eng. Sci.,* **22**, 845.

Weng, G. J. (1990). The theoretical connection between Mori-Tanaka's theory and the Hashin-Shtrikman-Walpole bounds. *Int. J. Eng. Sci.*, **28**, 1111.

Weng, G. J. (2010) A dynamical theory for the Mori-Tanaka and Ponte Castaneda-Willis estimates. *Mechanics of Materials*, **42**, 886-893.

Worsley, K. A., Ramesh, P., Mandal, S. K., Niyogi, S., Itkis, M. E., & Haddon, R. C., (2007). Soluble graphene derived from graphite fluoride. *Chem. Phys. Lett.*, **445**, 51‑6.

Wu, Z. S., Zhou, G., Yin, L. C., Ren, W., Li, F., & Cheng, H. M. (2012). Graphene/metal oxide composite electrode materials for energy storage. *Nano Energy*, **1**, 107-131.

Yan, K. Y., Xue, Q. Z., Zheng, Q. B., & Hao, L. Z. (2007). The interface effect of the effective electrical conductivity of carbon nanotube composites. *Nanotechnology*, **18**, 255705.

Yan, P., Jiang, C. P., & Song, F. (2011). An eigenfunction expansion-variational method for the anti-plane electroelastic behavior of three-phase fiber composites. *Mech. Mater.*, **43**, 586–597.

Yan, P., Jiang, C. P., & Song, F. (2013). Unified series solution for the anti-plane effective magnetoelectroelastic moduli of three-phase fiber composites. *Int. J. Solids Struct.*, **50**, 176–185.

Yavari, F., Raeisi Fard, H., Pashayi, K., Rafiee, M. A., & Zamiri, A. (2011). Enhanced thermal conductivity in a nanostructured phase change composite due to low concentration graphene additives. *J. Phys. Chem. C*, **115**, 8753–8758.

Yousefi, N., Sun, X., Lin, X., Shen, X., Jia, J. J., Zhang, B., Tang, B. Z., Chan, M. S., & Kim, J. K. (2014). Highly aligned graphene/polymer nanocomposites with excellent dielectric properties for high-performance electromagnetic interference shielding. *Adv. Mater.*, **26**, 5480–5487.

Yuan, F. Y., Zhang, H. B., Li, X., Ma, H. L., Li, X. Z., & Yu, Z. Z. (2014). In situ chemical reduction and functionalization of graphene oxide for electrically conductive phenol formaldehyde composites. *Carbon*, **68**, 653-661.

Zandiatashbar, A., Picu, C. R., & Koratkar, N. (2012a). Control of epoxy creep using graphene. *Small* **8** (11), 1676–82.

Zandiatashbar, A. Picu, R. C., & Koratkar, N. (2012b). Mechanical Behavior of Epoxy-Graphene Platelets Nanocomposites. *Journal of Engineering Materials and Technology*, **134**, 031011-1.

Zhang, D., & Zhan, Z. (2016). Strengthening effect of graphene derivatives in copper matrix. *Composites Journal of Alloys and Compounds*, **654**, 226-233.

Zhang, H. B., Zheng, W. G., Yan, Q., Jiang, Z. G., & Yu, Z. Z. (2012). The effect of surface chemistry of graphene on rheological and electrical properties of polymethylmethacrylate composites. *Carbon*, **50**, 5117-5125.

Zhang, H. B., Zheng, W. G., Yan, Q., Yang, Y., Wang, J. W., Lu, Z. H., Ji, G. Y., & Yu, Z. Z. (2010). Electrically conductive polyethylene terephthalate/graphene nanocomposites prepared by melt compounding. *Polymer*, **51**, 1191-1196.

Zhang, K., Zhang, L. L., Zhao, X. S., & Wu, J. (2010). Graphene/polyaniline nanofiber composites as supercapacitor electrodes. *Chem. Mater.*, **22**, 1392-401.

Acknowledgment of Previous Publications

Hashemi, R. & Weng. G.J. (2016). A theoretical treatment of graphene nanocomposites with percolation threshold, tunneling-assisted conductivity and microcapacitor effect in AC and DC electrical settings, *Carbon*, **96**, 474-490.

Hashemi. R. (2016). Magneto-electro-elastic properties of multiferroic composites containing periodic distribution of general multi-coated inhomogeneities. *International Journal of Engineering Science*, **103**, 59-76.

Hashemi. R. (2016). On the overall viscoelastic behavior of graphene/polymer nanocomposites with imperfect interface. *International Journal of Engineering Science*, **105**, 38-55.

Hashemi. R. (2017). Scattering of shear waves by a two-phase multiferroic sensor embedded in a piezoelectric/piezomagnetic medium. *Smart Materials and Structures* (in press).